Multiple Echo, Caesar Cipher Acquisition and Model-Based Reconstruction (ME-CAMBREC): a Novel Accelerated T_2 Mapping Method

By

Christopher Lynn Lankford

Dissertation

Submitted to the Faculty of the

Graduate School of Vanderbilt University

in partial fulfillment of the requirements

for the degree of

DOCTOR OF PHILOSOPHY

in

Biomedical Engineering

December, 2016

Nashville, Tennessee

Approved:

Mark D. Does, Ph.D.

Bruce M. Damon, Ph.D.

Daniel F. Gochberg, Ph.D.

William A. Grissom, Ph.D.

E. Brian Welch, Ph.D.

To my wife, Mary

ACKNOWLEDGMENTS

I would like to acknowledge my primary funding source, NIH R01 EB001744. I would also like to thank my advisor and committee chair, Prof. Mark Does, whose vast knowledge and love of sharing it both seem bottomless. I thank my committee for helpful questions and direction, and my compatriots in the Does lab and VUIIS for countless educational discussions. Most importantly, I thank my wife Mary for her patience and support—I hope your time in professional school is as filled with helpful advice as my time in graduate school.

TABLE OF CONTENTS

Page

LIST OF TABLES

LIST OF FIGURES

LIST OF ABBREVIATIONS AND SYMBOLS

γ	Nuclear gyromagnetic ratio
ε	Root-mean-squared error
θ	Flip angle
λ	Regularization parameter in ME-CAMBREC
ω	Precession frequency
B_0	Static (main) magnetic field
B_1, B_1^+	Radiofrequency (transmit) magnetic field
C	Receive coil sensitivity coefficient
CC	"Caesar-cipher" phase encode ordering scheme
CPMG	Carr-Purcell-Meiboom-Gill (pulse sequence)
DESPOT1 (-2)	Driven equilibrium, single-pulse observation of T_1 (of T_2)
EP	"Echo prepared" pulse sequence scheme
EPG	Extended phase graph
ESP	Echo spacing duration
ETL	Echo train length
FID	Free induction decay
FSE	Fast spin-echo
GF	Echo generating function
H^+	Hydrogen nucleus; proton
$H(x,k)$	Hybrid-space images
$I(x,y)$	Fourier-reconstructed reference image in ME-CAMBREC
IEC	Indirect echo-compensated
k	Spatial frequency dimension in MRI
NMR	Nuclear magnetic resonance

M_0	Equilibrium magnetization
M_+	Excited magnetization
ME-CAMBREC	Multiple echo, Caesar-cipher acquisition and model-based reconstruction
MR	Magnetic resonance
MRI	Magnetic resonance imaging
MSE	Multiple spin-echo (pulse sequence)
MT	Magnetization transfer
N_{pe}	Matrix size in the phase encoding direction
N_Q	Number of acquired pseudoimages in ME-CAMBREC
N_T	Number of acquired echo trains in ME-CAMBREC
$Q(k)$	k-space pseudoimages in ME-CAMBREC
R	Acceleration (undersampling) factor
R_2	Spin-spin or transverse relaxation rate ($1/T_2$)
R_2^*	Rate of FID signal vanishing
RF	Radiofrequency
SAR	Specific absorption rate; energy deposition
SNR	Signal-to-noise ratio
T_1	Spin-lattice or longitudinal relaxation time
T_2	Spin-spin or transverse relaxation time
T_2^*	Time constant of FID signal vanishing
TE	Echo time
TR	Repetition time
VT	“Variable trajectory” phase encode ordering scheme

CHAPTER 1

INTRODUCTION

This dissertation presents a novel fast T_2 mapping method for magnetic resonance imaging (MRI) that is insensitive to transmit field errors and does not suffer from artifacts common to conventional fast spin-echo methods. Chapter 1 will introduce the concepts required to understand the motivation behind and techniques described here. The first section will cover the basics of rapid T_2 relaxometry, including its applications and challenges. Following this is a detailed technical introduction to the spin-echo and multiple spin-echo pulse sequences. The final section of this chapter will examine image reconstruction methods in MRI, from the classic Fourier model to so-called compressed sensing methods and beyond. By the end of this chapter, the reader should have an understanding of the need for accelerated T_2 mapping methods as well as a solid foundation in current fast and conventional T_2 mapping protocols.

The following chapter, *Fast T_2 Mapping with Multiple Echo, Caesar Cipher Acquisition and Model-Based Reconstruction (ME-CAMBREC),* introduces the novel method as published in *Magnetic Resonance in Medicine*. The reprinted article illustrates ME-CAMBREC in detail and demonstrates its capabilities through computational, doped water phantom, and human experiments. This chapter theoretically compares ME-CAMBREC to a steady-state method and empirically compares the method to conventional fast spin-echo protocols and parallel imaging.

Chapter 3, *Biasing Factors in ME-CAMBREC,* investigates more deeply the sources of error in ME-CAMBREC T_2 maps. In particular, it characterizes bias caused by three sources: i) over-regularization during reconstruction, ii) through-slice flip angle errors, and iii) multi-

compartmental relaxation. The results presented in the chapter more clearly inform users of ME-CAMBREC as to the method's limitations, and identify potential pitfalls in protocol design.

The fourth chapter, *T_2 Mapping with Fitted vs. Measured B_1^+: a Statistical Analysis*, attempts to determine whether the refocusing flip angle parameter in ME-CAMBREC should be independently measured and used as a constraint during reconstruction. It investigates this interesting tradeoff from a broader view of T_2 mapping, and provides a rule of thumb for the necessary B_1^+ accuracy, precision, and efficiency needed to improve a fitted T_2 map. Theoretical investigations of fully-sampled T_2 mapping protocols are presented alongside simulations validating the results in ME-CAMBREC.

After the Conclusion, in which the results of Chapters 2-4 are synthesized to form comments on whole-brain imaging with ME-CAMBREC, a number of Appendices are provided as additional references. These brief chapters derive certain probability equations used extensively in the dissertation and provide MATLAB (The MathWorks, Natick, MA) code for ME-CAMBREC reconstruction.

1.1: Rapid transverse relaxometry

The transverse relaxation time constant in MRI, T_2, has been shown to vary with tissue water compartmentalization (1–3). It is intuitive, then, that many disease states—particularly those in which local microstructure is somehow disrupted, such as multiple sclerosis (4,5) and certain myopathies (6–8)—present as hyperintense lesions to clinically standard T_2-weighted imaging protocols. For example, in the presence of edema or inflammation, pockets of freely-tumbling extraneous water form with higher T_2 (see Section 1.2.1) than the surrounding healthy tissue.

T_2-weighted MRI of the inflamed region would show contrast between healthy and inflamed tissue, with the inflammation appearing brighter on the resulting image.

The function mapping signal intensity to the exact value of T_2 is unknown and noninvertible for T_2-weighted images. Common forms of diagnostic imaging are therefore referred to as semiquantitative, in that they do not provide exact values of T_2 on a voxel-by-voxel basis. It is of interest in both the clinical and research settings to be able to generate T_2 maps: images which contain absolute values of the transverse relaxation time as a function of space. For reasons that will be examined throughout this chapter, conventional quantitative T_2 mapping methods require long scan times in order to achieve appropriate image resolution and volumetric coverage. This section will discuss methods used for generating T_2 maps in a fraction of a conventional scan's duration.

Multiple T_2-weighted images, typically with varying echo time (TE), must generally be acquired in order to generate a single T_2 map (9). In practice, these can either be acquired simultaneously using a multiple spin-echo (MSE) pulse sequence (10,11)—the challenges of which will be discussed in Section 1.2—or can be acquired one at a time, typically using fast spin-echo (FSE, also TSE, RARE) acceleration (12). Although the pulse sequence used for FSE is fundamentally identical to that used for MSE imaging, it utilizes a different k-space trajectory which results in a different scan time. Multiple spin-echo sequences acquire a number of images equal to the echo train length (ETL) in a number of excitations equal to the image matrix size in the phase encoding direction(s) (N_{pe}), but cannot acquire fewer images in order to reduce scan time. In contrast, sequences in FSE mode acquire one image in N_{pe}/ETL excitations, and can acquire more than one image in succession by extending scan time. Thus, FSE protocols will result in a shorter scan time than MSE sequences as long as fewer than ETL images are acquired. Both MSE

and FSE image series contain artifact compared to single spin-echo images (see Sections 1.2.4 and 1.3.1). While it is possible to acquire multiple images using a single spin-echo pulse sequence, this will require an increase in scan time by a factor of ETL compared to MSE methods, which is impractical *in vivo*.

Although the FSE and MSE imaging modes are incompatible, both paradigms can be combined with a wide variety of other acceleration schemes. Section 1.3 will cover undersampling schemes, such as parallel imaging (13–15), compressed sensing (16), and model-based reconstruction, all of which can be applied to either FSE or MSE. A separate acceleration technique, the acquisition of multiple k-space lines per spin echo in the same manner as echo planar imaging (17), is called gradient and spin echo (GRASE) imaging (18) and has been applied to transverse relaxometry (19–21). Although GRASE provides an opportunity to accelerate acquisition beyond the limits of FSE alone, it has been shown to reduce image signal-to-noise ratio (SNR) by a predictable amount due to the necessary increase in receiver bandwidth (19). Another applicable method, somewhat of a hybrid between undersampling and rapid acquisition methods, is the view-sharing family of techniques. One such method, k-space weighted image contrast (KWIC (22)), generates T_2 maps from a single FSE k-space data set in the same way as model-based reconstruction. Unlike model-based reconstruction methods, KWIC generates multiple T_2-weighted images as an intermediate step between image reconstruction and T_2 fitting.

Both MSE and FSE require a long repetition time (TR) in order to prevent T_1-mediated bias and mitigate energy deposition in irradiated tissue. A unique alternative to MSE/FSE-based T_2 mapping is the driven equilibrium, single-pulse observation of T_2 (DESPOT2) protocol (23,24). This variable flip-angle method utilizes steady state sequences with low flip angles and directly accounts for T_1, causing the protocol to favor short TRs and rapid scan times. However, despite

significant speed advantages and the generation of a simultaneous T_1 map, the complex behavior of short-TR, gradient-balanced pulse sequences has demanded a series of corrections and model extensions to account for, e.g., magnetic field inhomogeneities (25,26) and finite radiofrequency (RF) pulse effects (27). Ultimately, while DESPOT2 is certainly an attractive method, it is difficult to implement due to the swarm of articles incrementally updating the method.

A quantitative multi-parametric mapping protocol called magnetic resonance fingerprinting (MRF) has generated significant interest in the MRI community (28). This method utilizes large image sets acquired during signal transients to fit multiple parameters, including T_2. In order to rapidly derive information from such a large dataset, signal amplitudes are precomputed using, for example, the extended phase graph (EPG) algorithm (29); the MRF implementation of the EPG algorithm is distinct from that discussed in Section 1.2.5 due to pulse sequence differences, but the fundamental theory is similar. Due to the large number of images collected, the scan time for a Nyquist-sampled MRF acquisition ranges between 10 and 35 minutes for a single slice (29,30). Many acceleration techniques have been proposed to reduce this scan time, including compressed sensing (31) and simultaneous multi-slice imaging (32,33), and scan times shorter than a minute have been reported for these accelerated methods.

While it is somewhat outside the scope of this dissertation, it is important to note that transverse relaxometry is frequently employed in tissues that do not present a single T_2 decay time, such as myelinated nerve (2) and white matter (3,34). The multiexponential decay of signals from these tissues is taken to imply a physical separation of water compartments; in white matter, the short-lived signal compartment is associated with water trapped between layers of myelin (3). When fitting a single T_2 to signals from these tissues, the multiple signal components will present an apparent T_2 with less diagnostic specificity compared to the individual compartments' T_2 values

and respective signal fractions. Many tissues also partially consist of tightly bound macromolecular protons, which decay with such a short T_2 as to be invisible to conventional imaging. They will, however, still affect MR signals through the magnetization transfer (MT) pathway (35), which is discussed in more detail in Section 1.2.

1.2: Technical details of MSE and FSE sequences

Section 1.2 will describe the elements of the MSE/FSE pulse sequence with sufficient detail to appreciate the method family's challenges, hidden assumptions, and recent advancements. The pulse sequence considerations in the following sections are important both for understanding ME-CAMBREC and for identifying key and subtle limitations in the method, some of which are examined in Chapter 3: Biasing Factors in ME-CAMBREC.

1.2.1: First principles: what is T_2?

The nuclear magnetic resonance (NMR) and magnetic resonance imaging techniques measure variations in induced voltage across an inductor coupled to a sample located within an external magnetic field. Particles within the sample that contain both a magnetic moment and angular momentum (i.e., quantum spin) will, unless exactly aligned with the external field, precess around the external field according to the Bloch equation (36),

$$\frac{dM_x(t)}{dt} = \gamma\left[\mathbf{M}(t)\times\mathbf{B}(t)\right]_x - \frac{M_x(t)}{T_2}$$
$$\frac{dM_y(t)}{dt} = \gamma\left[\mathbf{M}(t)\times\mathbf{B}(t)\right]_y - \frac{M_y(t)}{T_2}$$
$$\frac{dM_z(t)}{dt} = \gamma\left[\mathbf{M}(t)\times\mathbf{B}(t)\right]_z - \frac{M_z(t)-M_0}{T_1}\ , \qquad [1.1]$$

where the spin magnetization $\mathbf{M} = \begin{bmatrix} M_x & M_y & M_z \end{bmatrix}^T$ is exposed to external magnetic field **B**, γ is the gyromagnetic ratio of the particle (commonly a lone proton, or hydrogen nucleus, H^+), M_0 is the magnetization at thermal equilibrium, and T_1 and T_2 are the spin-lattice and spin-spin relaxation times, respectively. The spin-lattice relaxation time, intuitively called the longitudinal relaxation time, represents the time required for the spin to return to thermal equilibrium—in other words, to align with **B**, which is generally along the *z*-axis. According to Bloembergen, Purcell, and Pound (BPP) theory (37), it is dominated by energy exchange and spatial tumbling at the Larmor precession frequency, ω:

$$\omega = \gamma B. \qquad [1.2]$$

Note that ω is defined as a left-handed—i.e., clockwise—frequency. In contrast to T_1, T_2 is often described as a transverse relaxation time, as it manifests in the plane perpendicular to **B**. It represents the time constant for the decay of NMR signal, as the measurable signal is proportional to the transverse magnetization. Spin-spin relaxation is dominated by low-frequency interactions between spins of different precession frequency, specifically at the spins' beat frequency, or precession frequency difference. Although quantum theory limits T_2 to twice T_1 ($2T_1 \geq T_2$) (38), BPP theory and practical observation dictate a stricter relationship, with $T_1 \geq T_2$.

At a given field strength, BPP theory suggests that increasing tumbling speed—in other words, increasing spin freedom within its microstructural compartment—leads to decreasing, then

increasing T_1 and a monotonically increasing T_2. This explains why proton NMR signals from macromolecules or mineral lattices, which have relatively low tumbling speeds, typically exhibit very short T_2, on the order of microseconds (1). In contrast, so-called free water protons exhibit a long T_2, on the order of milliseconds or, for the most unrestricted water pools, even seconds (39).

1.2.2: Spin-echo sequences and T_2-weighted images

The term spin-echo, or Hahn echo (40), refers to both a physical phenomenon and the pulse sequence utilized to generate a T_2-dependent signal at the echo time (TE). It contrasts with free induction decay (FID), as well as with more advanced echo types such as stimulated echoes which will be discussed in later sections. Figure 1.1 shows a schematic of the pulse sequence in its most fundamental form, and a detailed description of each element in the sequence follows.

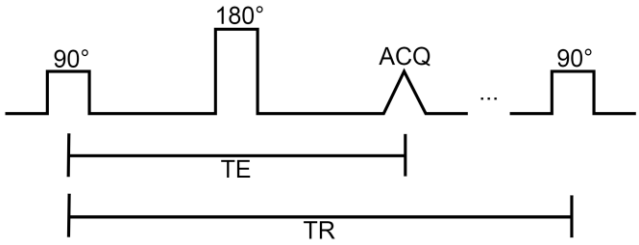

Figure 1.1: A schematic of the radiofrequency transmit/receive element for simple spin-echo sequences. Note that TE defines the echo time, which is equal to twice the duration between the excitation (here, 90°) and refocusing (here, 180°) pulses, and the repetition time TR defines the duration between each excitation pulse. Spoiler and crusher gradients, imaging gradients, pulse phases, and slice interleafs—all of which are important to common imaging variations of the spin-echo sequence—are not shown.

The sample is assumed to be in thermal equilibrium before the initial excitation at time $t = 0$. By applying a magnetic field perpendicular to the main field (B_0) and rotating it at a frequency matching the sample's Larmor frequency, spins in the sample can be nutated towards the transverse plane. This secondary field is called the radiofrequency (RF) or B_1 field, and the nutation effect of RF pulses is commonly described by a flip angle which is proportional to the integrated B_1 amplitude for an on-resonance pulse. The excited signal, which is proportional to the net transverse component of the magnetization M, is maximized when the excitation pulse flip angle is 90°. (It should be noted that for sequences in which TR is less than or on the order of T_1, this is not the case, as the longitudinal magnetization immediately before excitation is reduced to a steady-state value.)

After excitation, there is a delay period of time TE/2 during which subtle variations in precession frequency cause spins within the excited volume to dephase relative to each other. Net magnetization during this time rapidly decays according to a time constant T_2^*, and this period of signal evolution is called the FID. Each isochromat accrues a phase relative to the net magnetization of $\Delta\omega TE/2$ during this delay period. The refocusing pulse, which is described in more detail in the following section, would ideally then convert that phase to $-\Delta\omega TE/2$ for each isochromat in the volume. During the next TE/2 delay time, an additional $\Delta\omega TE/2$ is added to the spin phase after the refocusing pulse. At TE, the phase collapses to zero for all isochromats, and a signal echo is observed. The signal echo will be of a lower amplitude than the excited signal due to T_2 decay.

The distinction between T_2^* and T_2 is often a subtle one to students introduced to magnetic resonance for the first time. When considering relaxation rates, or $1/T_2$, one can consider a net rate

composed of reversible effects, such as time-invariant B_0 variations within the sample, and irreversible effects, such as spin diffusion:

$$R_2^* = R_2' + R_2$$
$$\frac{1}{T_2^*} = \frac{1}{T_2'} + \frac{1}{T_2}. \qquad [1.3]$$

Here the star notation denotes the total relaxation rate observed in the FID and the prime notation denotes a reversible component which can be unwound using a refocusing pulse. Note that T_2 is always longer than T_2^*, as the refocusing pulse enhances signal during the echo compared to an FID acquired at the same TE. As T_2^* is susceptible to variations in observation parameters such as magnetic field shim accuracy, it is less specific to tissue environment, and its absolute value is often of reduced diagnostic importance compared to T_2. (The relative nonspecificity of T_2^* values does not imply T_2^*-weighted imaging is not clinically relevant: dynamic imaging can be used to observe T_2^* *changes* in response to contrast agent injection (41) or external stimulus, as in blood oxygen level dependent (BOLD) functional MRI (42).)

Assuming arbitrary flip angles for the excitation (θ_1 along the *x*-axis) and refocusing (θ_2 along the *y*-axis) pulses and that each pulse is instantaneous, the transverse magnetization at TE can be shown to follow the isochromatic signal equation (43):

$$\begin{aligned} M_\perp(\Delta\omega, t = TE) = {} & iM_0 e^{-TE/T_2} \sin\theta_1 \cos^2\left(\theta_2/2\right) e^{-i\Delta\omega TE} \\ & + iM_0 e^{-TE/T_2} \sin\theta_1 \sin^2\left(\theta_2/2\right) \\ & - M_0 e^{-(TE/2)/T_2} \left(1 - \left(1 - \cos\theta_1\right) e^{-(TE/2)/T_1}\right) \sin\theta_2 e^{-i\Delta\omega TE/2}. \end{aligned} \qquad [1.4]$$

Here *i* is the imaginary unit aligned with the *y*-axis and $\Delta\omega$ is a precessing spin's deviation from the frequency of the rotating frame. The first term, which has dephased for a time TE, represents an FID from the excitation pulse. The last term—which has dephased for TE/2, is aligned with the

x-axis, and contains both T_2 and T_1 information—represents the FID from the refocusing pulse. The central term represents a true spin echo. When $\theta_1 = 90°$ and $\theta_2 = 180°$ as in Figure 1.1, the equation reduces to a familiar exponential decay,

$$\left|M_{\perp}\left(t=TE\right)\right| = M_0 e^{-TE/T_2}. \qquad [1.5]$$

The nonintuitive and admittedly intense trigonometry and T_1-T_2 cross-terms in Equation 1.4 represent the different coherence pathways a signal contains after a series of RF pulses. Each additional pulse grows the number of terms in the signal equation geometrically. This will be discussed further in Sections 1.2.4 and 1.2.5, which cover multiple spin echo pulse sequences and their numerical signal models.

Because imaging protocols demand a series of excitations in order to fully sample k-space, a long TR is often used in T_2-weighted spin-echo protocols in order to reduce the amount of T_1 information in the excited magnetization. If TR is chosen on the order of T_1, M_0 in Eq. [1.4] and [1.5] must be replaced by a reduced function of M_0, RF pulse timings and flip angles, and T_1. The corrected signal's sensitivity to T_1 monotonically decreases as TR grows larger, but this comes at a scan time cost.

1.2.3: The refocusing pulse

The previous section described a refocusing pulse as a transmitted radiofrequency signal which reverses the phase of affected spins, causing them to come into focus (i.e., form an echo) at time TE. The concept of coherence pathways was also introduced. The following section will expand on this foundation while investigating the practical limitations of refocusing pulses.

In practice, refocusing pulses never act as perfect 180° pulses. Although transmit field (B_1^+) variation and attenuation obviously contribute to erroneous flip angles, main field variation also contributes to transmit error—B_0 deviation leads to a spurious *z*-component of the effective magnetic field in the rotating frame, altering magnetization behavior during nutation. Furthermore, as slice selection in MRI is performed through the use of magnetic field gradients, amplitude modulated slice-selective refocusing pulses are inherently imperfect. Figure 1.2 shows an RF pulse with amplitude envelope shaped like the centermost five lobes of a sinc function. (In common parlance, this would be termed a soft or shaped pulse, or more specifically, a sinc pulse.) Although the pulse is certainly selective to a range of frequencies, its response in the lower panel does not have an ideal rectangular shape. Moreover, doubling the amplitude from a nominal 90° pulse to a nominal 180° pulse does not in any way provoke a doubled response. In fact, the pulse profile changes considerably, becoming sharper in the center and less uniform throughout.

A few techniques attempt to avoid the issues caused by selective refocusing pulses. One obvious workaround is to perform volumetric—i.e., 3D—imaging protocols. While this is advantageous from a noise variance perspective, it requires a significant increase in scan time, as a second phase encoded dimension is introduced. Another alternative is single-slice imaging, where slice-selective excitation is used in conjunction with nonselective refocusing. While this is SNR-inefficient compared to 3D and multi-slice protocols, it is a simplifying condition which is attractive in many cases. A slice-selective refocusing pulse with double or triple the excitation pulse's spatial width can also be employed as a compromise between single-slice and multi-slice acquisition schemes (44). This provides enhanced flip angle uniformity within the excited slice while still providing a response dropoff within the imaging volume. This particular solution to the

slice profile problem generally requires gaps between acquired slices, preventing volumetric coverage in a single scan.

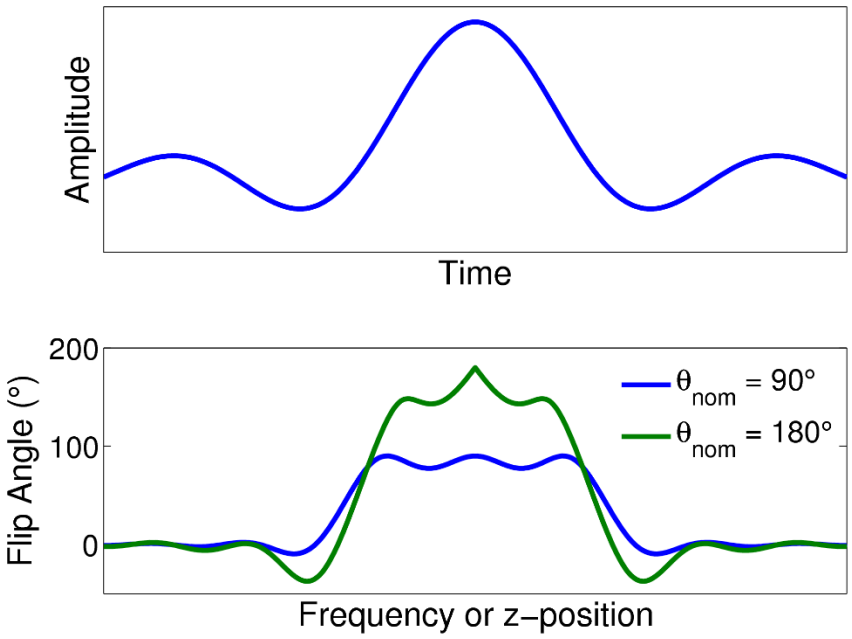

Figure 1.2: A sinc-shaped RF pulse and its flip angle profile for two nominal flip angles. Note that the flip angle profiles in the bottom panel have dramatically different characteristics both inside the selected slice and in the side lobes. The only difference between the two pulses which provided the profiles was a simple 2x amplitude scale factor.

Regardless of the extent of slice profile nonuniformity, a refocusing pulse with flip angle < 180° will generate signal in the same manner as an excitation pulse, which then decays as an FID signal according to T_2^*. This signal is generally minimized through the use of spoiler or crusher gradients (45). These gradient lobe pairs, which have the same polarity but flank the refocusing pulse on each side, dephase and rephase only the signal pathway which was in the transverse plane both before and after the refocusing pulse. Thus, signal excited by the refocusing pulse is only exposed to the latter gradient lobe, and is spoiled away due to excess dephasing. The case of multiple gradient-crushed refocusing pulses is more complicated, but briefly described as

part of a larger discussion on echo trains in Section 1.2.4. It is common to apply the crusher gradients in the slice-select direction; imaging voxels are largest in this direction, so spins dephase over a larger angle for a given gradient amplitude-time product.

Refocusing pulses are almost always assumed to be instantaneous. This assumption holds as long as the refocusing pulse duration (usually on the order of microseconds for hard pulses and milliseconds for shaped pulses) is much shorter than the T_2 of the sample. This criterion is paradoxically both true and false for many biological tissues. Tissues evaluated by conventional imaging methods have bulk T_2 values larger than a few milliseconds, or they would not be visible to those conventional methods. However, many of these MR-visible tissues are in constant exchange with MR-*in*visible protons, such as those associated with macromolecules (1,35). To these spins, refocusing pulse durations are decidedly not instantaneous, and more involved models are needed to study the spins' responses. Generally, integrated RF power (i.e., RF energy) predicts the response of very short-lived spins more closely than integrated RF amplitude (i.e., flip angle), and this response is a magnetization saturation, or monotonically decreasing **M**. The exchange of saturated ($\mathbf{M} \approx 0$) macromolecular protons with excited MR-visible protons causes a reduced effective signal in the excited pool; this is called magnetization transfer (35) contrast.

1.2.4: The echo train; or, why echo trains are not merely series of spin-echoes

Multiple spin echo pulse sequences generally use the Carr-Purcell-Meiboom-Gill (CPMG) framework (10,11). In this method, refocusing pulses are played out every time interval equal to TE, positioned equidistant to the surrounding echoes. Furthermore, the excitation pulse phase and

refocusing pulse phase are shifted 90° with respect to each other in order to ensure flip angle errors do not induce accumulating signal phase deviation (11).

The intuitive nature of CPMG sequences should not be mistaken as fundamental simplicity. A number of confounding factors affect acquired CPMG signals and provide implementation challenges. First and perhaps most significantly, the inclusion of at least three RF pulses in an echo train will generate stimulated or indirect echoes (46), which have been shown to bias fitted T_2 values (47–49). Stimulated echoes result from coherence pathways which involve the magnetization being first excited, then stored on the longitudinal axis by a second pulse, and finally returned to the transverse plane at half-amplitude by a third pulse. It is worth noting that conventional crusher gradients do not dephase stimulated echoes, as both a left- and right-crusher is experienced by the coherence pathway. Alternative crusher schemes exist which somewhat alleviate indirect echo contribution to CPMG signal (9), but an ideal gradient-crushed solution would require geometrically-increasing crusher amplitude, which is not practical due to gradient strength limitations. Furthermore, these methods are not compatible with optimized RF phase schemes such as the one presented by Meiboom & Gill (11). Signal models which include the effects of indirect echoes are described in detail in the following section. Although a somewhat subtler point, multiple spin echo pulse sequences generally have a smaller contribution of J-coupling to transverse relaxation due to their shorter echo spacing (50). This causes tissues with significant lipid fractions, such as adipose tissue, to appear bright on MSE images compared to single spin-echo images.

Multiple spin echo sequences are frequently limited by energy deposition, or specific absorption rate (SAR). It is intuitive that a series of large-amplitude refocusing pulses will deposit more heat in tissues than small-angle steady state or single spin-echo pulse sequences. Interleaved

multi-slice acquisitions are particularly egregious in this regard, as they transmit a number of 180° pulses equal to the echo train length (ETL) multiplied by the number of slice interleafs. This SAR limitation can reduce the scan time-efficiency of multi-slice MSE acquisitions compared to other protocols, and therefore extend scan times.

1.2.5: Modeling the multiple spin-echo signal

Conventional MSE sequences must contend with indirect echo signal contamination. Including the effects of indirect coherence pathways in signal calculations will, therefore, generate more robust estimates of T_2 when a series of images is fitted to the signal model. These effects can be calculated using straightforward Bloch equation simulation for each isochromat in a voxel (51,52), but this is extremely computationally expensive: full Bloch simulation demands numerically solving a series of simultaneous ordinary differential equations (Eq. [1.1]) for each isochromat and each refocusing pulse. Computationally tractable alternatives are therefore commonly employed. The two alternatives to Bloch simulation most critical to this dissertation are the extended phase graph (EPG (46,53)) and echo generating function (GF (54,55)) methods.

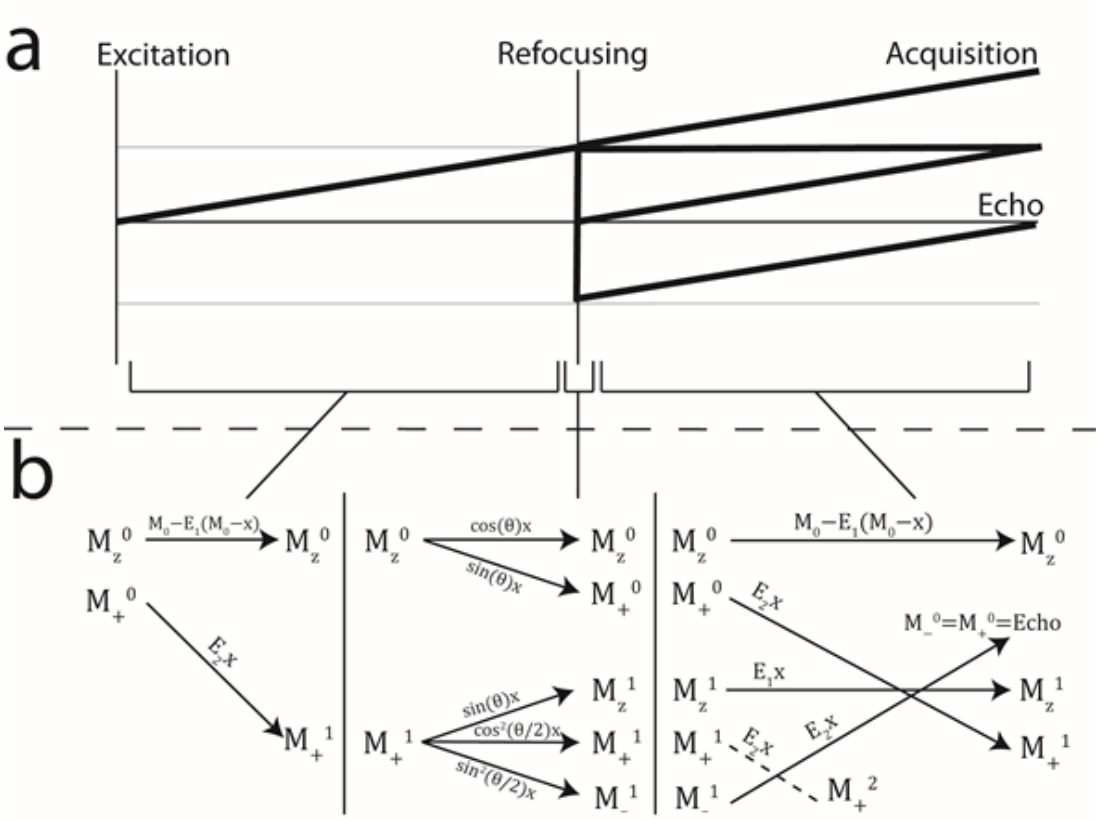

Figure 1.3: A schematic representation of the extended phase graph (EPG) model for one spin-echo. Interpulse periods are represented by signal decay according to T_1 and T_2 and +1 dephasing (upward diagonal lines in a, superscripts in b). Radiofrequency pulses perform trigonometric transforms on magnetization, mixing transverse and longitudinal coherences for each dephasing level. An echo is formed when spins in the M_{-}^{1} coherence channel rephase to the M^0 channel. Note that there is no consideration of an isochromat's specific precession frequency.

In brief, the EPG method treats each dephasing level, rather than each isochromat or each coherence pathway, as a separate entity, and assumes uniform phase throughout the acquisition. When slice-selective refocusing is used, the deviation in flip angle across the profile is occasionally corrected for by discretizing the profile and then summing across it (56–58). Figure 1.3 demonstrates the idea of tracing coherence pathways using trigonometric transforms, such as those apparent in Eq. [1.4]. The superscript of each magnetization describes the amount of dephasing that a pathway has experienced in units of the phase accrued during one interpulse period—i.e.,

one echo spacing. (It should not be surprising, then, that the EPG model requires uniform dephasing through each interpulse period. Fluid flow and modulated crusher gradients violate the assumptions of the model.) Magnetization in the M_+^0 coherence pathway represents a signal echo. Example curves generated by the EPG signal equation can be found in Figure 1.4.

The GF formulism is a noniterative signal calculation method, making it even more computationally efficient than the EPG model. However, in order to eliminate the need for recursive calculations, the model makes additional assumptions about the signal. Specifically, GF calculations treat measured echo amplitudes as the only nonzero coefficients in an infinite series; in other words, they assume that the echo train is sampled until the signal decays to zero. This will not generally be the case, particularly for tissues with very long T_2 such as CSF or for Rice-distributed magnitude signals, which decay towards the (nonzero) mean of a Rayleigh distribution. Taken together with the EPG and Bloch simulation methods, GF simulations represent another point on a spectrum of techniques with varying accuracy and computational speed.

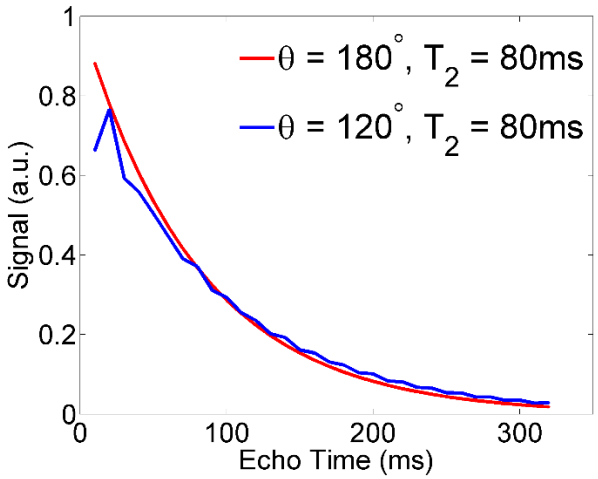

Figure 1.4: Sample curves generated by the EPG model. Stimulated echoes (blue curve) cause oscillations throughout the echo train which are particularly egregious at early TEs.

1.3: Image reconstruction

Image reconstruction in MRI typically involves the organization of data into a spatial frequency domain called k-space, which is then converted into a tomographic image through a Fourier transform. A brief derivation of this approach from first principles follows. Assumptions in the derivation—some of which are notably violated by conventional accelerated imaging techniques—are clearly stated.

1.3.1: Fourier reconstruction

The spatial frequency vector **k** is defined such that

$$\phi(\mathbf{r},t) = 2\pi\mathbf{k}(t)\cdot\mathbf{r}\,, \qquad [1.6]$$

where $\phi(\mathbf{r},t)$ is the gradient-induced phase of a spin at position **r** and time *t* in the rotating frame of reference. Expanding this into integral form using the definition of the (clockwise) Larmor frequency (Eq. [1.2]) provides

$$\phi(\mathbf{r},t) = 2\pi\mathbf{k}(t)\cdot\mathbf{r} = \int_0^t \gamma\mathbf{B}_g(\mathbf{r},\tau)\partial\tau\,, \qquad [1.7]$$

where $\mathbf{B}_g$ is the magnetic field in the *z* direction induced by magnetic field gradients. As these gradients are linear in space, the function $\mathbf{B}_g$ can be separated into the dot product of the gradient waveform **g** and the spin's position,

$$2\pi\mathbf{k}(t)\cdot\mathbf{r} = \gamma\int_0^t \mathbf{g}(\tau)\cdot\mathbf{r}\partial\tau\,, \qquad [1.8]$$

and if the spins are assumed stationary, **k** has the closed-form solution:

$$\mathbf{k}(t) = \frac{\gamma}{2\pi}\int_0^t \mathbf{g}(\tau)\partial\tau \,. \qquad [1.9]$$

It is possible to generate **k** values for every acquired sample during an imaging pulse sequence, and importantly, it is also possible to generate an arbitrary **k** through modulation of the gradient waveforms. This is, in the briefest sense, the objective of all MRI pulse sequences.

The receiver coil detects the integrated magnetization across its sensitive volume, *V*. If the detected signal at time *t* is *S* and the magnetization in the absence of imaging gradients is **M**, that signal will be described by

$$\begin{aligned} S(t) &= \int_V M_\perp(\mathbf{r},t)e^{-i\phi(\mathbf{r},t)}\partial\mathbf{r} \\ &= \int_V M_\perp(\mathbf{r},t)e^{-i2\pi\mathbf{k}(t)\cdot\mathbf{r}}\partial\mathbf{r} \,. \end{aligned} \qquad [1.10]$$

Equation [1.10] is a Fourier transform from **r**-space to **k**-space. Conventional image reconstruction algorithms utilize this relationship to generate images through the inverse Fourier transform by redefining *S* as a function of **k** and dropping the time dependence of **M**:

$$S(\mathbf{k}) = \int_V M_\perp(\mathbf{r})e^{-i2\pi\mathbf{k}\cdot\mathbf{r}}\partial\mathbf{r} \,. \qquad [1.11]$$

In practice, a series of **k** positions are sampled in rapid succession. These series can be rows oriented orthogonal to the **k**-space axes (Cartesian sampling), pass through the **k** origin (radial sampling), or take on more abstract shapes, such as spirals. These various techniques are dubbed readout patterns, or simply readouts.

Accelerated imaging methods such as fast spin-echo (12), echo planar imaging (17), and Look-Locker imaging (59) acquire multiple series of **k** positions—multiple readouts—per excitation in a temporal echo train. This reduces scan time by a factor equal to the number of readouts collected per excitation, but simultaneously violates the assumptions inherent to the Fourier reconstruction model in Eq. [1.11]. Point spread function-like blurring and the obscuration

of small image features (60) follow from the violated assumptions. Figure 1.5 demonstrates this phenomenon graphically.

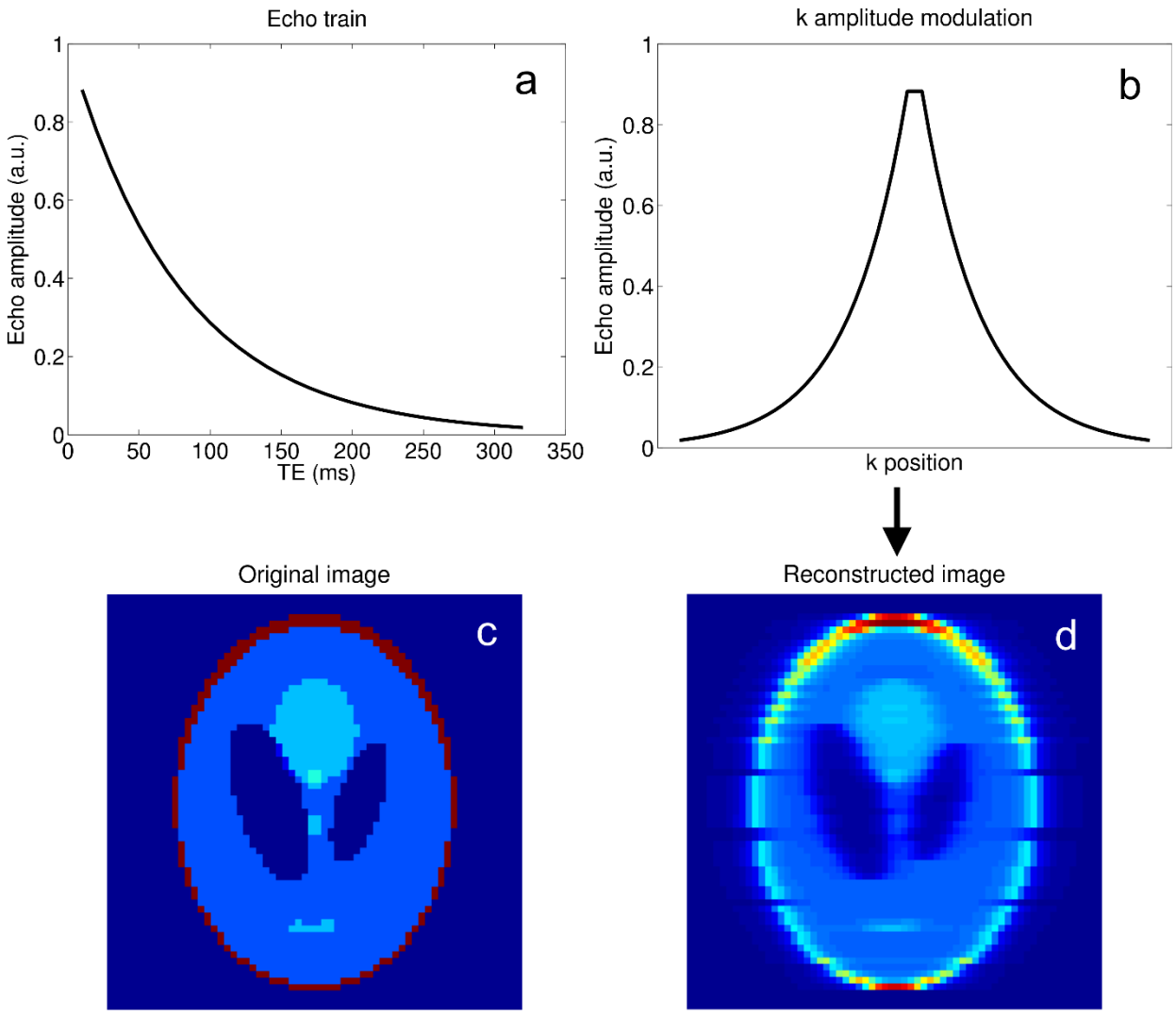

Figure 1.5: Artifact in FSE reconstruction. The original image (c) is acquired in a 32-echo train (a) in two acquisitions. This leads to amplitude modulation in k-space (b), which when reconstructed using the inverse Fourier transform, generates a blurred image with inaccurate signal values (d). In practice, acquiring an accurate image would take 32 times longer than acquiring the blurred image in panel (d).

The artifacts caused by Fourier reconstruction of rapidly-acquired data are a direct result of the assumption that all k-samples were collected at the same time after excitation (i.e., echo time). If instead of assuming **M** is time-invariant, we allow **M** to vary with time, a discretized version of Eq. [1.11] can be created as a more accurate MRI signal equation:

$$S_n = \sum_l M_\perp\left(\mathbf{r}_l, \mathrm{TE}_n\right) e^{-i2\pi \mathbf{k}_n \cdot \mathbf{r}_l} \qquad [1.12]$$

where n is the index of a sample gathered at time TE_n and k-position $\mathbf{k}_n$, and l is a spatial index. Unfortunately, this equation alone cannot be used for image reconstruction if accelerated acquisition techniques are employed; by the definition of an accelerated acquisition, there is insufficient data to fully characterize **M** at each echo time. Reconstruction approaches which solve the inverse problem of Eq. [1.12], or a variant thereof, are therefore said to reconstruct images or parameter maps from undersampled data.

1.3.2: Reconstructing undersampled images

In the previous sections, it was claimed that undersampling in MRI can be used to acquire images in a fraction of the time of conventional scans. However, solving the inverse problem of Eq. [1.12], or alternatively reconstructing images using the Fourier simplification (Eq. [1.11]) in conjunction with sub-Nyquist sampling, is a nontrivial challenge which demands further introduction before approaching the original work presented in Chapters 2-4. The following section will provide an overview of undersampled reconstruction techniques.

Perhaps the most straightforward family of undersampled imaging methods is partial-Fourier reconstruction (61–63). This methodology utilizes the conjugate symmetry of real signals' Fourier transforms in order to reduce the amount of data collected by up to one-half. In practice,

slightly more than half of k-space is sampled in order to correct for nonzero and nonuniform phase in image space. While this approach is straightforward, it provides a maximum acceleration factor less than 2 unless combined with other acceleration methods, such as in half-Fourier acquisition single-shot turbo spin-echo (HASTE (64)). This hybrid method combines the FSE readout with partial-Fourier reconstruction in order to acquire T_2 weighted images within a single excitation. Reconstructed images from HASTE are blurred, as all FSE images are, and are inaccurate in the presence of phase errors, similar to other partial-Fourier techniques.

The most widespread undersampled reconstruction technique is the family of methods referred to as parallel imaging; in particular, sensitivity encoding (SENSE (14)) and generalized autocalibrating partially parallel acquisitions (GRAPPA (15)). These methods utilize multiple receiver elements distributed in space. As each receiver element is sensitive to a distinct portion of the imaging volume, data collected by an ensemble of these elements are inherently spatially encoded. The synergistic information between receiver elements can be used to reconstruct images from samples of every second k-space line (acceleration factor R = 2), every third line (R = 3), etc. The acceleration factor can theoretically be as high as the number of receiver elements, but in practice, it is limited by overlap in the coil sensitivity profiles. Greater overlap reduces reconstruction quality and maximum practical acceleration factor, as the reconstruction problem becomes ill-posed. A related approach to parallel imaging is simultaneous multi-slice imaging (65), which uses the same principles to separate images acquired from multiple slices in the same readout. These images are acquired through pulse sequences that employ multiband RF pulses, and conventionally demand large peak RF power.

Another widely used, fast MRI technique that relies on undersampling is compressed sensing reconstruction (16). In compressed sensing applications, a regularization is used alongside the iterative image reconstruction least-squares problem,

$$I(\mathbf{r}) = \min_{M_\perp} \left[\sum_n \left(S_n - \sum_l M_\perp(\mathbf{r}_l) e^{-i2\pi \mathbf{k}_n \cdot \mathbf{r}_l} \right)^2 + \Psi\left(M_\perp(\mathbf{r}_l)\right) \right], \quad [1.13]$$

where Ψ is the regularization function. The colloquial definition of compressed sensing demands that Ψ be the L1-norm of a sparsifying transform, such as the gradient magnitude for many medical images, as this guarantees convexity of the cost function. Compressed sensing is an attractive technique due to its straightforward nature, but it cannot be directly applied to MR parameter mapping. The problem convexity granted through use of the L1-norm does not apply if $M_\perp$ is assumed to be a nonlinear function of MR parameters, and it is unknown how image bias induced by any given sparsifying regularization might propagate into parameter maps. Thus, generating parameter maps through iterative image reconstruction demands a subtly different brand of accelerated imaging protocol: the model-based reconstruction.

1.3.3: Model-based reconstruction

Model-based reconstruction techniques such as the one presented in this manuscript can be considered the quantitative-imaging counterpart to compressed sensing. The use of nonlinear reconstruction algorithms to directly fit MR parameters to k-space data dates to at least 1994, when Tong & Prato published an article in which T_1 was fitted to fast low-angle shot (FLASH) data acquired in less than 3 seconds (66). Although this method was complicated by issues arising from B_1^+ errors, it serves as an early example of model-based reconstruction, and similar T_1 mapping

methods utilizing radial Look-Locker acquisition schemes have been published in the past three years (67–69).

The current wave of model-based reconstruction methods interested in fitting T_2 began with a paper by Kai Tobias Block, Martin Uecker, and Jens Frahm in 2009 (70). Their work demonstrated that a radially-acquired FSE dataset could be used to directly generate a T_2 map in a fraction of the time it would take to acquire multiple fully-sampled T_2-weighted images. These authors have since published a plurality of the model-based reconstruction of T_2 literature. In 2011, Uecker and Frahm—this time with Tilman Sumpf—adapted the 2009 paper to a Cartesian readout (71). While this work was similar to ME-CAMBREC, it did not utilize an indirect echo-compensated signal model at the time. It was later adapted to include the echo generating function (GF) model in an article published in late 2014, making the updated method contemporary to ME-CAMBREC. A 2016 paper by Block and Noam Ben-Eliezer presented a comparable method utilizing Bloch simulation signal models and a radial readout (52).

Chuan Huang, Ali Bilgin, and Maria Altbach independently developed a similar protocol during this wave of literature. Their method was called the reconstruction of principal component coefficient maps (REPCOM) in a 2012 paper (72) and curve reconstruction via principal component analysis-based linearization with indirect echo compensation (CURLIE) in a follow-up article published in 2013 (57). These methods utilized an intermediate principal component space between k-space and the final T_2 map, while CURLIE employed the extended phase graph algorithm to correct for indirect echo pathways. Both methods required radial acquisition schemes.

More general reconstruction frameworks, typically presented without a specific signal model, have been proposed for accelerated MR parameter mapping (73–76). These frameworks often focus on particular sparsity transforms in the parametric (i.e., TE) dimension, and can be

considered to belong to both the compressed sensing and model-based reconstruction families of methods. While these techniques represent an intriguing approach to model-based reconstruction, they can be difficult to implement for any particular signal model due to their abstract presentation in literature. Furthermore, any complications that might arise from a specific implementation—for example, indirect echo-compensated T_2 mapping—appear to be left as exercises for the reader.

As of the acceptance of the manuscript reprinted in Chapter 2, there were no published model-based reconstruction methods which both i) corrected for stimulated and indirect echo pathways, in contrast to Block's 2009 paper, and ii) directly fit T_2 maps to k-space data, in contrast to the CURLIE method. Thus, the development of ME-CAMBREC using the extended phase graph algorithm represented a novel and important contribution to the contemporary literature. The simultaneous development of Sumpf's GF-based technique (55)—and subsequent inception of Ben-Eliezer's Bloch simulation-based method (52)—demonstrate that there is significant interest in accelerated T_2 mapping methods using model-based reconstruction. It is the purpose of this dissertation to demonstrate and thoroughly investigate the ME-CAMBREC method with the overarching goal of determining its challenges and advantages in the context of the cornucopia of accelerated imaging techniques.

CHAPTER 2

FAST T_2 MAPPING WITH MULTIPLE ECHO, CAESAR CIPHER ACQUISITION AND MODEL-BASED RECONSTRUCTION (ME-CAMBREC)

This chapter is adapted with permission from an article published in *Magnetic Resonance in Medicine* issue 73, March 2015, by Christopher L. Lankford, Richard D. Dortch, and Mark D. Does.

2.1: Introduction

The fast spin echo (FSE) pulse sequence is widely used in MRI due to its ability to quickly acquire high-resolution T_2 weighted images which are relatively insensitive to spatial magnetic field variations (12). However, when FSE is used for quantitative T_2 mapping, image artifacts caused by amplitude modulation in the phase-encoded direction of k-space, particularly in the presence of B_1 field variations, can induce significant errors in estimated relaxation time values. The sensitivity to B_1 field variation can be addressed through use of the extended phase graph (EPG) algorithm (46,53), and model-based reconstruction of parametric images such as T_2 maps from k-space data can inherently eliminate acceleration-induced artifacts in FSE images (57,70). This work integrates these ideas into a fast and B_1-insensitive method for T_2 and proton density mapping.

The EPG algorithm for calculating echo amplitudes (53) has received attention recently for its ability to compensate for indirect- or stimulated-echo pathways in multiple spin-echo

acquisitions, such as those used for FSE (77–79), T_2 mapping (56,80), or multi-exponential T_2 analysis (81,82). These coherence pathways occur as a result of refocusing flip angles that deviate from 180°, which may be by design (77–79) or due to in-plane field variations or slice profile effects. Prasloski et al. have also used the EPG algorithm for analysis of combined gradient and spin-echo imaging (20), which provided accelerated T_2 mapping at a predictable signal-to-noise ratio cost (19), but the EPG analysis remained decoupled from the reconstruction problem.

In most Fourier-reconstructed fast T_2 mapping methods, two general approaches are used to provide both acceleration and sensitivity to T_2. In the first, multiple acquisitions are made using a single (usually center-out) k-space trajectory prepared by a spin echo period to provide T_2 image contrast. In the second method, the k-space trajectory is altered (83) (or data is reordered, such as in view-shared protocols (22,84)) from one image to the next in order to weight the center of k-space differently without extending the echo train. Here the former is referred to as an echo-prepared (EP) acquisition and the latter as a variable trajectory (VT) acquisition. While EP techniques waste information before or after the echo trains, each VT image will have a unique set of artifacts which will compound when fitting T_2 maps. As both of these acquisition strategies are tailored to the requirements of Fourier-reconstructed images, a novel "Caesar cipher" acquisition strategy—named after the famed emperor's method of encoding text by wrapping the alphabet modulo its length—which is more suited to the proposed model-based reconstruction algorithm was developed. The proposed method is referred to as "Multiple Echo, Caesar cipher Acquisition and Model-Based REConstruction" (ME-CAMBREC).

2.2: Theory

ME-CAMBREC simultaneously fits three parameters on a voxelwise basis—the relaxation time constant T_2, refocusing pulse flip angle θ, and the complex transverse magnetization immediately after excitation, M_+. First, N_Q fast spin echo k-space pseudo images $Q_j(k_{ro}, k_{pe})$ (with unique effective echo time indexed by j, j = 1 to N_Q) are acquired in a number of echo trains, N_T, less than the number of phase-encoded lines in Q, depending on the desired acceleration factor. (Note than when $N_T = N_{pe}$, the number of points in the phase encoded direction, the acquisition requires the same scan time as a non-accelerated multiple spin-echo pulse sequence.) Since all points along the readout direction of a given line occur in the same echo and are therefore assumed to have the same T_2 weighting, Q can be Fourier transformed in one dimension to create hybrid-space images $H_j(x, k_{pe})$. The ensemble of points corresponding to a certain spatial position, x_0, in the read direction—i.e., all phase encoded points k_{pe} across all N_Q pseudo images for a given $x = x_0$—are collected in a vector $\mathbf{S}_{x0}$ (indexed by n) and paired with vectors $\mathbf{t}$ and $\mathbf{k}_{pe}$, the echo times and phase encode k-values at which $\mathbf{S}_{x0}$ were collected, respectively. Figure 2.1 demonstrates this data transformation in graphical form. Additionally, a reference image, I, is generated by inverse 2D Fourier transform of the Q_1 image, i.e. the k-space image with the shortest effective echo time, $I = F_{2D}^{-1}\{Q_1\} = F_{pe}^{-1}\{H_1\}$. This reference image is used in the model-based reconstruction as an initial guess, as part of a regularization penalty, and to threshold the parameter maps *a priori*. For each row of data (i.e., each value of x_0), voxels with magnitude < z % of the maximum of $|I(x_0, y)|$ are not fitted and constrained to zero.

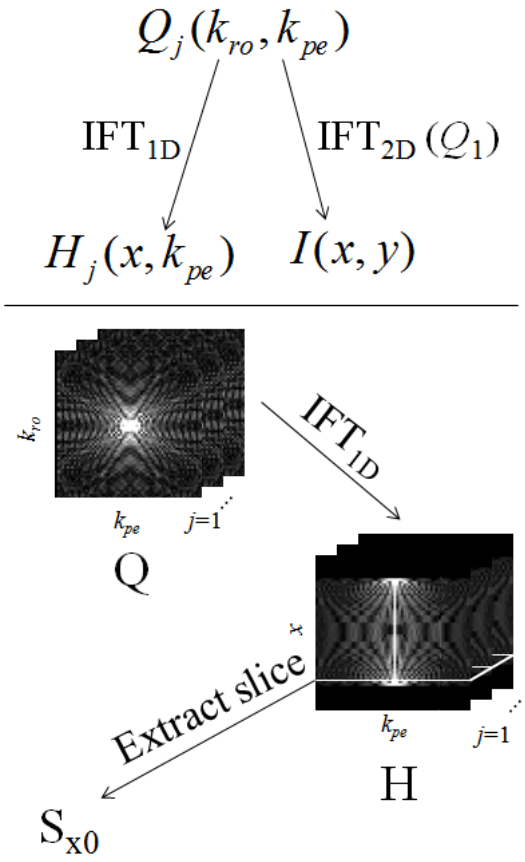

Figure 2.1: Data sorting and preparation. Fast spin echo k-space images *Q* are transformed into a hybrid space *H*, from which parameter map reconstruction occurs row-by-row. A reference image *I* is also generated through simple Fourier reconstruction of the earliest effective echo time data.

Once the vector $\mathbf{S_{x0}}$ has been constructed for a given image row, M_+, T_2, and θ are fitted simultaneously using the cost function

$$\varepsilon = \sum_{n=1}^{N_Q N_{pe}} \sum_{c=1}^{N_C} \left| \sum_{l=1}^{L} C_{c,l} M_{+,l} EPG\left(t_n, T_1 = 1\mathrm{s}, T_{2,l}, \theta_l\right) \exp\left(-\frac{i2\pi l k_{pe,n}}{L}\right) - S_{n,c} \right|^2 + \lambda \cdot p\left(M_+, I\right), \quad [2.1]$$

where $EPG(\cdot)$ represents the extended phase graph calculation, l is an index corresponding to y position (l = 1 to L), and p is the regularization function, defined below, which is weighted in the

cost by λ. The parameter $C_{c,l}$ is the complex coil sensitivity at position l of the c^{th} receive coil element of an N_C coil array.

The regularization is a fractional variation constraint designed to penalize added sharpness in the fitted M_+ over the reference image I:

$$p = \sum_l \left(\frac{\mathrm{Re}\left[M_{+,l+1} - M_{+,l} \right]}{\mathrm{Re}\left[M_{+,l+1} + M_{+,l} \right]} - \frac{\mathrm{Re}\left[I_{l+1} - I_l \right]}{\mathrm{Re}\left[I_{l+1} + I_l \right]} \right)^2 + \sum_m \left(\frac{\mathrm{Im}\left[M_{+,l+1} - M_{+,l} \right]}{\mathrm{Im}\left[M_{+,l+1} + M_{+,l} \right]} - \frac{\mathrm{Im}\left[I_{l+1} - I_l \right]}{\mathrm{Im}\left[I_{l+1} + I_l \right]} \right)^2 . \quad [2.2]$$

The spatial difference taken in the penalty function makes this regularization similar in spirit to total variation constraint, but with the following important distinctions: 1) the use of a blurred reference image, I, which will reduce the penalty burden in regions of genuine spatial variation of M_+, 2) the normalization by the sum of the values of M_+ or I, which is required due to the different scaling of the reference image caused by signal decay before the first echo, and 3) the usage of a 2-norm rather than a 1-norm, for ease of computation. The behavior of this regularization is intuitively straightforward. When the penalty weighting factor λ is close to zero, noise amplification from phase encoded lines acquired near the end of the echo train causes significant image degradation. As the weighting factor increases, the M_+ image becomes increasingly similar to a scaled version of I. The regularization used here is not intended to be optimal, but rather as an intuitive use of *a priori* knowledge regarding the M_+ map. Further study may find alternate regularization strategies that provide better performance, such as a sparsity constraint over some transform of the data.

Optimal tuning of λ is a nontrivial process. Here, a nonlinear L-curve (85) approach was used, where the optimal λ is selected as the point where a marginal increase in penalty weighting begins to induce a notable increase in solution residuals. Mathematically speaking, the value of λ

chosen is the value that maximizes the curvature, κ, of a log-residual vs. log-penalty graph parameterized by λ:

$$\kappa = \frac{\left(\frac{r}{\lambda p}\right)}{\left(1+\frac{r^2}{\lambda^2 p^2}\right)^{3/2}}\left(\frac{r}{\lambda^2\left(\nabla_\beta p^T H^{-1}\nabla_\beta p\right)}-\left(\frac{r}{\lambda p}+1\right)\right). \quad [2.3]$$

This equation was adapted from literature (86), correcting for typographical errors. Here r is the sum-squared residual term and p is the scalar penalty term from Eq. [2.1] and [2.2]. The gradient vector with respect to model parameters β is defined as $\nabla_\beta p$, and H is the Hessian (second derivative) matrix of the entire cost function. By plotting κ against λ, an optimal value for λ can be estimated; in the following, a single value of λ was selected for each image using a small sample of the image rows.

ME-CAMBREC also uses a novel acquisition scheme to further reduce noise amplification. Unlike Fourier reconstruction, which introduces artifacts related to the properties of a k-space amplitude modulation function, image noise in model-based reconstructions will be amplified at any spatial frequencies not sampled at early echo times. It is, therefore, disadvantageous to acquire the high spatial frequency lines of Cartesian k-space at the end of every echo train. Instead of using either the EP or VT methods to provide T_2 contrast, ME-CAMBREC provides T_2 contrast by sampling phase encoded lines in a Caesar cipher-like (CC) pattern. This trajectory can be considered an application of the rotated rapid acquisition relaxation enhanced methodology (87) to a center-out framework. In this acquisition strategy, the first echo train(s) acquire a center-out image (Q_1). The next pseudo images (Q_j, $j = 2, 3, \ldots$) are acquired by pushing the entire trajectory down the echo train and moving the last phase encode lines—those which would require the echo train to be extended if they were acquired in center-out order—to the beginning of the echo train.

For example, given the first trajectory k_{pe}=0,-1,1,-2,2 the second trajectory is k_{pe}=2,0,-1,1,-2, the third is k_{pe}=-2,2,0,-1,1, and so on, as shown in Figure 2.2. Acquiring fewer pseudo-images than the echo train length provides accelerated acquisition compared to conventional multiple spin echo imaging.

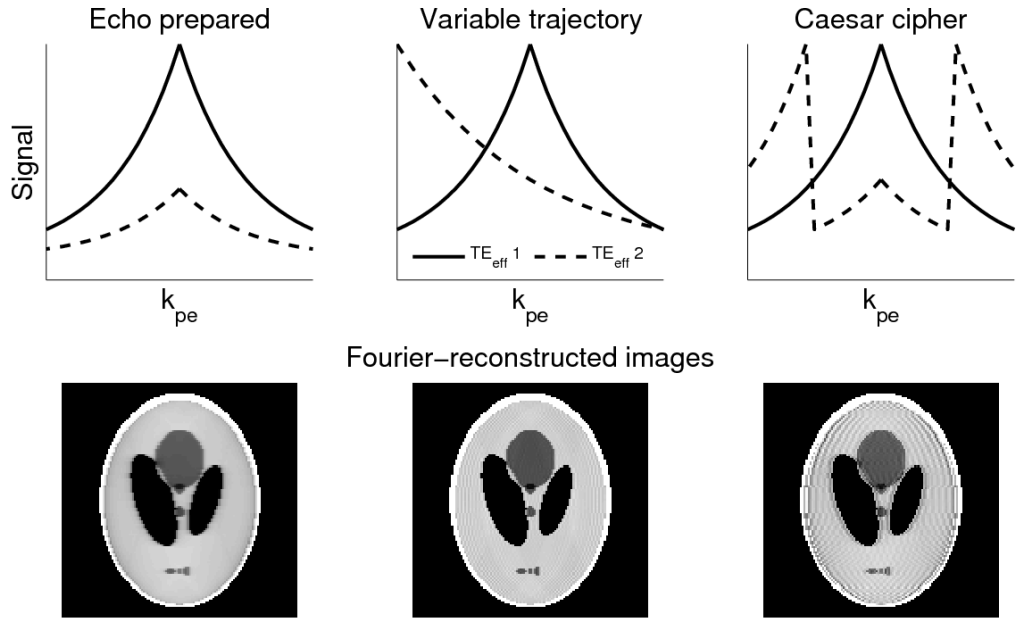

Figure 2.2: Artifact and k-space trajectory. The upper portion of the figure represents the acquired echo train from shot to shot as effective echo time increases; the solid line is a center-out acquisition common to most FSE schemes, while the dashed line demonstrates a later TE_{eff} using the given acquisition strategy. In the echo-prepared image, blurring (but not ghosting) is present. Both types of artifact exist in other sampling schemes, with the proposed Caesar cipher acquisition clearly being unsuited to Fourier-based reconstruction.

2.3: Methods

2.3.1: Computational experiments

The ME-CAMBREC method was compared to analysis of Fourier-reconstructed images using previously established trajectories, namely the EP and VT methods. The computational phantom used for each experiment was as follows. A 128 (N_{ro}) × 128 (N_{pe}) Shepp-Logan phantom with intensity values ranging from 0.8 to 1 was used as a proton density map; each compartment of that map had its own uniform T_2, ranging from 60-500 ms; a flip angle map varying smoothly across the image over 110-130° was used for all EPG-based analysis, and a similar map varying from 170-190° was used for exponential model fitting. A four-shot ($N_T = 4N_Q$) mock acquisition using each trajectory was performed with the following parameters: echo spacing (ESP) = 10 ms, echo train length (ETL) = 32 echoes, effective echo time (TE_{eff}) = 10, 90, 170, 240 ms for CC and EP, TE_{eff} = 10, 40, 90, 160 ms for VT. (The VT acquisition scheme used lower effective echo times because it is not suited to acquiring the $k_{pe} = 0$ line after the halfway point of the echo train; doing so would require an outside-in type trajectory.) Since $N_T = 4N_Q = 16 = N_{pe}/8$, the acceleration rate, R, for all mock acquisitions was equal to 8. Noise was added to the data at a magnitude image signal to noise ratio (SNR) of 15 for the median intensity voxels of the Shepp-Logan phantom, which represents about the lowest SNR permissible for quantitative imaging. The ME-CAMBREC reconstructions were regularized using optimal weighting levels (see the Fitting Algorithm section). The resultant parameter maps were compared to the actual underlying parameters as were reconstructed maps using data with median SNR = 30, 60, and 120. Additionally, parameter maps from Fourier-reconstructed voxel-wise fitting to the extended phase graph and exponential models

were created for comparison using both EP and VT trajectories. Error metrics were calculated root-mean-square (RMS) errors relative to known values, reflecting parameter estimate variance more than bias error at low SNR and the opposite at high SNR.

In order to compare the proposed method to a more disparate fast T_2 mapping protocol, DESPOT2 (23), the Cramer-Rao lower bound of the variance of T_2 was calculated for both ME-CAMBREC and a sample implementation of DESPOT2 (88) using the same Shepp-Logan phantom. The mean coefficient of variation of T_2 estimates (defined as the Cramer-Rao bound divided by the true value) across an image row was calculated. Additionally, since each method will have unique noise characteristics and scan times, these were accommodated in an overall calculation of SNR efficiency (i.e., T_2 SNR per unit root scan time). The DESPOT2 acquisitions simulated the following parameters: spoiled gradient-recalled echo: TR = 11.7 ms, flip angles = 4° and 15°, receiver bandwidth = 15.6 kHz; steady-state free precession: TR = 3.7 ms, flip angles = 15° and 55°, receiver bandwidth = 62.5 kHz. Both methods assumed a 256 × 256 in-plane matrix, with DESPOT2 acquiring 128 points in the third dimension and ME-CAMBREC acquiring this many 2D slices. Scan parameters for ME-CAMBREC were adapted from the human imaging protocol (see Human Experiments), with the receiver bandwidth adjusted to 36.6 kHz to acquire the new matrix size in the same echo spacing. Simplifying assumptions for DESPOT2 included instantaneous approach to steady state, no compressed sensing/partial Fourier acceleration, and *a priori* knowledge of confounding factors such as off-resonance/flip angle maps which are often measured in practice.

2.3.2: Phantom experiments

An eight-tube phantom containing copper sulfate and manganese chloride solutions (T_2 range: approximately 15ms-150ms) was imaged on a 4.7 T/31 cm Agilent/Varian (Santa Clara, CA) DirectDrive MRI system equipped with a single element volume coil (N_C = 1, Eq 2.1) using CC, EP, and VT k-space sampling methods. A multiple spin echo pulse sequence with constant gradient dephasing in every inter-echo period was used with the following parameters: matrix size = 64 (N_{ro}) × 64 (N_{pe}), ETL = 16 echoes; TE_{eff} = 5, 25, 45, and 60 ms for CC and EP and 5, 15, 25, and 30 ms for VT; refocusing flip angle = 120°; N_Q = 4; N_T = 16; ESP/TR = 5/2500 ms; slice thickness = 2 mm; refocusing pulse width = 5 mm. It should be noted that this wide refocusing pulse width would require a 1.5 mm gap between slices if the acquisition were performed in multi-slice mode, although only one slice was acquired here. These data were subjected to ME-CAMBREC (CC) and Fourier-reconstructed EPG analysis (EP, VT). The T_2 maps resulting from these protocols were compared to EPG analysis of a fully-sampled multiple spin-echo dataset acquired using the same scan parameters and double the echo train length. The errors were calculated as relative errors of the mean of each sample tube, reflecting systematic bias and artifact more than noise characteristics.

2.3.3: Human experiments

The brain of a healthy volunteer was imaged on a 3.0-T Philips (Best, NL) Achieva MRI system using an 8-element head coil (N_C = 8, Eq 2.1) and a multiple spin-echo pulse sequence with uniform echo spacing and constant gradient dephasing in every inter-echo period. The following

sequence parameters were used: ETL = 32, ESP/TR = 10/2500 ms, slice thickness = 5 mm (excitation)/15 mm (refocusing), in-plane resolution = 2×2 mm^2, number of averaged acquisitions = 1, SENSE acceleration factor = 1, and image matrix = 105 (N_{ro}) × 105 (N_{pe}). This resulted in a scan time of 4m 23s. (The slice gap required if a user wished to perform this scan in multi-slice mode would be 5 mm.) Coil sensitivity maps (C_c in Eq 2.1) were estimated from the first echo image using a cubic polynomial basis. Two fully sampled multi-echo image sets were acquired, one using refocusing pulse flip angles prescribed at 120° and the other at 180°, in order to compare EPG methods to exponential decay fitting. These data were sub-sampled into datasets emulating CC, EP, and VT acquisition schemes, each with $N_Q = 4$, $N_T = 16$ ($\approx N_{pe}/6.6$) and ETL = 26 (to roughly match the matrix size of 105). The CC ordered sub-sample used TE_{eff} = 10, 80, 150, and 210 ms; for VT, TE_{eff} = 10, 40, 60, and 110 ms; for EP, TE_{eff} = 10, 20, 30, and 50. The EP TE_{eff}s were low in order to prevent extending the echo train and substantially changing the total scan time between protocols. These sub-sampled data represented an $R = 6.6$ acceleration compared with the fully sampled data. These data were analyzed in a similar manner to the phantom studies, specifically focusing on a heterogeneous rectangular region of interest (ROI) containing both white matter and deep gray matter, but excluding cerebrospinal fluid due to its long T_2. For all accelerated methods, error was defined as the difference between estimated T_2 values and those estimated from fully sampled data. Error metrics were tabulated as RMS errors over a heterogeneous region, reflecting both noise and artifact. For comparison, previously published (21) T_2 values of the dominant signal component of various brain regions have also been presented.

ME-CAMBREC was also compared to the sensitivity encoding (SENSE) method of parallel imaging acceleration (14). The same coil sensitivity maps were used for ME-CAMBREC

and SENSE. ME-CAMBREC was performed using fully-sampled data reduced by a factor R ≈ 2 (N_Q = 13, N_T = 52 ≈ N_{pe}/2). The ME-CAMBREC T_2 map was compared to one resulting from voxelwise EPG fitting of 32 SENSE-reconstructed images with acceleration factor R = 2. In turn, ME-CAMBREC was performed on a data subset which was both undersampled in k-space (R = 2, i.e. all odd k_{pe} lines were excluded) and undersampled in the echo dimension (N_Q = 13, N_T = 26) for a total acceleration factor of roughly R = 4. This "sub-Nyquist" ME-CAMBREC reconstruction was compared to purely accelerating in the k-spatial dimension (SENSE, R = 4) and purely accelerating in the echo dimension with $R \approx 4$ (ME-CAMBREC, N_Q = 7, N_T = 28 ≈ N_{pe}/4).

2.3.4: Fitting Algorithm

For fitted voxels, initial guesses for M_+ (real and imaginary values) were taken from the image I, T_2 was initialized to a linearized least-square estimate for all points in **S** where k_{pe} = 0, and θ was initialized to the prescribed value. For all cases, T_1 was constrained to 1s, and the intensity threshold, z, was set to 5 %.

An iterative nonlinear least-squares solver (*lsqnonlin* in MATLAB (The MathWorks, Natick, MA)) was used to minimize the cost function. In order to accelerate the computation of each iteration, the gradient of the cost-function with respect to model parameters was calculated using a direct analytical formulation of the penalty gradient and a computational shortcut for the gradient of the sum squared residual:

$$\frac{\partial c}{\partial \beta} = 2\,\mathrm{Re}\left[\sum_n \frac{\partial M_{+,a} EPG\left(t_n, T_1 = 1\mathrm{s}, T_{2,a}, \theta_a\right)}{\partial \beta} \exp\left(-\frac{2\pi i a k_{\mathrm{pe},n}}{L}\right) r_n^*\right] + \lambda \frac{\partial p}{\partial \beta}, \qquad [2.4]$$

where r_n^* is the complex conjugate of the residual at index n, and β represents any of the fitted parameters. This shortcut is enabled through the knowledge that each reconstruction parameter β only appears in the equations of a single spatial point a. An extension of this equation into a second differential order can be used to expedite calculation of the cost function's Hessian matrix as well, for use in determining the optimal regularization level. The entire algorithm allows for fitting one image row in 15-30 seconds on standard personal computer hardware, but this should not be considered an optimized reconstruction time.

2.4: Results

2.4.1: Computational experiments

Table 2.1 summarizes the root-mean-squared error (ε_{rms}) of all three reconstructed parameter maps from simulated data, excluding cerebrospinal fluid-like regions with very long T_2 (500ms) which would otherwise dominate error calculations. The errors presented were for data with median SNR = 60. Propagation of error laws dictate that parameter estimate variance should decrease at least linearly with the standard deviation of the image noise, but Figure 2.3 shows a diminishing return in total RMS error due to inherent bias in the estimators. Model-based reconstruction of CC k-space encoded data (i.e., ME-CAMBREC) performed well relative to Fourier-reconstructed protocols. Perhaps unsurprisingly, the simple echo-prepared, exponential fit FSE protocol demonstrated high sensitivity to T_2 and the lowest error when near-perfect refocusing was simulated.

Table 2.1: RMS error of reconstruction in a computational phantom. Results from the computational study utilizing four FSE images (at SNR = 60) for each method. The labels, such as Fourier-EPG + EP, denote the method of reconstruction (Fourier transform or model-based fitting), the decay model used in the fit (EPG or exponential, EXP), and the k-space view ordering (CC, EP, or VT). ME-CAMBREC provided lower RMS errors in T_2 estimates than any other method except echo prepared FSE fit to an exponential decay curve.

Recon. + Acq.	$\varepsilon_{rms,\ M+}$ (a.u.)	$\varepsilon_{rms,\ T2}$ (ms)	$\varepsilon_{rms,\ \theta}$ (°)
Model-Based + CC (ME-CAMBREC)	0.21	8.3	22.0
Fourier-EPG + EP	0.15	15.7	21.7
Fourier-EPG + VT	0.16	14.0	17.4
Fourier-EXP + EP	0.05	7.6	-
Fourier-EXP + VT	0.05	10.8	-

ME-CAMBREC was discovered to have an SNR efficiency (i.e., T_2 SNR per unit root scan time) 2.4 times higher than that of a previously published four-angle implementation of DESPOT2. This was primarily due to the sensitivity of multiple spin-echo sequences compared to steady-state sequences.

2.4.2: Phantom experiments

Figure 2.4 shows T_2 maps (top) and relative errors (bottom) from the phantom experiments for different acquisition and analysis protocols. ME-CAMBREC performed well across the range of T_2s, with relative errors of less than 5%. Although any EPG analysis of the $CuSO_4$ solutions (T_1

$\approx T_2$) in the presence of imperfect refocusing will result in a small bias in the T_2 estimates(56), Figure 2.4 shows that the unknown T_1 does not result in additional error or artifact in ME-CAMBREC maps. As was the case in the computational study, accelerated Fourier-reconstructed EPG analysis performed poorly for certain T_2s, especially short ones such as those of tubes 4 and 7. T_2 was underestimated by both Fourier FSE methods, in some cases by more than 30%. Severe artifact was also present in both Fourier-based T_2 maps.

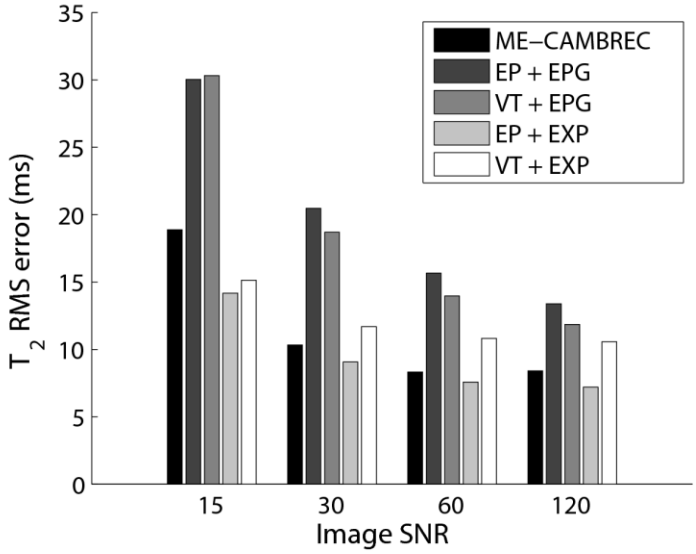

Figure 2.3: RMS Errors in estimated T_2 vs SNR for various FSE methods. Legend keys refer to the acquisition trajectory (EP or VT) and the fitting model (EPG or exponential, EXP). EXP fits were applied to data refocused using 170-190° pulses; all others were applied to 110-130° refocused data. As SNR increases, ME-CAMBREC and other accelerated protocols approach a lower error limit due to estimate bias. In practice, ME-CAMBREC demonstrates better T_2 accuracy than most Fourier-reconstructed methods at both high and low SNR.

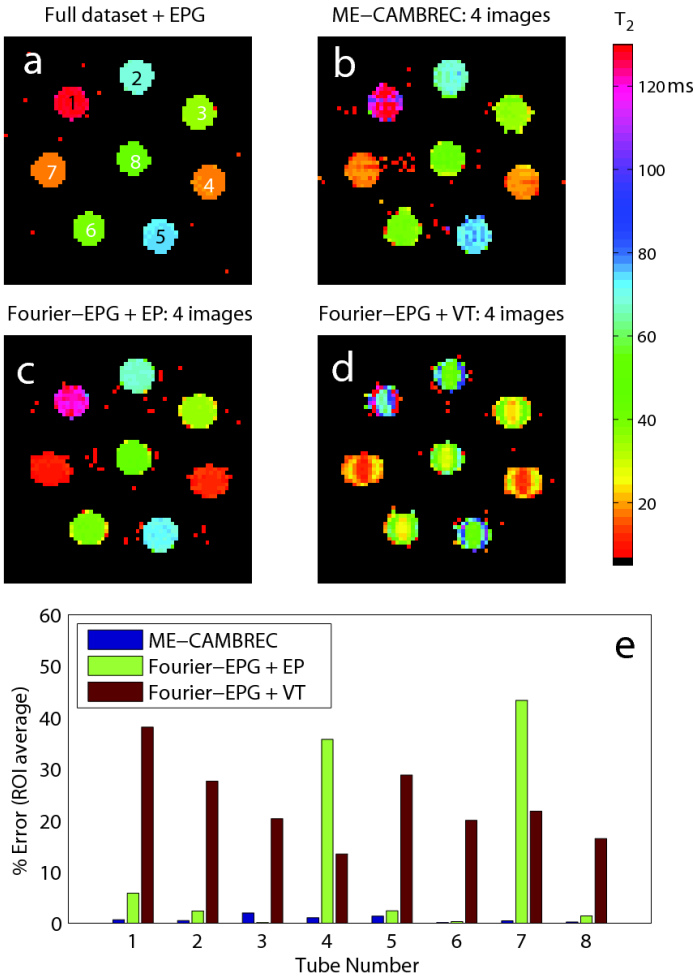

Figure 2.4: Reconstructed T_2 maps in a physical phantom. In short T_2 regions such as tubes 4 and 7, Fourier-based fast T_2 mapping methods either underestimate (c) or overestimate (d) high spatial frequency signal, resulting in blurring and edge enhancement respectively. While the proposed nonlinear reconstruction method has decreased stability for short T_2s relative to long T_2s, as visible in tube 7 of (b), the overall error remains consistently low (e). All accelerated methods used 1/4th of the full dataset.

2.4.3: Human experiments

Figure 2.5 shows T_2 maps from the *in vivo* human brain imaging. The upper left frame shows a T_2 map generated from the fully sampled 120° refocused multiple spin echo sequence. Each of the other frames shows a T_2 map derived from a sub-set of the data which could be acquired

in less than $1/6^{th}$ the time; panels b-d were taken from the 120° refocused scan and panels e-f used data refocused by 180° pulses. As in the phantom experiments, ME-CAMBREC generated a T_2 map most closely resembling that of the fully sampled dataset. The middle and lower panels of Fig 2.5, those corresponding to Fourier-reconstructed images, show enhanced artifact such as blurring and asymmetry compared to the maps from fully sampled data and ME-CAMBREC. Unlike in the computational experiment (Table 2.1), fitting *in vivo* high-refocusing flip angle data to the exponential model (Fig 2.5e-f) did not provide better error rates than the proposed method; these error rates were similar to those of maps fitted to the EPG model.

Table 2.2 quantitatively compares the T_2 estimates of various cerebral structures made using accelerated Fourier-based T_2 mapping methods, ME-CAMBREC, fully-sampled data and values from literature. Fully sampled data from the present study agreed well with literature values, showing no systematic bias. ME-CAMBREC accelerated at $R = 6.6$ underestimated T_2 relative to the fully sampled data, but differences were comparable in absolute value to those between the fully sampled data and literature. Similar absolute differences in estimated T_2 resulted from Fourier-reconstruction of $R = 6.6$ EP-trajectory data. The $R = 6.6$ VT-trajectory data underestimated T_2 with somewhat greater absolute differences to fully sampled data. In all cases, voxelwise paired t-tests indicated that differences between fully sampled data from the present study and all accelerated acquisitions were statistically significant.

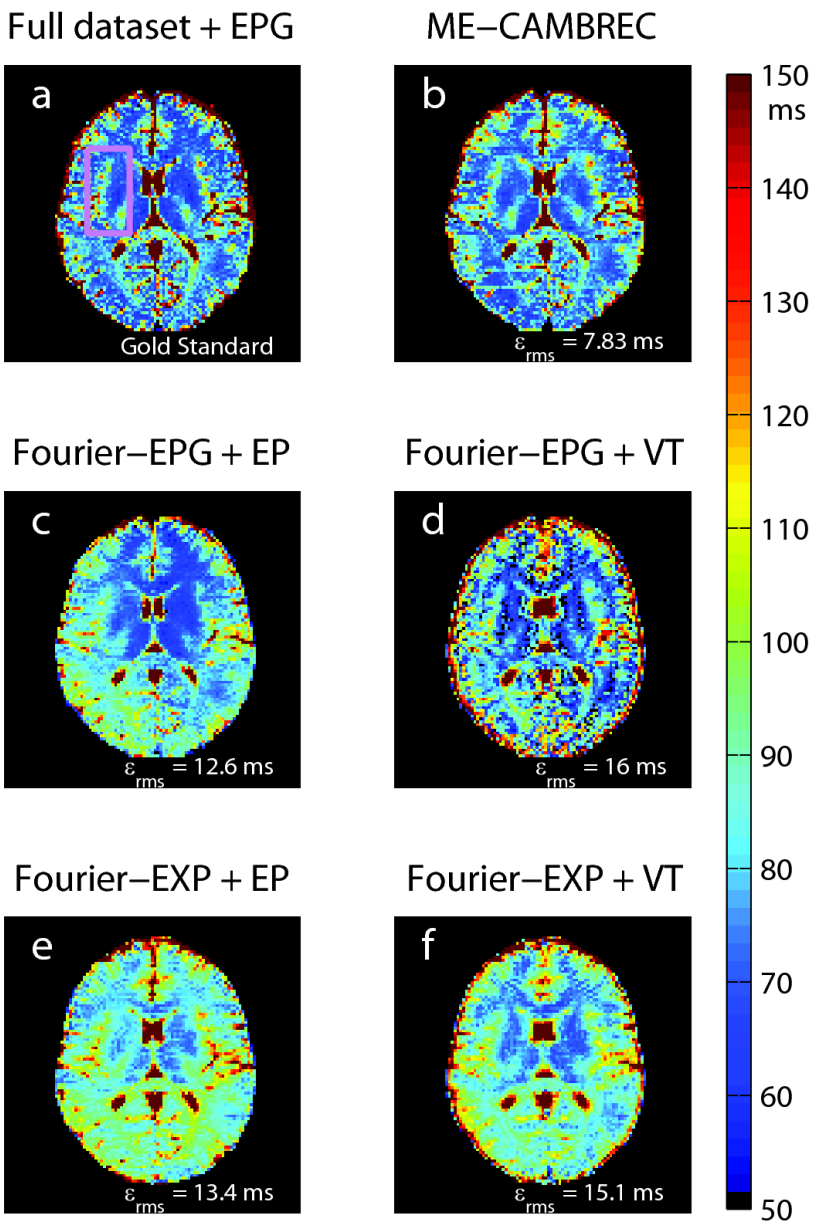

Figure 2.5: Reconstructed T_2 maps in healthy human brain. The pink rectangle in the top-left fully sampled image (a) denotes the ROI used to measure RMS error. Note the asymmetry and systematic overestimation of T_2 in Fourier-reconstructed EP protocols (c,e) as well as the edge enhancement and ghosting artifacts visible in the Fourier-reconstructed VT protocols (d,f). All accelerated methods used $1/6.6^{th}$ of the full dataset ($N_T = 16$); data fit to the exponential model was acquired with a prescribed refocusing flip angle of 180° and was compared to a fully sampled dataset at that flip angle. All other images were derived from data acquired using a prescribed flip angle of 120°.

Table 2.2: Mean T_2 values of various brain regions from literature, fully sampled data, and accelerated methods. All results shown used the EPG model in the T_2 estimation. In all cases, voxelwise paired t-tests indicated that differences between fully sampled data from the present study and all accelerated acquisitions were statistically significant. Values from literature were estimated from Figure 6 in Zhang, et al. *MRM* 2015 (21).

	ROI mean T_2 (ms)				
	Fully Sampled		Accelerated, R = 6.6		
	Literature	Present Study	ME-CAMBREC (R = 6.6)	Fourier-EP (R = 6.6)	Fourier-VT (R = 6.6)
Corpus Cal., Genu	68.2	68.7	66.7	72.3	67.7
Corpus Cal., Splenium	80.4	84.7	80.4	84.2	77.7
Cortical Grey Matter	80.0	84.1	81.3	86.5	74.1
Insular cortex	85.6	83.8	82.0	81.2	74.4
Thalamus	65.6	68.0	66.3	70.6	60.2

The comparison between ME-CAMBREC and SENSE acceleration/EPG fitting is presented in Figure 2.6. At acceleration factor $R = 2$, the methods are comparable, with SENSE performing better in regions with little aliasing and worse in regions with more intense aliasing. At higher acceleration rates ($R = 4$), ME-CAMBREC outperformed SENSE as visible in the left halves of panels e-f. Panel d shows reaching $R = 4$ acceleration by combining sub-sampling in k-space and the echo dimension by a factor of 2 each provided a poorer result than ME-CAMBREC with $R = 4$. That is, one can in principle combine traditional parallel acceleration with ME-CAMBREC, but for this case at least, acceleration by ME-CAMBREC alone was superior.

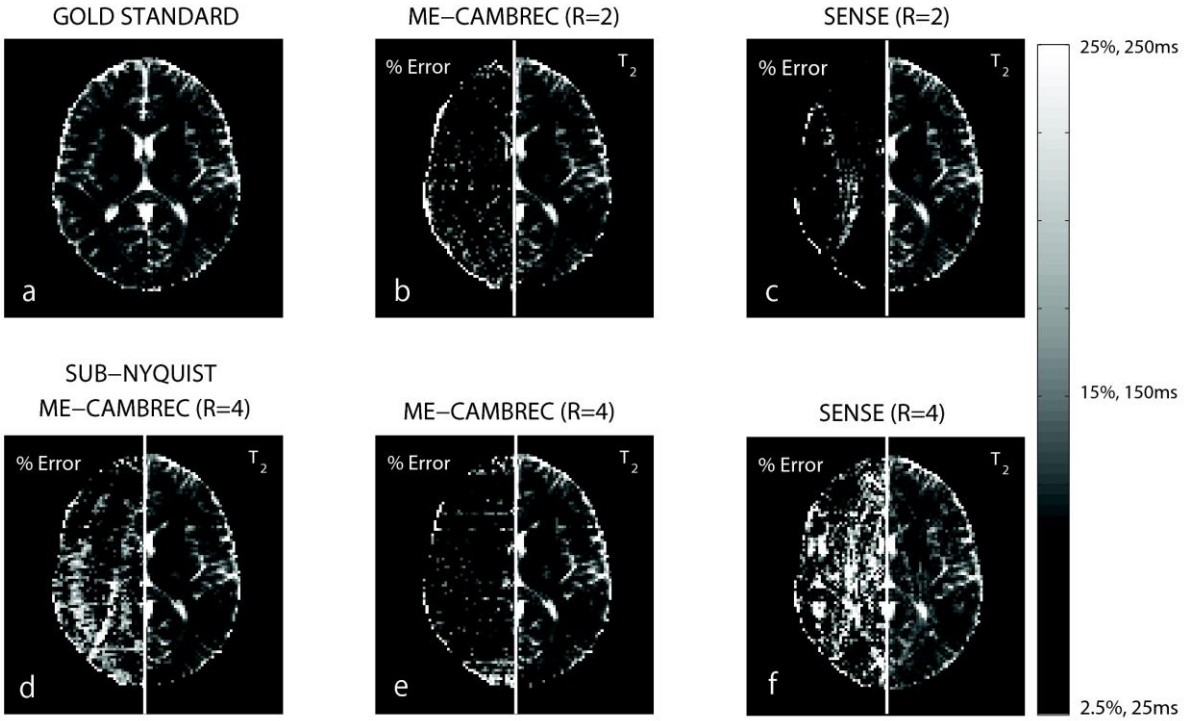

Figure 2.6: T_2 maps from ME-CAMBREC and EPG fitting to SENSE images. The left side of each panel is a relative difference between the given T_2 map and the EPG-fit, fully-sampled, 180° refocused T_2 map. Panels b, d, and e are ME-CAMBREC reconstructions, while panels c and f are T_2 maps from EPG fitting to SENSE-reconstructed images. At acceleration factor 2, SENSE provides better T_2 maps than ME-CAMBREC in regions with little aliasing and worse maps in regions with more severe aliasing (b,c). ME-CAMBREC scales better to higher acceleration factors than SENSE (e,f). Acceleration by the sub-Nyquist sampling of k-space combined with sub-sampling the echo dimension (d) showed a poorer result than acceleration by sub-sampling the echo dimension alone (e).

2.5: Discussion

In experimental environments designed to test noise propagation (computational), artifact and systemic error (phantom), and a combination of the two (human), ME-CAMBREC performed at least comparably to the best conventional FSE methods tested. Noise propagation was kept

similar to Fourier-reconstructed exponential fitting (Table 2.1 and Figure 2.3), despite significant artifact reduction (Figure 2.4). The *in vivo* implementation, where both noise and artifact can contribute to significant errors, gave the greatest advantage over the other accelerated T_2 mapping methods tested. Visually, all ME-CAMBREC images presented here contain smearing artifacts in the phase encode direction which are not smooth in the readout direction, apparently caused by the row-by-row nature of the reconstruction. It is possible that extending the algorithm to jointly fit multiple rows with 2D regularization could alleviate this shortcoming at the cost of computational complexity. There is also an apparent underestimation of T_2 when averaged across regions of interest (Table 2.2) which can be seen in VT Fourier reconstruction fitted to the EPG model as well. This may imply that the artifact is caused by noise amplification at moderate spatial frequencies interacting with the EPG fitting. However, the quantitative errors of these artifacts and underestimation remain lower than those of Fourier-reconstructed fitted T_2 values. While ME-CAMBREC bias, like that of Fourier-based accelerated methods, limits accuracy at high SNR (Figure 2.3), deeper control over regularization-induced bias as compared to image artifact permits T_2 bias to be a somewhat tunable parameter, able to be traded off for estimate precision.

For high acceleration factors, each of the studies presented demonstrated that Fourier-reconstructed EPG fitting induces high errors in T_2 maps. This is not surprising, since the EPG model is a three-parameter model involving oscillating signal behavior: when fitting to a small subset of effective echo times, sensitivity to oscillations (θ) and decay (T_2) must be traded off through the selection of a proximate or disparate set of time points. However, the disagreement between the computational and human studies regarding the expected error of EP-FSE when fit to the exponential model is less parsimonious. The computational study suggests that EP-FSE may be a better option than model-based reconstruction when near ideal refocusing pulses are realized.

As this is a Fourier reconstructed approach, though, the results of EP-FSE will be heavily dependent on the imaging subject's sensitivity to artifact, which has been shown to rely on many additional factors such as feature size and echo train length (60). The large feature size of elements of the Shepp-Logan phantom, combined with the slowly varying underlying T_2 distribution, likely contributed in large part to the apparent superiority of the EP-FSE protocol.

In all experiments, ME-CAMBREC performed at or above the standards of conventional FSE T_2 mapping at a given acceleration factor (from 4 in the phantom experiments to 8 in the computational experiments). However, a wide variety of other fast T_2 mapping methods exist. The proposed method was directly compared to DESPOT2 by way of SNR efficiency, but no experiments were performed to test other aspects of the method which may or may not be limiting factors. For example, DESPOT2 can provide single-slice parameter maps at a slightly faster rate than ME-CAMBREC, although at lower precision due to differences in sensitivity. It should also be noted that DESPOT2 is typically run as a 3D protocol while extending ME-CAMBREC to 3D would be nontrivial. The model-based reconstruction would have to be applied simultaneously in multiple dimensions, both enabling acceleration in a second spatial dimension and creating new challenges in computational stability.

Accelerating using parallel imaging provided excellent results in the case of small acceleration factors ($R = 2$), as Fig 2.6c shows, but at higher acceleration factors ($R = 4$) generally provided poor results compared to ME-CAMBREC. Using ME-CAMBREC itself as a parallel imaging reconstruction method by sampling k-space in the same sub-Nyquist pattern across all pseudo-images provided lower quality results than purely undersampling in the echo dimension (Fig 2.6d-e). This is somewhat intuitive, since the number of echoes acquired is typically many times larger than the number of elements in a receive array, allowing more degrees of freedom in

that dimension. Readers should note that undersampling k-space in a unique sub-Nyquist pattern between pseudo images (e.g., all even k-space lines for one image and all odd lines the next) is essentially equivalent to Nyquist-sampled ME-CAMBREC, since all data are fitted simultaneously.

Another accelerated T_2 mapping method which should be considered is view-shared projection-reconstruction (22,84), such as k-space weighted image contrast (KWIC). One primary advantage KWIC maintains over the ME-CAMBREC is motion insensitivity due to the repeated sampling of the center of k-space. Otherwise, however, KWIC is still somewhat vulnerable to high-spatial frequency image artifact and requires more scan time: the typical KWIC scan requires 32 echo trains, while the highest-accelerated method proposed here used only 16 excitations. Variations on PR-FSE have included a model-based reconstruction (70), which shares certain benefits of ME-CAMBREC with the motion insensitivity and data redundancy of KWIC. While this is certainly advantageous from a problem conditioning perspective, the Cartesian approach used by ME-CAMBREC can be used to separate reconstruction into N_{ro} independent inverse problems, simplifying the computation considerably. Ultimately, this trade-off allows ME-CAMBREC easier implementation and quicker reconstruction at the cost of parameter SNR relative to radial methods.

One other fast T_2 mapping protocol, curve reconstruction via principal component-based linearization with indirect echo compensation (CURLIE), uses PR-FSE, a model-based reconstruction, and the extended phase graph model (57). Although appearing at first glance to be very similar to ME-CAMBREC, CURLIE uses training data to effectively remove artifact from images using linear decompositions, then performs a voxelwise fitting to the EPG model. Thus, compared to the proposed method, CURLIE has major computational advantages, but applies an intermediate principal component-space rather than attempt to directly fit k-space signal to an

underlying model. In the same vein, compressed sensing-based protocols which utilize sparse spaces in the parametric (TE) dimension (74) or a similar "model dictionary" dimension (73) can theoretically be used with the EPG model for accelerated T_2 mapping, especially when combined with a pseudo-random acquisition scheme.

Implementing ME-CAMBREC for volumetric coverage will present challenges for two reasons. As presented here, ME-CAMBREC used wider refocusing pulses compared to the excitation pulse, thereby requiring a slice gap if one wanted to implement a multi-slice acquisition. In principle, this limitation can be overcome by incorporating the known RF profiles into the reconstruction model, similarly to prior work (56). Also, under certain circumstances, multi-slice multiple spin echo acquisitions may be limited by specific absorption rate (SAR). However, ME-CAMBREC does offer the ability to use low-angle refocusing pulses without sacrificing image quality or quantitative accuracy, and this feature may be exploited to reduce the stringency of SAR limits or accelerate further by extending echo trains at the cost of added T_1 bias.

Finally, it should be noted that ME-CAMBREC as presented does not accommodate or account for multi-compartmental transverse relaxation, as is known to occur in cerebral white matter due to the presence of myelin (3) and will occur whenever individual voxels include partial volume averaging of two or more tissues with widely different T_2. One would expect this to be a particular problem in brain regions neighboring cerebrospinal fluid, although Figures 2.5 & 2.6 and a cursory analysis of data therein did not indicate any widespread problem. Extension of ME-CAMBREC to account for multi-compartmental transverse relaxation would likely be SNR-limited and non-trivial to make effective. ME-CAMBREC will face similar challenges/limitations when motion or physiological noise sources significantly alter the signal from the model, although further study is necessary to assess such challenges.

2.6: Conclusions

The work presented here has demonstrated a novel regularized model-based reconstruction algorithm for generating T_2 maps from undersampled multi-echo data, such as those acquired via FSE sequences. A Cartesian acquisition scheme which is better tailored to its advantages than previously established k-space trajectories was also proposed and evaluated. The proposed method, dubbed Multiple Echo, Caesar cipher Acquisition and Model-Based REConstruction (ME-CAMBREC) generated T_2 maps with low error in computational, phantom, and human studies, and was demonstrated to be more efficient than a comparably accelerated non-FSE relaxometry protocol (DESPOT2). While other accelerated methods may have particular advantages, such as motion insensitivity, the ease of implementation of ME-CAMBREC combined with its demonstrated accuracy and precision, make it a potentially valuable tool in both research and clinical environments.

CHAPTER 3

BIASING FACTORS IN ME-CAMBREC

3.1: Introduction

In the previous chapter, it was shown that multiple echo, Caesar cipher acquisition and model-based reconstruction (ME-CAMBREC) T_2 maps are quantitatively similar to those constructed by fitting fully sampled multi-echo images to the extended phase graph (EPG) model. Despite the method's promising results for acceleration factors up to and including R=6, the sources of T_2 estimate error in ME-CAMBREC are not well understood. It is therefore the objective of this chapter to examine a number of the method's assumptions and, through simulation, determine the most prominent sources of T_2 bias in ME-CAMBREC. The remainder of this section is an overview of potentially biasing assumptions in ME-CAMBREC. (Note that this chapter does not cover the influence of T_1 constraint. Lebel and Wilman showed that the EPG signal model is not highly sensitive to T_1 (56), and a comparable model-based reconstruction method was recently shown to be insensitive to this source of bias (55).)

One of the assumptions utilized in ME-CAMBREC is slice-profile uniformity. As ME-CAMBREC is an accelerated 2D imaging method, the ability to acquire multiple slices in the same repetition time (TR) is critical—thus, interleaved slice-selective radiofrequency (RF) pulses must be employed. Slice-selective pulses are inherently nonuniform due to the necessary flip angle fall-off outside the slice. In the previous chapter, double-wide refocusing pulses were employed to improve uniformity inside the excited slice (44), but this precludes the acquisition of contiguous

slices and will not entirely eliminate the contribution of profile effects to T_2 error. It is therefore important to investigate the effect of slice profile on reconstructed T_2 maps, and furthermore, to determine if a smaller refocusing pulse width could be used without sacrificing T_2 accuracy.

Transverse relaxation mapping through ME-CAMBREC also assumes a single-compartment decay model, which is not the case in tissues such as white matter (3,34), nor in voxels with partial-volume signal averaging. Two broad types of multi-compartment decay models have been applied to brain tissue: multiple water compartment models, such as the myelin water model of white matter, and macromolecular pool models (35,89). While the former will affect single-compartment estimates of T_2 such as those of ME-CAMBREC, the latter will reduce initial excited signal (90,91), M_+, but not the measured T_2—all off-resonance saturation occurs outside the echo train.

Another source of T_2 error in ME-CAMBREC is introduced by design in the form of regularization bias. When the M_+ regularization factor, λ, is small, noise amplification in the image reconstruction process will degrade image quality. On the other hand, over-regularization (i.e., when λ is large) will introduce bias to all fitted parameters. The following chapter will therefore simulate the effects of under- and over-regularization, as well as address the unanswered questions regarding slice profile and multi-compartmental relaxation effects on measured T_2 values.

3.2: Methods

In all of the following simulations, the true values for T_2 (or signal fraction, in the case of multi-compartment relaxation) were positioned within a computational phantom at varying feature sizes, as shown in Figure 3.1. Features of width between 1 and 96 voxels, the full object width

within a 128-point field of view, were simulated in order to determine the effects of biasing factors on image elements of varying size. All simulations used the EPG signal model, and assumed an acquisition train of 32 echoes spaced 8 ms apart. Retrospective undersampling was performed in the Caesar-cipher pattern (92) with eight four-shot fast spin echo (FSE) pseudoimages, corresponding to a total acceleration factor R = 4.

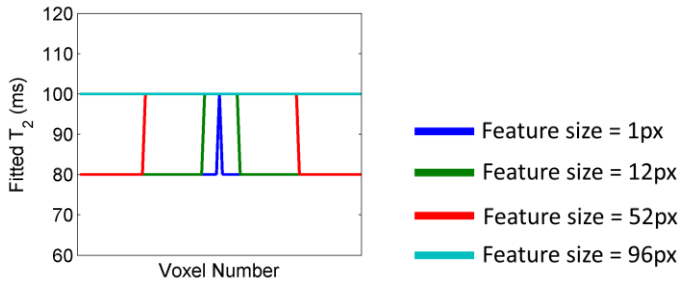

Figure 3.1: The computational phantom used for regularization and slice profile experiments. The T_2 value changed from 80 ms to 100 ms in features of varying size, with the largest feature representing the entire object and the smallest feature a single voxel. A similar phantom was used for the multi-compartmental decay experiments, but the features of varying size represented regions of multi-compartmental decay rather than a different single-compartment T_2 value. The T_2 values used were also different in the multi-compartmental experiments.

3.2.1: Regularization bias

In order to determine the nature of regularization artifact in ME-CAMBREC, image profiles were reconstructed with regularization parameters between 10^{-4} and 10^{2} (in arbitrary units). The phantom T_2 was 80 ms with features in which T_2 = 100 ms, as in Figure 3.1. In order to avoid converging to the exact solution and better represent an actual measurement, complex Gaussian noise was added with magnitude standard deviation equal to 1% of M_+, corresponding to an image signal-to-noise ratio (SNR) ≈ 100.

3.2.2: Slice profile effects

The Bloch equations were solved to generate flip angle profiles for a slice-selective refocusing scheme (five-lobed sinc shape; full-width, half-max (FWHM) = 1x and 2x excitation width). The profiles were discretized to 400 isochromats of individual bandwidth equal to 1/100th the excitation FWHM, as in (56), and the slice-resolved EPG simulation was used in forward simulations. In order to characterize the bias caused by ME-CAMBREC's assumption of uniform flip angle, reconstructions of data from slice-selective refocused (1x and 2x width) simulations were compared to those of uniformly-refocused (e.g., through hard-pulse refocusing) simulations. The phantoms used were identical to those in the previous section and Figure 3.1. As slice profile shape and therefore uniformity is highly dependent on flip angle, this was repeated for peak flip angles of 140, 180, and 220 degrees, as well as for two acceleration factors, R=2 and R=4. The regularization parameter was set to zero for all reconstructions in this experiment. In addition to T_2 map evaluation, reconstructed refocusing pulse flip angle (θ) maps were compared to θ values obtained through fully-sampled EPG fitting.

3.2.3: Multi-compartmental relaxation

Simulated images were calculated with T_2 pairs of 15/80, 30/250, and 80/1000 ms. These three pairs were chosen to roughly represent the two T_2 values observed in white matter, partial-volume averaging between fat and muscle, and partial-volume averaging between brain tissue and cerebrospinal fluid (CSF), respectively. These circumstances were chosen in order to evaluate conditions in which the *apparent* T_2s—the biased T_2s determined by single-compartment

analysis—were moderate compared to the echo spacing (white matter), on the order of the echo spacing (muscle), and long compared to the echo train (CSF). The signal fractions of myelin water, fat, and CSF were arbitrarily assigned a value of 20% within the image features of varying size, and 0% outside the features. In addition to properly reconstructed images, under- and over-regularized reconstructions were computed in order to determine the combined effects of varying regularization and model inconsistency. Each ME-CAMBREC reconstruction was compared to the apparent T_2s obtained by fitting fully-sampled simulated data to the (one-compartment) EPG model.

3.3: Results

3.3.1: Regularization bias

The reconstruction profiles at five values of λ are shown in Figure 3.2. For the lowest two values of λ, T_2 was biased within features of moderate size. Higher levels of regularization generated artifacts in the T_2 maps at the edges of the object, leading to gross overestimation of T_2 in these regions at the highest levels of regularization. Inside the object, features of larger size were found to be more accurate as regularization increases, while smaller features were intuitively more biased. As observed previously, T_2 noise decreased between the lowest value of λ and the optimal value, $\lambda = 0.05$. The overall trend of model-based reconstructions to spread artifact to surrounding voxels is visible in the red curves in the upper row of panels; negative T_2 bias in the $T_2 = 100$ ms feature was accompanied by a positive T_2 bias outside the feature.

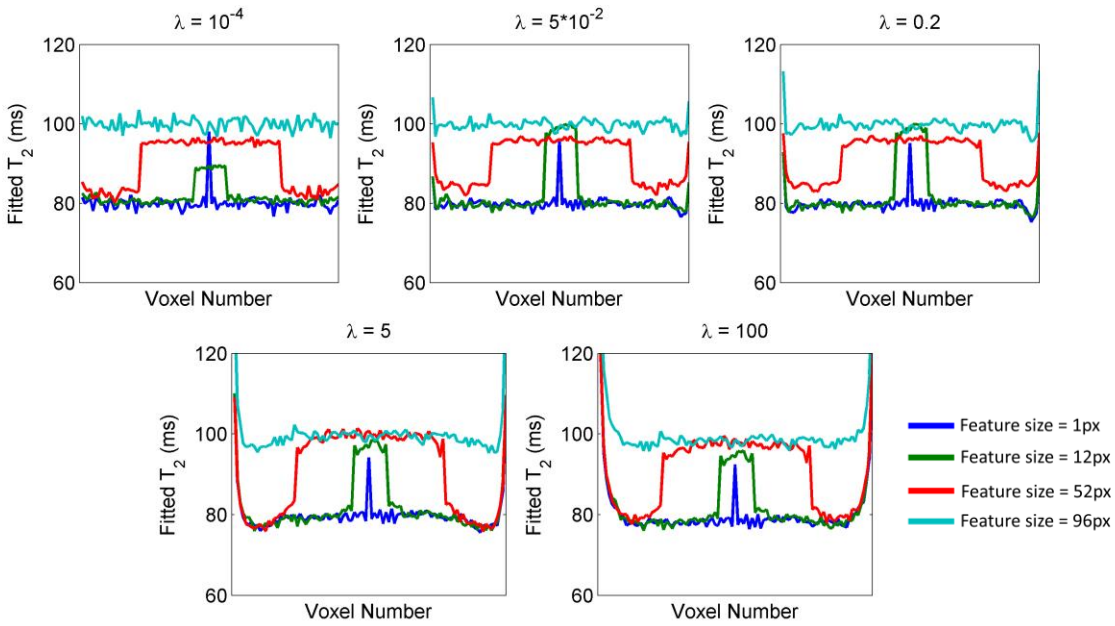

Figure 3.2: T_2 reconstructions at various λ values. Each curve represents a phantom with a different-sized T_2 = 100 ms feature. The horizontal axis represents the voxels within a 96-point object in a 128-point field of view. As regularization increases, larger features become more accurate and noise decreases to a minimum, but smaller features lose accuracy and, most prominently, T_2 is highly overestimated at the object's edges.

3.3.2: Slice profile effects

The quality of reconstructed T_2 maps was found to be highly dependent on refocusing pulse slice width, and less dependent on transmitted flip angle. Figure 3.3 shows a significant decrease in T_2 map accuracy when moving from double-width (bottom row) to single-width refocusing (middle row). At the same acceleration factor, T_2 estimates from single-width refocused simulations had large noise-like variations as well as systematic overestimation of T_2; at lower acceleration factors, single-width refocused simulations experienced less noise-like variation, but the systematic overestimation remained.

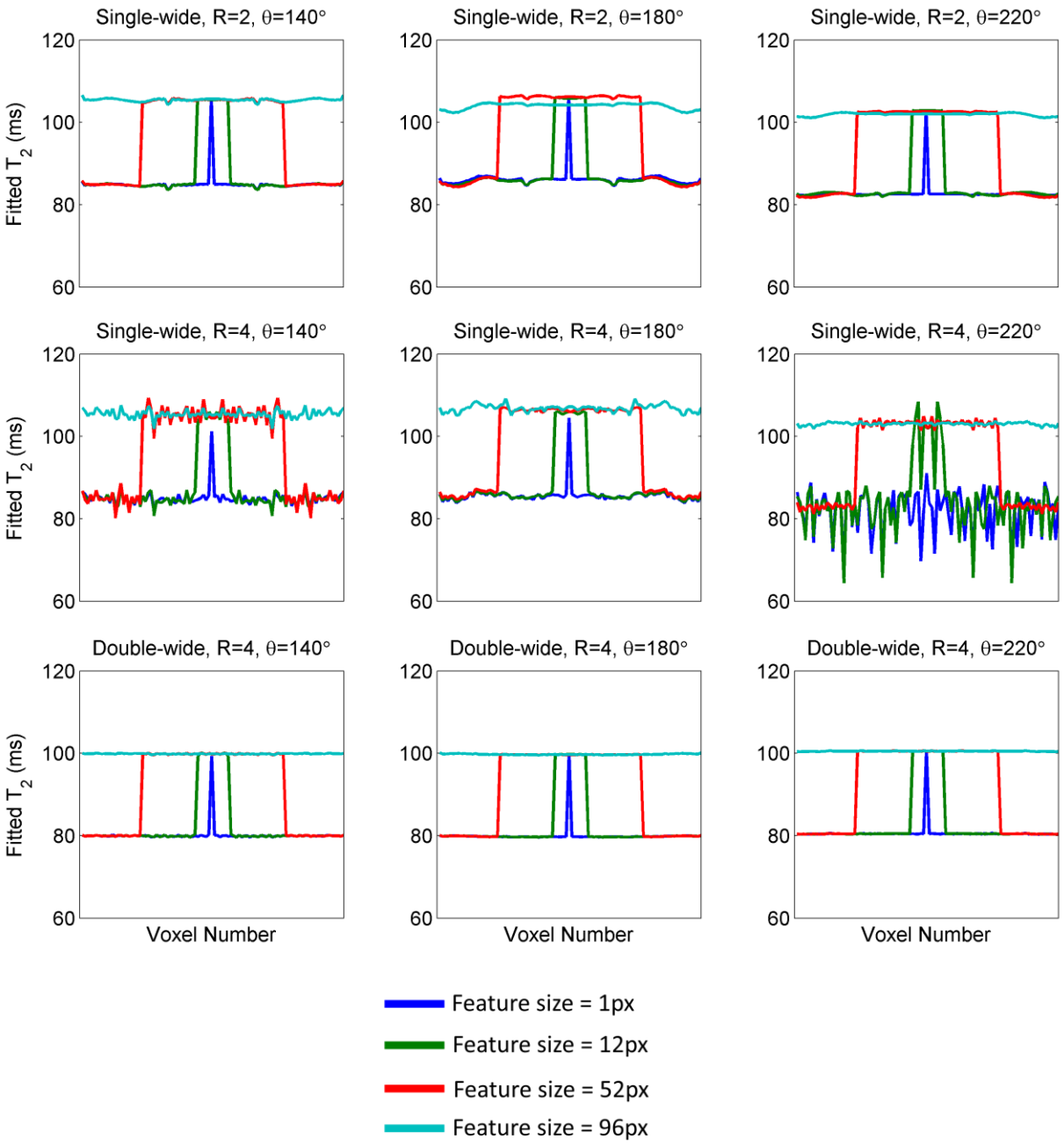

Figure 3.3: ME-CAMBREC T_2 reconstructions as a function of refocusing pulse qualities. The true T_2 values are 80 ms and 100 ms. At a low acceleration factor (R=2, top row), refocusing pulses with slice width equal to the excitation width provided reasonable but overestimated T_2 values. Single-width pulses provided more erratic and flip angle-dependent results at higher acceleration factors (R=4, middle row). Refocusing pulses twice the width of the excitation pulse (bottom row) provided accurate T_2 values when fit using ME-CAMBREC's isochromatic refocusing model.

It should be noted that fitted flip angles showed artifactual in-plane variation when the refocusing pulse width matched the excitation pulse width. The θ maps in Figure 3.4 and the corresponding T_2 maps in Figure 3.3 (center column) demonstrate artifacts with similar shape, demonstrating the covariance of the ME-CAMBREC joint reconstruction. Mean reconstructed flip angles were similar to the apparent flip angles observed by fitting fully-sampled images to the (isochromatic) EPG model. For example, a double-wide refocusing pulse with peak flip angle 220° provided data that fitted to an isochromat experiencing θ = 139.8° pulses; the average ME-CAMBREC reconstructed flip angle was θ = 139.9°, a 0.07% difference.

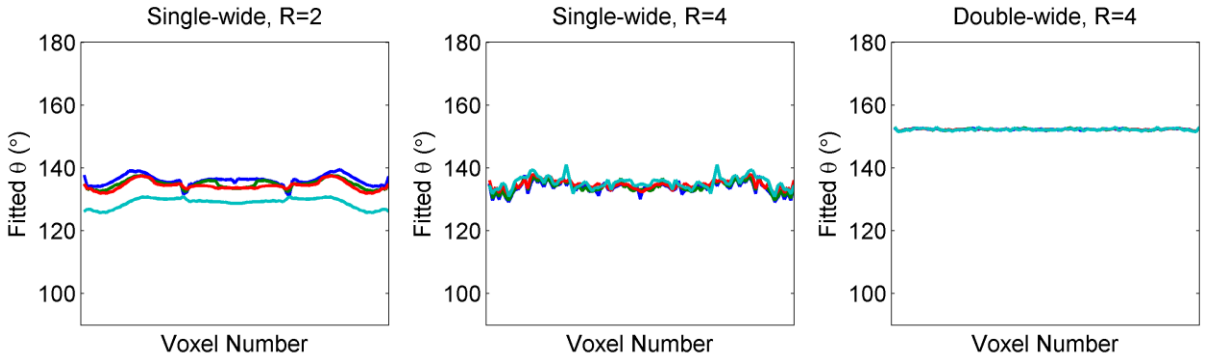

Figure 3.4: Flip angle reconstructions of selectively-refocused simulated data. The true peak flip angle was 180°, corresponding to an apparent flip angle of 138.2° for a refocusing pulse of equal width to the excitation pulse (left and middle) and 152.1° for a refocusing pulse twice that width (right). There is artifactual in-plane variation when using single-width refocusing pulses, but not when using double-width pulses.

3.3.3: Multi-compartment relaxation

Multi-compartment features in ME-CAMBREC did not in general match the fully-sampled estimates of apparent T_2, which are represented by the dotted lines in Figure 3.5. Over-regularized reconstructions (right column) were biased both within regions with multiple decay compartments

and outside those regions, and this bias was highly dependent on feature size. For under- and moderately-regularized reconstructions, T_2 maps were more accurate and demonstrated less spatial variation when the apparent T_2 was within the range of maximal pulse-sequence sensitivity; i.e., when T_2 was much larger than the first echo time, yet much smaller than the last. For example, the short muscle-like T_2 (30 ms, compared to 8 ms echo spacing) caused sizable fluctuations in panel d of Figure 3.5, and the long CSF-like T_2 (1000 ms, compared to the final echo time at 256 ms) caused bias in panel h that was feature-size dependent. It should be noted, though, that the bias in features with CSF-like partial volume averaging did not strongly affect accuracy outside the feature. Each under- and moderately-regularized reconstruction slightly underestimated the fully-sampled apparent T_2 in voxels with multiple decaying species.

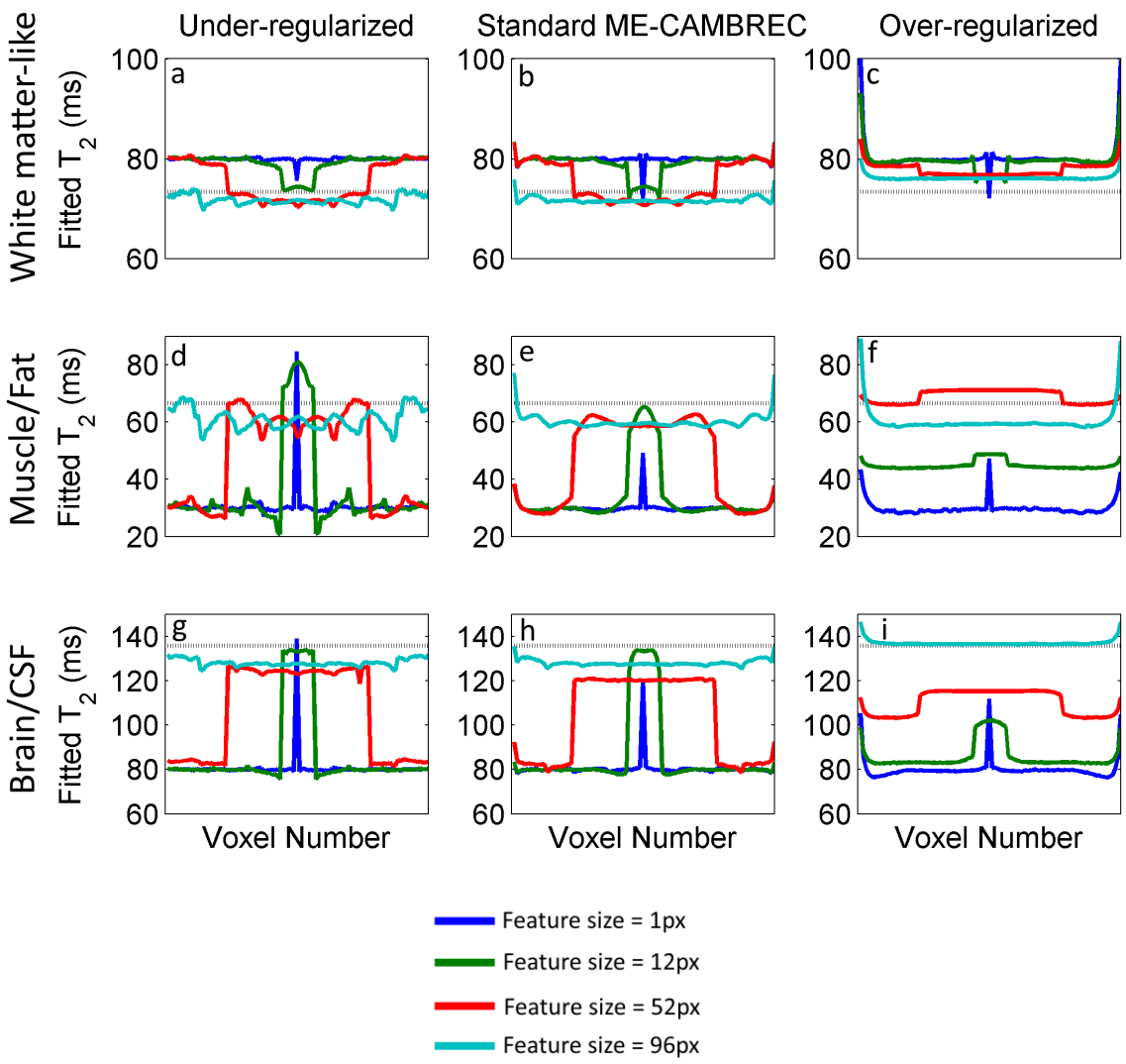

Figure 3.5: ME-CAMBREC T_2 reconstructions of underlying multi-compartmental signals. The dotted lines mark the value of the apparent (single-compartment) T_2 for each two-compartment feature. Over-regularization (c,f,i) causes large feature size-dependent bias. For tissues like white matter with apparent T_2 within the range of sensitivity (a-c), ME-CAMBREC performs well with moderate regularization. Regions containing apparent T_2 values outside the sensitive range (all of d-f and the two-compartment features in g-i) were significantly less accurate, producing spatial variations in T_2 (d-e) or feature size-dependent T_2 bias (g-h).

3.4: Discussion

The relationship between over-regularization and sharp overestimation of T_2 at the edge of the object is intuitive. As regularization in ME-CAMBREC forces similarity between the M_+ map and the first pseudoimage, which is a center-out, Cartesian fast spin-echo image, reconstructing using a large value of λ will effectively constrain M_+ to a blurred image. This blurring manifests as a gradual *falloff* in M_+ at the edges, which forces an increase in fitted signal longevity (i.e., T_2) in those regions to compensate and better match the observed k-space data. This causes T_2 to be overestimated at sharp edges in the M_+ map. It is noteworthy that this artifact does not occur at edges in the T_2 map, but at edges in M_+, or more specifically, in the first pseudoimage. The relationship between regularization quality and the quality of the first pseudoimage also implies a need to ensure a fairly large refocusing pulse flip angle, θ. Low-θ signal decay includes stimulated echoes and accompanying oscillations, and will cause sharp edges in the first pseudoimage's attenuation function. In turn, this will cause ghosting in the pseudoimage and all reconstructed maps. While the over-regularization artifact may seem innocuous when many imaging targets are deeper than the outermost voxels, such as in brain imaging where these artifacts would manifest within subcutaneous fat and CSF, Figure 3.5 more clearly shows the dangers of over-regularization. When model inconsistencies such as multi-compartmental behavior are smoothed through regularization, feature size-dependent bias will occur. Regularization weight should thus be kept below levels which induce noticeable edge enhancement in the T_2 map.

Using refocusing pulses equal in width to the excitation pulse, while necessary to acquire contiguous slices in one repetition time, comes at a large cost in ME-CAMBREC and is not recommended. In addition to a general overestimation of T_2 caused by stimulated echoes at the

edge of the slice (44), spatial variation is introduced into the T_2 maps. Although this spatial variation is not larger than practical noise variations for low acceleration factors—compare Figure 3.2 and the top row of Figure 3.3—a moderate acceleration factor combined with single-width refocusing introduces computational instabilities to the reconstruction. This is most notable in image lines with small features, potentially due to these lines' dependence on accurate high-spatial frequency information.

A recent study (58) suggested that the fitted flip angles from EPG analysis do not exactly correspond to measured transmit field (B_1^+) or flip angle maps. Although ME-CAMBREC flip angle maps did correspond well to those fitted to the isochromatic EPG model, they did not match the average flip angle calculated as the inner product of the excitation profile and refocusing flip angle profile. The difference between the *apparent* (to EPG analysis) flip angle and *average* flip angle was over 10% for a single-wide refocusing pulse with peak $\theta = 180°$. Interestingly, this deviation dropped to <2% for the double-wide refocusing pulse.

ME-CAMBREC performed poorly when reconstructing multi-compartment signals containing long T_2 values, such as CSF, or when the signal decays away quickly compared to the echo spacing, such as in muscle. In the former case, T_2 estimates outside the long-T_2 feature were accurate, but estimates of the long T_2 were biased in a feature size-dependent manner. The muscle-like computational phantom required extensive regularization to reconstruct a smooth profile, as visible by the overestimation of T_2 at the edges of Figure 3.5e, and regardless of regularization level, feature size-dependent bias existed in the T_2 maps. In contrast, the white matter-like T_2 was biased by <2 ms in a size-independent manner when reconstructed with optimal regularization. For an undersampled model-based reconstruction method like ME-CAMBREC, this is often within the practical noise level (55,57).

It is well-known that a multiple spin echo-based T_2 mapping method will be most sensitive to T_2 values between the pulse sequence's first and last echo times. As model-based reconstruction methods can potentially spread the error from poorly fit voxels to nearby voxels, one might expect ME-CAMBREC and similar protocols (52,55,57,70,72,75) to experience large bias at the edge of CSF-contaminated regions, in which the T_2 is ill-determined. However, Figure 3.5g-h shows this is not the case: although the CSF-contaminated T_2 is erroneous in a feature size-dependent manner, the adjoining T_2 = 80 ms region is estimated accurately. It is reasonable to assume this result applies to other model-based methods; an important exception is the generating function family of methods (55), as these utilize a model which is violated by the truncation of the echo train before signal decay is complete (54). A similar argument can be made from Figure 3.5e, with the caveat that ME-CAMBREC is less sensitive to the short T_2 of muscle than the moderate T_2s found in brain, and therefore requires more regularization and, in practice, higher SNR.

The general underestimation of apparent T_2—compared to voxelwise EPG analysis, the dotted lines in Figure 3.5—in regions with multi-compartmental decay is not immediately intuitive. One possible explanation is that the undersampling pattern inherent to ME-CAMBREC is causing the spuriously large first echoes (at least, compared to a true single-compartment decay) to present as an increase in low-spatial frequency signal during early echoes. This could cause an overestimation of M_+ and a corresponding underestimation of signal longevity—particularly a spatially uniform or slowly-varying underestimation as seen in Figures 3.5b and e.

This analysis did not investigate the effects of T_1 constraint bias. Although this has been studied previously for simple cases of erroneous constraint (56), the effects of biexponential T_1 relaxation on the EPG fitting algorithm—such as can be seen in the presence of a macromolecular pool (93)—have not been previously considered. Due to the high-θ MSE pulse sequence's overall

insensitivity to T_1, it is not expected that this effect plays a large role in signal determination, but this should be explicitly investigated in the future.

3.5: Conclusions

This chapter has qualitatively characterized a number of biasing factors in T_2 maps generated by ME-CAMBREC, including regularization bias, slice profile nonuniformity, and multi-compartmental decay. The results show that image quality is best preserved by ensuring regularization is not unduly weighted, as this can cause edge enhancement in T_2 maps. The risks of using narrow refocusing pulses in order to acquire contiguous slices were clearly presented—such protocols will overestimate T_2 and may cause computational instability at moderate acceleration factors. ME-CAMBREC was shown to provide accurate, though slightly underestimated, apparent T_2 values for multi-compartmental signals, provided the apparent T_2s are well-defined by the user's choice of echo time and echo train length. When a voxel does present a compartment with an impractically long T_2, such as that of cerebrospinal fluid, the contaminated voxels will be assigned biased T_2 estimates, but the T_2 of surrounding voxels will be estimated accurately.

CHAPTER 4

T_2 MAPPING WITH FITTED VS. MEASURED B_1^+: A STATISTICAL ANALYSIS

This chapter is adapted from an article in the late stages of preparation which is to be submitted to *Magnetic Resonance in Medicine*. Its authors are Christopher L. Lankford and Mark D. Does. The sections specifically pertaining to ME-CAMBREC have been added for greater depth.

4.1: Introduction

Accurate T_2 mapping with a multiple spin echo imaging sequence requires accounting of stimulated echoes from indirect signal pathways (49,53,94), which typically employs the joint fitting of T_2 and refocusing flip angle, θ. Useful signal models for such analysis include the extended phase graph model (EPG (20,46,53,56,81)), the echo generating function (GF (54,55)), and the Bloch equations (51,52,58). For an appropriate multiple spin echo sequence, each of these models can be used to determine the echo magnitude from a voxel given four input values: equilibrium magnetization (M_0), the relaxation time constants T_1 and T_2, and the refocusing pulse flip angle (θ). Due to the relatively weak T_1-dependence of multiple spin-echo signals, T_1 is generally fixed to an approximate value and subsequently ignored (20,51,52,55–58,81,92). This leaves three unknown parameters to be jointly fitted from the measured echo magnitudes; alternatively, one can independently measure θ from a B_1^+ mapping method (95–99) and then fit

only M_0 and T_2. To date, there is no clear analysis of the advantages/disadvantages of these two options.

It is well-known that constraining some parameters in a joint fit will generally improve the precision of the remaining fitted parameters, potentially at the cost of imparting bias. Note that even with a biased fitted parameter, the mean-squared error, ε_{T2}^2, which is the sum of an estimate's variance and squared bias, may actually decrease overall (100). Constraint of the θ parameter should therefore be considered in the analysis of multiple spin echo data. The objective of this work is to quantify and characterize the relationships between the accuracy and precision of T_2 from multiple spin echo data, computed with and without independent measurements of θ.

4.2: Theory

When simultaneously estimating a vector of tissue parameters, **z**, from a Gauss-distributed signal vector, **s**, one can use the Cramér-Rao Lower Bound (CRLB) to estimate the covariance matrix of **z**,

$$\mathbf{\Sigma_z} = \left(\mathbf{J}^T \mathbf{\Sigma_S}^{-1} \mathbf{J}\right)^{-1}, \qquad [4.1]$$

where **J** is the signal model Jacobian matrix populated by values of $\partial\mathbf{s}/\partial\mathbf{z}$ values, and $\mathbf{\Sigma_s}$ is the covariance matrix of the signal noise. In most cases, $\mathbf{\Sigma_s}$ reduces to an identity matrix scaled by the noise variance of the measured signal ($\sigma_\mathbf{s}^2$). The variance of a particular fitted parameter (e.g., $\sigma_{\hat{T}_2}^2$) can be extracted from the relevant diagonal element of $\mathbf{\Sigma_z}$.

For an unbiased estimate, the mean-squared error (ε^2) of a given parameter is equal simply to its variance (e.g., $\varepsilon_{\hat{T}_2}^2 = \sigma_{\hat{T}_2}^2$). However, when one element of **z** (e.g., θ) is constrained to an

independently measured value (e.g., a flip angle estimate, $\hat{\theta}$), the mean-squared error of each of the remaining fitted parameters includes more than the variance caused by noise in **s**. The approximation used here for the mean-squared error of $\hat{T}_2$ is

$$\varepsilon_{\hat{T}_2}^2 \approx {\sigma_{\mathbf{s}}}^2 \left(\mathbf{J}_{M_0,T_2}^T \mathbf{J}_{M_0,T_2} \right)^{-1}_{T_2,T_2} + \sigma_{\hat{\theta}}^2 \left(\frac{\partial \bar{T}_2}{\partial \hat{\theta}} \right)^2 + \left(\bar{T}_2 \left(\bar{\theta} \right) - T_2 \right)^2, \qquad [4.2]$$

where the bar notation denotes the average estimate of a parameter, and the subscripts of matrices in the leftmost term imply a selection of only the columns and/or rows corresponding to the given parameters. The leftmost term is the constrained CRLB of the variance of an unbiased $\hat{T}_2$ given an accurate θ constraint. The middle term is the propagation of noise from the flip angle estimate, $\hat{\theta}$, to the T_2 estimate, $\hat{T}_2$. The rightmost term represents the squared bias in $\hat{T}_2$ caused by bias in $\hat{\theta}$. In general, constraint of θ will decrease the leftmost term relative to the comparable term in Eq. [4.1], but will result in nonzero values of the middle and rightmost terms depending on the precision and accuracy of $\hat{\theta}$, respectively. Thus, to reduce the value of $\varepsilon_{\hat{T}_2}^2$ by constraining $\theta = \hat{\theta}$, $\hat{\theta}$ must be sufficiently precise and accurate. A derivation of Eq. [4.2] is presented in Appendix 2.

4.3: Methods

In order to evaluate the effects of using independent measures of refocusing pulse flip angle in T_2 fitting, Equations [4.1] and [4.2] were evaluated for a variety of scenarios. In all cases, calculations were performed using tissue parameters similar to those found in human brain at clinical field strengths (T_1 = 1000 ms, T_2 = 80 ms). All calculations used the extended phase graph (EPG) algorithm as the underlying signal model with T_1 constrained to the true value of 1000 ms.

To evaluate the partial derivative terms in the Jacobian matrix, a forward difference approximation was used with a step size 1×10^{-6} times the parameter value. The partial derivative $\partial \bar{T}_2 / \partial \hat{\theta}$ was estimated by fitting T_2 without added image noise and performing a center-difference approximation across the true value, taking $\hat{\theta} = \theta \pm 1°$.

Two different echo train lengths were investigated, corresponding to the extremes of common T_2 mapping protocols. The first was a 32-echo protocol with echo spacing (ESP) = 10 ms, and the second was a four-echo protocol with ESP = 30 ms. In each case, two refocusing schemes were evaluated: i) a nonselective, rectangular refocusing pulse, and ii) a five-lobed sinc-shaped slice-selective pulse with FWHM 2× that of the excitation pulse. For the simulations of slice-selective refocusing, the flip angle profile was calculated through numerical solution of the Bloch equations for each nominal flip angle, θ. Although the forward simulation employed a Bloch-simulated slice profile, both profile-corrected and uncorrected T_2 fitting methods were considered in the analysis.

4.3.1: The effect of θ constraint on $\hat{T}_2$ precision

The propagation of noise from an unbiased measure of the flip angle to the estimate $\hat{T}_2$ was evaluated for all tested protocols (4- and 32-echo, non- and slice-selective refocusing, with and without profile correction) and with various actual flip angles. Equation [4.1] was used to calculate $\varepsilon^2_{\hat{T}_2}$ when jointly fitting T_2, M_0, and θ, and Eq [4.2] was used for the same purpose when θ was constrained to an unbiased estimate, $\hat{\theta}$. (Note that the third term of Eq. [4.2] was equal to zero in this scenario, as $\hat{\theta}$ and therefore $\hat{T}_2$ were unbiased.) The standard deviation of noise added to the

signal was set as $\sigma_s = 0.01 \times M_0$; thus, the image signal-to-noise ratio was $SNR_s \triangleq M_0/\sigma_s = 100$. Calculations were repeated for θ values over the range [90°, 180°] and with $SNR_{\hat{\theta}} = 25$, 50, 100, and ∞. The resulting $\hat{T}_2$ precision, reported as $SNR_{\hat{T}_2}$, scales linearly with SNR_s as long as the ratio $SNR_{\hat{\theta}}/SNR_s$ is constant, and thus the chosen SNR_s value is arbitrary within the regime of the approximation.

4.3.2: The effect of θ constraint on $\hat{T}_2$ accuracy

If the independent measure of flip angle is biased, then the resulting estimate of T_2 will also be biased, and this effect is captured by the third term of Eq [4.2]. Values of $\bar{T}_2\left(\hat{\theta}\right)$ were calculated by estimating $\hat{T}_2$ using $\hat{\theta}$ = [90°, 180°] for four different values of θ: 90°, 120°, 150°, and 175°. As above, this was repeated for all tested protocols (4- and 32-echo, non- and slice-selective refocusing, with and without profile correction). Next, the level of θ-bias was determined at which independently-measured and jointly-fitted θ resulted in the same $\varepsilon^2_{\hat{T}_2}$. This evaluation was performed with nonselective refocusing pulses only; including slice selective refocusing would simply add an independent and predictable bias to $\hat{T}_2$ related to the definition of the flip angle as peak θ rather than apparent or average θ, as briefly discussed in Chapter 3.

4.3.3: Monte Carlo simulations

In order to validate calculations of $\varepsilon^2_{\hat{T}_2}$ using Eqs [4.1] and, in particular, [4.2], Monte Carlo simulations were performed in which $\hat{T}_2$ was fitted from noisy multiple spin echo data and, where relevant, constrained to a noisy and/or biased $\hat{\theta}$. Gaussian noise was added to the simulated signals and flip angle estimates at levels corresponding to $SNR_{\mathbf{S}}$ = 100 and $SNR_{\hat{\theta}}$ = 100, respectively. Both unbiased ($\bar{\theta} = \theta = 150°$) and biased ($\bar{\theta} = 155°$; $\theta = 150°$) scenarios were tested. The 32-echo, nonselective refocusing protocol was used. Each calculation was repeated 10,000 times with independent realizations of noise, and $\varepsilon^2_{\hat{T}_2}$ values were compared to those predicted by Equations [4.1] and [4.2].

4.3.4: θ constraint in ME-CAMBREC

The predicted precision and accuracy changes for fully-sampled T_2 maps generated through θ constraint were compared to T_2 maps from θ-constrained ME-CAMBREC. Simulated pseudoimages assumed phase-encoded matrix size = 128, ETL = 32, and 8 pseudoimages, for an acceleration factor R = 4. Slice-selective refocusing pulses with FWHM double that of the excitation pulse were simulated. The T_2 values and spatial configurations in Figure 3.1 were taken as underlying truth—T_2 was equal to 80 ms and 100 ms. Noise was added to the images at a level consistent with $SNR_{\mathbf{S}}$ = 200, which for R = 4 should provide T_2 maps of comparable quality to fully-sampled images with $SNR_{\mathbf{S}}$ = 100. Reconstructions were repeated for fitted-θ and for three θ-constrained protocols: i) $\hat{\theta} = \theta_{peak}$, the peak flip angle; ii) $\hat{\theta} = \theta_{avg}$, the average flip angle through

the slice; and iii) $\hat{\theta} = \theta_{avg} + 20° \sin\left(x_{pe}\right)$, an erroneous flip angle estimate that varied across image space in the phase-encoded direction. (For brevity, x_{pe} is defined as $+\pi$ at the right edge and $-\pi$ at the left edge.) The true flip angle was $\theta = \theta_{peak} = 150°$ $\left(\theta_{avg} \approx 135°\right)$.

Table 4.1: Monte-Carlo simulation results. Equations [4.1] and [4.2] underestimate Monte-Carlo simulations by < 1.5%.

	Monte-Carlo	Eq. [4.1] or [4.2]
	$\varepsilon_{\hat{T}_2}$ (ms)	$\varepsilon_{\hat{T}_2}$ (ms)
Joint fit	1.138	1.121
$\bar{\theta} = \theta = 150°$	0.952	0.944
$\bar{\theta} = 155°;\ \theta = 150°$	1.376	1.367

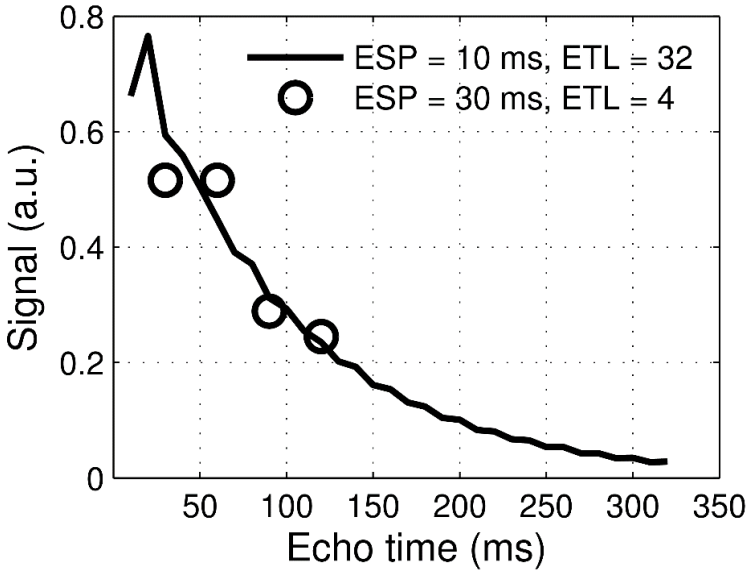

Figure 4.1: Example multiple spin-echo signals resulting from imperfect refocusing. This example used T_2 = 80 ms and a nonselective refocusing pulse with flip angle θ = 120°.

4.4: Results

Figure 4.1 shows example multiple-spin echo signals calculated for the 4- and 32-echo protocols, using $\theta = 120°$. The effect of imperfect refocusing is apparent in the signal oscillations relative to a smooth exponential decay. These signal oscillations enable the joint fitting of T_2 and θ. The results of the Monte-Carlo simulations, presented in Table 4.1, demonstrate close agreement between simulated and predicted fitting errors. Across all simulations, the root mean squared errors of $\hat{T}_2$ predicted by Eq. [4.1] or [4.2] matched those from the simulations to within < 1.5%.

4.4.1: Effect of θ constraint on $\hat{T}_2$ precision

Figure 4.2 shows the $SNR_{\hat{T}_2}$ resulting from various constrained and jointly-fitted protocols for $SNR_{\mathbf{S}} = 100$. For the 32-echo protocol, the predicted improvement in $SNR_{\hat{T}_2}$ through θ constraint was more pronounced when slice-selective refocusing pulses were assumed. In fact, for nonselective refocusing protocols with well-calibrated transmit fields ($\theta > 165°$), as might be the case for single-slice experiments, Fig 4.2a shows that the benefit of θ constraint was minimal even in the presence of a noiseless flip angle estimate. In contrast, for a slice-selective protocol, Figs 4.2c and e demonstrate an increase in $SNR_{\hat{T}_2}$ by up to ≈ 30% can be attained through θ constraint. In the extreme case of a four-echo protocol, poorly calibrated refocusing ($\theta = 90°$), and $SNR_{\hat{\theta}} = SNR_{\mathbf{S}}$, $SNR_{\hat{T}_2}$ was predicted to triple by constraining θ. For any of the tested scenarios,

constraining θ increased $SNR_{\hat{T}_2}$ as long as $SNR_{\hat{\theta}} \geq 1/2 \times SNR_{\mathbf{S}}$, and $SNR_{\hat{T}_2}$ increased with increasing values of $SNR_{\hat{\theta}}$.

Other observations from Figure 4.2 include that the optimal refocusing flip angle for multiple spin echo T_2 measurement was at or near 180°, both for jointly fitted and independently measured θ. However, for the 4-echo, joint-fitted protocol, $SNR_{\hat{T}_2}$ is roughly independent of θ for θ > 140°. Also, while slice-selective refocusing imposes a modest penalty on $SNR_{\hat{T}_2}$, correcting for the known slice profile had little effect on $SNR_{\hat{T}_2}$ except when θ was near 180°.

4.4.2: Effect of θ constraint on $\hat{T}_2$ accuracy

Figure 4.3 shows the biased estimator $\bar{T}_2\left(\hat{\theta}\right)$. The curves have a generally logarithmic shape, indicating that overestimation of θ—i.e., constraint to a value that is higher than the true flip angle—was found to generate less bias in $\hat{T}_2$ than underestimation of θ. Nonselective refocusing or profile correction provided an unbiased $\hat{T}_2$ if $\hat{\theta}$ was unbiased, as expected. Assuming a uniform slice profile when in fact a slice-selective refocusing pulse was employed resulted in a biased $\hat{T}_2$, but this was primarily due to the definition of θ as the peak flip angle rather than the average flip angle across the slice. For example, with θ_{peak} = 175°, the average flip angle over the slice was ≈ 154°. Constraining the fit with the average flip angle (not shown) provided an approximately accurate value for $\hat{T}_2$.

Figure 4.4 compares the $\hat{T}_2$ variance, bias, and mean-squared error of various selectively-refocused protocols where θ_{peak} = 150°. The variance in $\hat{T}_2$, $\sigma^2_{\hat{T}_2}$ —whether θ was constrained or jointly fitted with T_2—is independent of $\hat{\theta}$ bias $(\bar{\theta} - \theta)$, and is thus constant between the two panels. When $\hat{\theta}$ was constrained to θ_{avg} + 1°, bias was dominated by variance, and the T_2 mean-squared error was reduced for $\text{SNR}_{\hat{\theta}} > 40$. This result was similar to the rule of thumb discovered in Fig 4.2 of $SNR_{\hat{\theta}} \geq 1/2 \times SNR_{\mathbf{S}}$. When $\hat{\theta}$ was constrained to θ_{avg} + 5°, T_2 bias dominated variance, and $\varepsilon_{\hat{T}_2}$ was not reduced by θ constraint under any circumstances. Even so, constraint reduced T_2 variance compared to joint-fitted protocols when $\text{SNR}_{\hat{\theta}} > 40$.

The maximum permissible θ bias at which constraining θ results in a lower $\varepsilon_{\hat{T}_2}$ than achievable through joint-fitting is presented in Fig 4.5 as a two-dimensional function of $SNR_{\hat{\theta}}$ and $SNR_{\mathbf{S}}$. Note that the maximum permissible bias is largely a function of $SNR_{\mathbf{S}}$ but goes to zero when $SNR_{\hat{\theta}} \lesssim 1/2 \times SNR_{\mathbf{S}}$, in agreement with the results in Fig 4.2. There is also little difference in this threshold between the 4- and 32-echo protocols, despite stark difference in the biases between these two protocols (Fig 4.3).

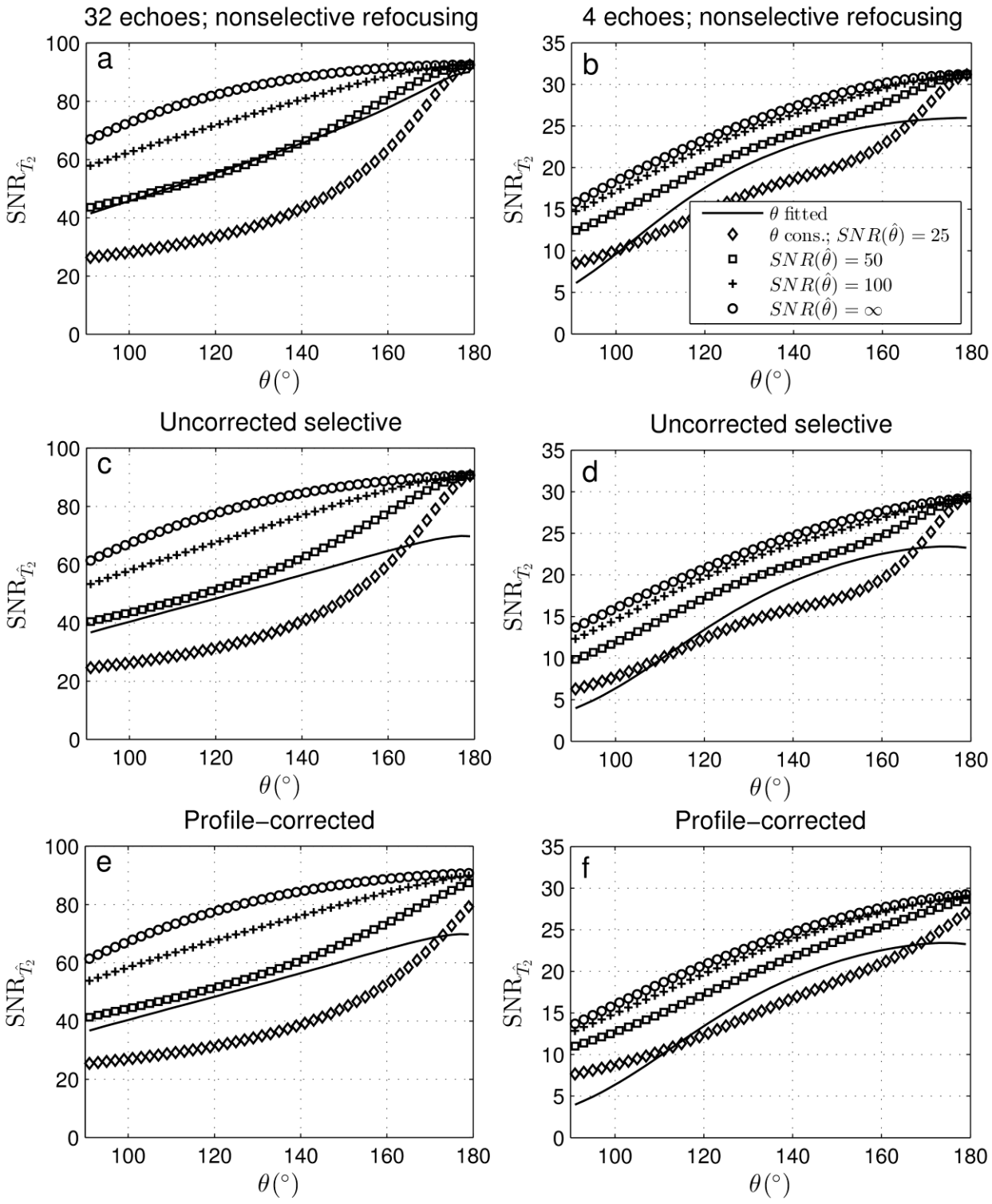

Figure 4.2: The effect of θ constraint on $\hat{T}_2$ precision. In general, constraining θ when $SNR_{\hat{\theta}} \geq 1/2 \times SNR_{\mathbf{s}}$ resulted in higher $SNR_{\hat{T}_2}$ compared to jointly fitting T_2 and θ.

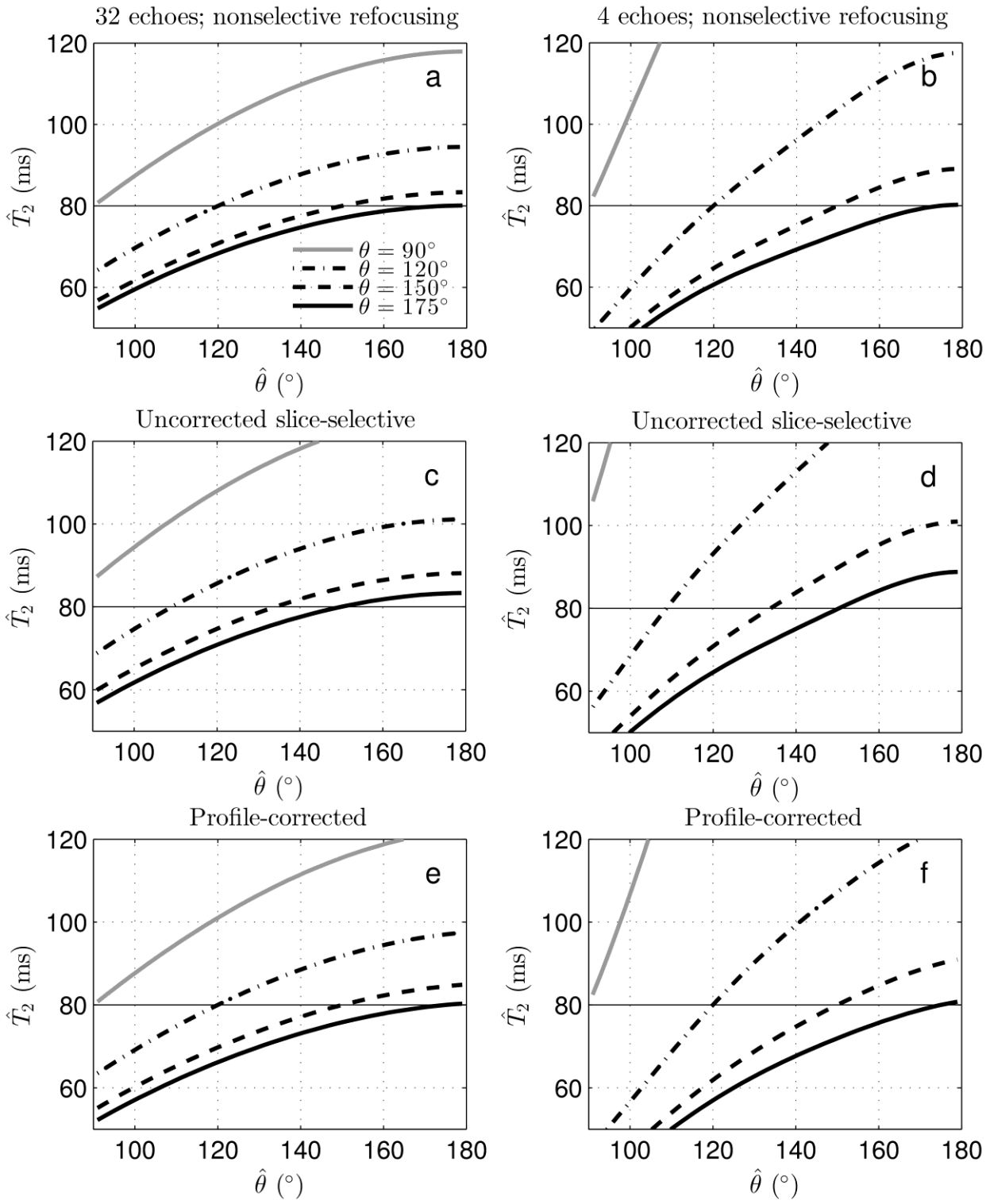

Figure 4.3: The biased estimator function $\overline{T}_2\left(\hat{\theta}\right)$. The true T_2 value was 80 ms. Generally, overestimation of the refocusing pulse flip angle produced less T_2 bias than underestimation of θ.

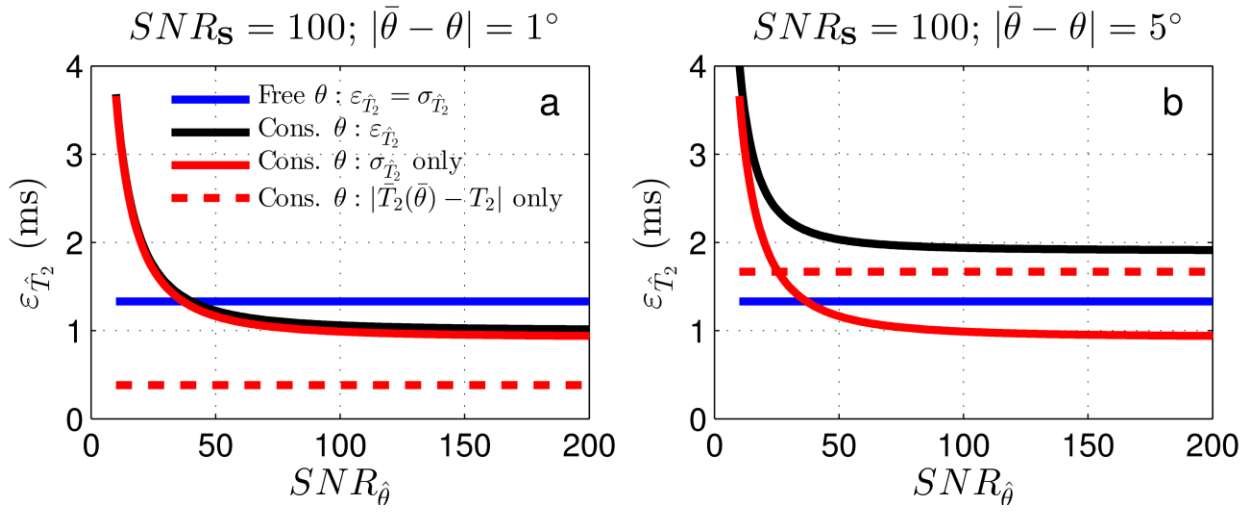

Figure 4.4: Variance, bias, and mean-squared error of $\hat{T}_2$. A relatively small bias in $\bar{\theta}$ (panel a) allows constraint to decrease $\varepsilon_{\hat{T}_2}$ as long as $SNR_{\hat{\theta}}$ was greater than a critical value. When $\bar{\theta}$ bias is increased (panel b), $\varepsilon_{\hat{T}_2}$ is dominated by bias, and θ constraint will never reduce overall error. The actual flip angle was 150°.

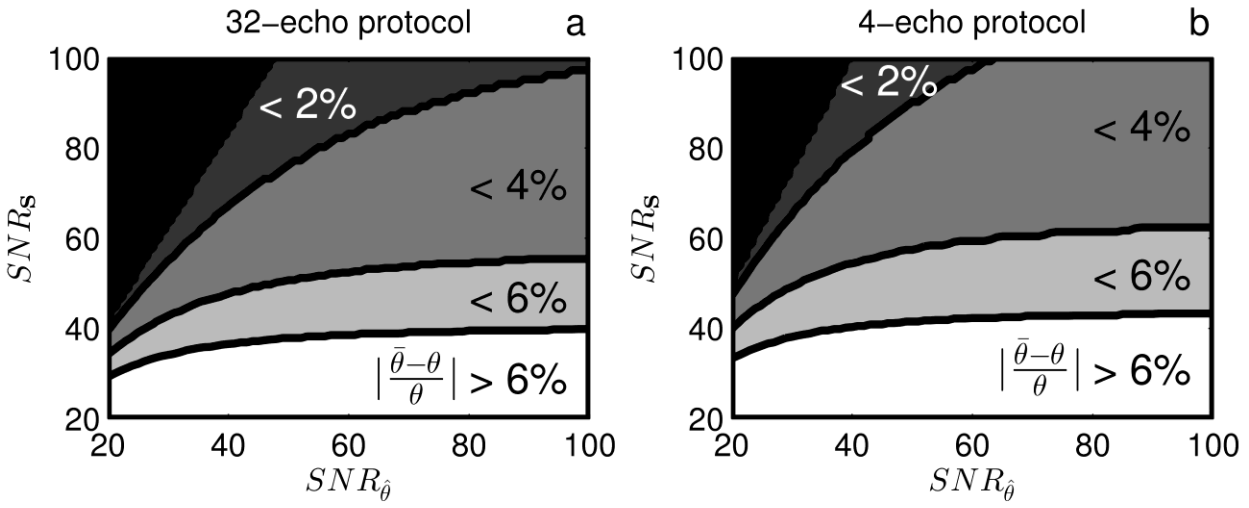

Figure 4.5: Critical $\bar{\theta}$ bias at which $\varepsilon_{\hat{T}_2}$ can no longer be reduced by θ constraint. At high $SNR_{\mathbf{S}}$, very little bias can be tolerated before mean-squared error suffers relative to jointly fitting θ and T_2.

4.4.3: ME-CAMBREC simulations

Figure 4.6 shows the results of the ME-CAMBREC simulations. Constraining θ decreased noise in the reconstructed $\hat{T}_2$ profile, as expected. Constraining θ to the peak value within the slice (150°) introduced T_2 bias similar to that predicted by Figure 4.3. When using the average flip angle across the profile (Figure 4.6d), $\hat{T}_2$ is accurate. The spatially varying constraint (Figure 4.6e) provided a $\hat{T}_2$ profile with spatially varying bias, as might be predicted by Figure 4.3 for a voxelwise analysis. No additional errors caused by the model-based reconstruction were apparent in any of the reconstructions.

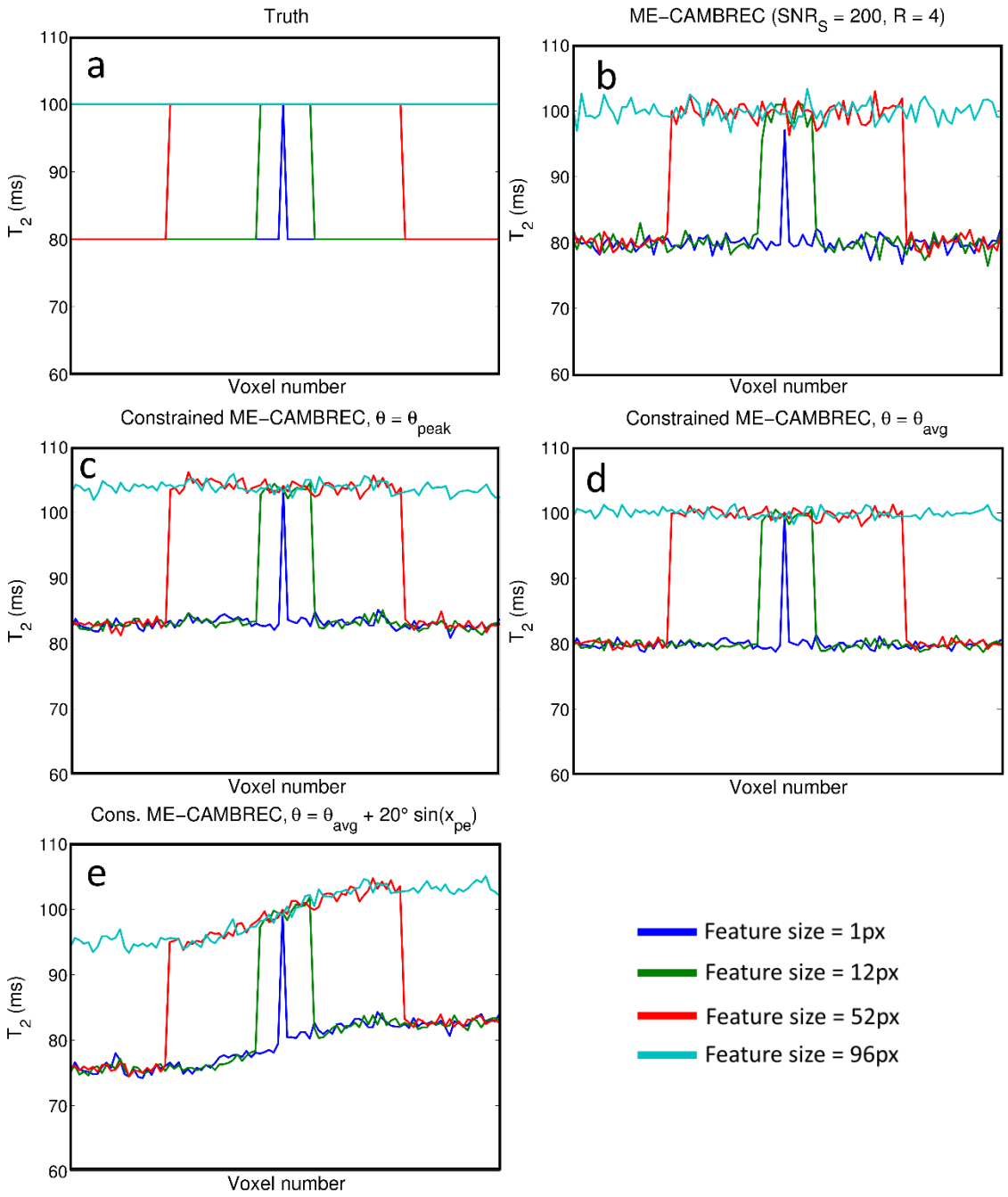

Figure 4.6: *θ* constraint in ME-CAMBREC. T_2 noise is reduced by a factor of roughly 2 when constraining θ to a noiseless value in ME-CAMBREC, which is a greater reduction in T_2 noise than predicted by Equation 4.2. Bias is introduced when the flip angle is erroneously constrained to the peak value (c). Constraint to the average value (d) provides accurate results, which is consistent with results presented in Chapter 3 regarding slice profile effects. Constraining θ to an erroneous spatial function (e) causes T_2 estimate bias to follow that function's error; no anomalous errors specific to ME-CAMBREC or model-based reconstruction appeared in constrained-θ reconstructions.

4.5: Discussion

The results demonstrate the potential to improve the precision of T_2 mapping by independently measuring the refocusing pulse flip angle rather than including it as a free parameter in the fitting. However, the circumstances under which measuring rather than fitting θ is beneficial depends on a number of factors, including the SNR of both the multiple spin echo images and the B_1^+ map, whether a single or multi-slice protocol is required, and to what extent $\hat{T}_2$ accuracy (and not merely precision) is important.

In order to improve $\hat{T}_2$ precision by measuring rather than jointly fitting θ, the independent estimate $\hat{\theta}$ must have an SNR $\gtrsim$ 50% as high as that of the spin echo image at TE = 0 (compare solid line and square symbols in Fig 4.2). For the 32-echo nonselective refocusing case, with $SNR_{\hat{\theta}}$ = $SNR_{\mathbf{S}}$ (+ symbols in Fig 4.2a) and θ = 150°, constraining $\theta = \hat{\theta}$ results in ≈ 22% increase in $SNR_{\hat{T}_2}$. However, the estimate $\hat{\theta}$ comes at a cost of acquisition time, which could also be used to increase the $SNR_{\hat{T}_2}$ through signal averaging. From data presented by Park et al. (101), using the Bloch-Siegert shift method of B_1^+-mapping, $SNR_{\hat{\theta}} \geq SNR_{\mathbf{S}}$ can be obtained in the same scan time as the multiple spin echo measurement (conservatively estimated from Fig 4 in (101)). In this case, it would be better to simply double the number of averaged excitations of the spin echo acquisition, which would increase $SNR_{\hat{T}_2}$ by $\sqrt{2}$. However, B_1^+ maps are typically smooth functions, and so in practice a low-resolution (and, consequently, higher SNR) map is probably sufficient. For example, using a B_1^+ map acquired in 1/4 the scan time of the multiple spin echo acquisition would result in ≈ 30% increase in $SNR_{\hat{T}_2}$ (see Fig 4.2a) at the cost of only a 25% longer scanning time.

For low flip angle refocusing pulses ($\theta \leq 140°$) the benefits in $\hat{T}_2$ precision from constraining θ are similar for nonselective and selective refocusing schemes; they are also indifferent to whether the a slice profile is corrected (compare different rows of Figure 4.2). However, for larger flip angles ($140° \leq \theta \leq 180°$), the benefit diminishes substantially for the 32-echo, nonselective refocusing case. The reason for this effect is that as θ increases toward 180°, the covariance between $\hat{\theta}$ and $\hat{T}_2$ decreases toward zero for nonselective protocols, making joint-fitting more effective. For a slice-selective protocol, the variation in θ across the slice mitigates this effect—in other words, stimulated echoes are never removed entirely from the signal—and some benefit in constraining θ remains. Thus, for a single-slice protocol, which is amenable to good flip angle calibration, there may be little benefit to independently measuring θ. However, for multi-slice protocols or even 3D protocols where a sizable variation in θ over the volume is unavoidable, acquiring a low resolution B_1^+ map may be beneficial for the precision of $\hat{T}_2$.

An additional factor in determining whether to measure or jointly fit θ relates to bias. Given an unbiased estimate of θ, the above analysis of precision tells the whole story. However, if the B_1^+ mapping is inaccurate, then the bias in $\bar{\theta}$ will result in bias in $\hat{T}_2$. Figure 4.3 demonstrates that this effect is greater with fewer echoes and lower refocusing pulse flip angles. A more complete characterization of measurement error then is the mean squared error, $\varepsilon^2_{\hat{T}_2}$. As apparent from Figure 4.5, for $SNR_{\mathbf{S}} \approx 40$ (a typical level for in vivo quantitative MRI), $\bar{\theta}$ must be accurate to within ≈ 6% for its use in T_2 fitting to lower $\varepsilon^2_{\hat{T}_2}$, and this requirement becomes more demanding as $SNR_{\mathbf{S}}$ increases. While numerical studies indicate the potential for several methods to map B_1^+ to within ±2% (101,102), experimental evaluations of such methods to accurately measure large flip angles remain to be done.

Even in cases where the bias in $\bar{\theta}$ is above the threshold in Fig 4.5, certain applications may benefit from the reduction in variance over the loss in accuracy. Note the reduction in variance that occurs in general when $SNR_{\hat{\theta}} \gtrsim ½\ SNR_{\mathbf{s}}$ holds under diverse circumstances, including those in which $\hat{\theta}$ is biased. Furthermore, as shown in Fig 4.3, constraining θ to a value greater than the true value will introduce less bias than using an underestimated $\hat{\theta}$. In fact, for 32-echo protocols with nonselective refocusing pulses and $\theta \gtrsim 150°$, simply constraining $\theta = 180°$ will provide up to 30% improvement in $SNR_{\hat{T}_2}$ at the cost of < 5 ms error in $\hat{T}_2$ (for true T_2 = 80 ms). This primitive approach is therefore an alternative strategy for situations in which the calibration can be assumed to be reasonably accurate. In the case of extremely accurate calibration (θ > 170°) constraint provides little benefit to 32-echo, nonselective protocols (Fig 4.2a). Interestingly, the $\theta > 140°$ regime of 4-echo protocols shows little improvement in joint-fitted $SNR_{\hat{T}_2}$ as the flip angle approaches 180°. This implies that accurate calibration of B_1^+ is not important to T_2 mapping using these protocols in conjunction with stimulated echo correcting models.

Contrariwise, there might be cases in which the inaccuracy caused by θ-bias is far more significant than the potential precision gain. One example could potentially be model-based reconstruction methods such as ME-CAMBREC which use IEC models (52,55,57,92). In these applications, model inconsistencies can lead to spatial distortions such as ghosting, which can seriously degrade fitted T_2 maps. This was, however, not the case in the ME-CAMBREC simulations presented here: noise and bias presented independently of each other and of spatial considerations in Figure 4.6. In fact, the precision of ME-CAMBREC measures of T_2 showed *more* improvement relative to voxelwise analysis than predicted—SNR_{T2} nearly doubled when constraining θ rather than the ≈30% increase predicted by Figure 4.2c. How flip angle errors,

parameter constraint, and other model inconsistencies (e.g., coil sensitivity errors) may interact in practice is still an unanswered question and a potential topic of further investigation.

A recent article by McPhee and Wilman (58) presented similar studies to the work presented here. The authors of that paper concluded that using the EPG algorithm in conjunction with improper slice profile correction (i.e., a single profile that scaled with θ, rather than a recalculated profile for every flip angle) provided inaccurate T_2 values when flip angle was constrained. However, they also discovered that constraining θ improved T_2 precision when using a Bloch simulation-based fitting method in Monte-Carlo simulations, which agrees with the results in Figure 4.2. The authors reported similar T_2 accuracy and precision between joint-fitted and constrained-θ methods in vivo using double angle B_1^+ mapping with $SNR_{\hat{\theta}} \approx 20$; although they did not report a value for $SNR_{\mathbf{S}}$, they noted that all reported regions of interest had $SNR_{\mathbf{S}} > 30$, which implies a $SNR_{\hat{\theta}} / SNR_{\mathbf{S}}$ ratio < 0.66 and is near the approximate break-even point of $SNR_{\hat{\theta}} / SNR_{\mathbf{S}} \approx 0.5$. It should be noted that the EPG signal model used here did not assume a single slice profile in the case of slice-selective pulses, and therefore has more in common with the Bloch-simulation method evaluated by McPhee (58) than the EPG-based methods presented there.

4.6: Conclusions

When using IEC models in T_2 mapping applications, constraining the refocusing pulse flip angle parameter, θ, to a measured value ($\hat{\theta}$) was shown to efficiently improve T_2 estimate precision when $SNR_{\hat{\theta}} \gtrsim ½\ SNR_{\mathbf{S}}$. Previous work suggests this is practically achievable through the Bloch-Siegert shift and Phase Sensitive methods (99,101,102). The potential improvement in $SNR_{\hat{T}_2}$

increased as the refocusing pulses became progressively more imperfect, for example as θ decreased or slice profile effects became more pronounced. The resulting T_2 bias induced through θ-constraint was quantified in Figure 4.3 and an upper limit for statistically beneficial bias was presented in Figure 4.5. Due to the unknown accuracy of many B_1^+ mapping methods at high values of θ, it is not clear whether these upper limits are practically achievable; nevertheless, certain applications—including ME-CAMBREC, based on the results in Figure 4.6—may favor more precise estimates of T_2 at the cost of accuracy.

CHAPTER 5

CONCLUSION

The method presented in Chapter 2—Multiple Echo, Caesar-Cipher Acquisition and Model-Based REConstruction (ME-CAMBREC)—can be used *in vivo* to generate T_2 maps consistent with those generated through fully-sampled means, but in less than $1/6^{th}$ the scan time. Although ME-CAMBREC benefits from acquisition using multi-channel coil arrays, it is not directly compatible with currently-available parallel imaging packages (Figure 2.6). Care should be taken when selecting the regularization parameter, as feature size-dependent T_2 bias can present itself at high regularization factors (Figure 3.2, 3.5). Regularization is weighted too heavily when sharp edge enhancements are visible in the T_2 map. If acceleration factors greater than R = 2 are desired, double-wide refocusing pulses should be employed in order to limit computational instability and resulting T_2 bias (Figures 3.3, 3.4), despite the fact that this requires the use of slice gaps.

Multiple spin echo-based T_2 mapping methods, including ME-CAMBREC, can under certain circumstances benefit from constraining the refocusing flip angle (θ) to a measured value. Figure 4.2 shows that T_2 precision is increased when $\hat{\theta}$ is constrained to a sufficiently precise ($SNR_{\hat{\theta}} \gtrsim ½\ SNR_{\mathbf{s}}$) value, especially when slice-selective refocusing pulses are employed. While the increase in precision is often efficient compared to acquiring multiple signals and averaging them, the T_2 bias caused by erroneous constraint dominates noise effects when $\hat{\theta}$ is biased by less than 10°. This $\hat{\theta}$ bias threshold is less than the difference between the peak and average θ of

double-wide slice selective pulses. Thus, in order to reduce mean-squared error by θ constraint, considerations for slice profile effects must be made during θ-mapping and/or T_2 fitting.

One consideration that is difficult to present in a general sense is the effect of practical energy deposition (SAR) limits on whole-brain ME-CAMBREC. As multi-slice FSE imaging demands a large number of high-amplitude pulses in rapid succession, it is not surprising that ME-CAMBREC protocols will typically require extending TR beyond the duration of acquired echo trains, reducing scan time efficiency. Although extending the refocusing pulses in time will proportionally decrease their deposited energy, this generally comes at the cost of extended echo spacing or increased receiver bandwidth, both of which reduce the SNR of acquired pseudoimages. It is therefore most practical to decrease the echo train length in order to reduce SAR and improve scan efficiency. However, it is important to note that reducing ETL in ME-CAMBREC reduces the acceleration factor compared to a fully-sampled MSE protocol, as the acceleration factor is $R = \mathrm{ETL}/N_Q$, or the ratio of the echo train length to the number of pseudoimages. N_Q has a practical lower limit of 4 pseudoimages in order to sufficiently sample the signal curve's oscillations (which contain B_1^+ information) and decay (which contains T_2 information). Thus, as SAR limitations become tighter and ETL is decreased to compensate, the advantage of ME-CAMBREC compared to other accelerated imaging protocols—for example, parallel imaging (see Fig 2.6)—is substantially diminished. On the other hand, in a scenario where SAR is not a limiting factor (e.g., low field strength), the fact that ME-CAMBREC requires slice gaps to avoid computational instability (Fig 3.3) will cause full-coverage T_2 mapping protocols to have doubled scan time compared to a profile-corrected method with the same acceleration factor. It is therefore important to recognize that ME-CAMBREC should only be used when SAR limitations are strict enough to prevent whole-volume coverage in a single scan, but not so strict as to require a severely reduced

echo train length—say, 8 echoes. The exact "minimum ETL" at which ME-CAMBREC should be used depends on the number of elements in the receiver array, as this defines the practical acceleration factors parallel imaging can achieve.

Another consideration that was not highlighted in the previous chapters was the issue of coil sensitivity mapping for multi-channel receive coils. Corrupted coil sensitivity maps can cause large errors in estimated M_+ and, therefore, T_2. In the previous sections, these maps were estimated from ME-CAMBREC data via the first pseudoimage, to which coil sensitivity maps were fitted as polynomial functions of space. As this pseudoimage contains blurring and, in the presence of imperfect refocusing pulses, ghosting, the estimated coil sensitivity maps were inherently erroneous. Independent measures of C might improve measures of T_2 if these measures are sufficiently accurate and precise, but these accuracy and precision thresholds are currently unknown. An analysis similar to that used in Chapter 4 could be used to determine if independent measures of C would be beneficial to fitted T_2 maps, and may even demonstrate that ME-CAMBREC could fit C during the reconstruction step as additional free parameters.

ME-CAMBREC was designed with ease of implementation in mind. This was the primary motivation behind the choice to use Cartesian-readout FSE instead of radial FSE, which is commonly used by other model-based reconstruction algorithms due to the disproportionate oversampling of the center of k-space (52,57,70). Section 2.5 noted that these radial protocols often require more excitations than ME-CAMBREC—and ironically present higher acceleration factors, R, due to the larger number of excitations required for radial Nyquist sampling—but this oversampling provides computational stability that is attractive compared to ME-CAMBREC. On the other hand, ME-CAMBREC and Sumpf's Cartesian model-based reconstruction algorithms (55,71) can simply apply a Fourier transform in the readout direction, while radial protocols must

perform the iterative reconstruction on both dimensions simultaneously. It is not clear how these competing effects—the oversampled k-space origin and the shift to 2D iterative reconstruction—interact to determine the most stable readout for model-based reconstruction. This should be investigated from both a statistical and algorithmic perspective in the future.

Bias in T_2 estimates caused by common sources of error in ME-CAMBREC was estimated to be on the order of 5 ms in many cases (see Table 2.2 and Figures 3.2, 3.3, and 3.5). This should be taken as a lower limit for practical T_2 detection accuracy in ME-CAMBREC, with this limit increasing in size as relative noise variance increases. This means that ME-CAMBREC may not be an ideal diagnostic tool in, for example, demyelinating diseases in which single-compartment apparent T_2 changes by only a small amount. This study found the theoretical deviation from demyelination to be on the order of 5-10 ms (compare the baseline to the dotted line in Figure 3.5b; this is the approximate deviation in T_2 caused by the presence of myelin), and recent work showed that T_2 changes in early multiple sclerosis were approximately 10 ms (103).

REFERENCES

1. Cooke R, Kuntz ID. The properties of water in biological systems. *Annu. Rev. Biophys. Bioeng.* 1974;3:95–126.

2. Vasilescu V, Katona E, Simplăceanu V, Demco D. Water compartments in the myelinated nerve. III. Pulsed NMR results. *Experientia* 1978;34:1443–4.

3. MacKay A, Whittall K, Adler J, Li D, Paty D, Graeb D. In vivo visualization of myelin water in brain by magnetic resonance. *Magn. Reson. Med.* 1994;31:673–677.

4. McDonald WI, Compston A, Edan G, et al. Recommended diagnostic criteria for multiple sclerosis: Guidelines from the International Panel on the Diagnosis of Multiple Sclerosis. *Ann. Neurol.* 2001;50:121–127.

5. Polman CH, Reingold SC, Edan G, et al. Diagnostic criteria for multiple sclerosis: 2005 Revisions to the "McDonald Criteria." *Ann. Neurol.* 2005;58:840–846.

6. Hernandez RJ, Keim DR, Chenevert TL, Sullivan DB, Aisen AM. Fat-suppressed MR imaging of myositis. *Radiology* 1992;182:217–219.

7. Reimers CD, Schedel H, Fleckenstein JL, Nägele M, Witt TN, Pongratz DE, Vogl TJ. Magnetic resonance imaging of skeletal muscles in idiopathic inflammatory myopathies of adults. *J. Neurol.* 1994;241:306–314.

8. May DA, Disler DG, Jones EA, Balkissoon AA, Manaster BJ. Abnormal Signal Intensity in Skeletal Muscle at MR Imaging: Patterns , Pearls , and Pitfalls. *RadioGraphics* 2000;20:295–315.

9. Poon CS, Henkelman RM. Practical T2 quantitation for clinical applications. *J. Magn. Reson. Imaging* 1992;2:541–553.

10. Carr HY, Purcell EM. Effects of Diffusion on Free Precession in Nuclear Magnetic Resonance Experiments. *Phys. Rev.* 1954;94:630–638.

11. Meiboom S, Gill D. Modified Spin-Echo Method for Measuring Nuclear Relaxation Times. *Rev. Sci. Instrum.* 1958;29:688.

12. Hennig J, Nauerth A, Friedburg H. RARE imaging: a fast imaging method for clinical MR. *Magn. Reson. Med.* 1986;3:823–833.

13. Sodickson DK, Manning WJ. Simultaneous acquisition of spatial harmonics (SMASH): Fast imaging with radiofrequency coil arrays. *Magn. Reson. Med.* 1997;38:591–603.

14. Pruessmann KP, Weiger M, Scheidegger MB, Boesiger P. SENSE: Sensitivity encoding for fast MRI. *Magn. Reson. Med.* 1999;42:952–962.

15. Griswold MA, Jakob PM, Heidemann RM, Nittka M, Jellus V, Wang J, Kiefer B, Haase A. Generalized Autocalibrating Partially Parallel Acquisitions (GRAPPA). *Magn. Reson. Med.* 2002;47:1202–1210.

16. Lustig M, Donoho D, Pauly JM. Sparse MRI: The application of compressed sensing for rapid MR imaging. *Magn. Reson. Med.* 2007;58:1182–1195.

17. Mansfield P. Multi-Planar Image Formation Using NMR Spin Echoes. *J. Phys. C Solid State Phys.* 1977;10:L55–L58.

18. Oshio K, Feinberg DA. GRASE (Gradient-and Spin-Echo) imaging: A novel fast MRI technique. *Magn. Reson. Med.* 1991;20:344–349.

19. Does MD, Gore JC. Rapid acquisition transverse relaxometric imaging. *J. Magn. Reson.* 2000;147:116–20.

20. Prasloski T, Rauscher A, MacKay AL, Hodgson M, Vavasour IM, Laule C, Mädler B. Rapid whole cerebrum myelin water imaging using a 3D GRASE sequence. *Neuroimage* 2012;63:533–539.

21. Zhang J, Kolind SH, Laule C, Mackay AL. Comparison of myelin water fraction from multiecho T2 decay curve and steady-state methods. *Magn. Reson. Med.* 2015;73:223–232.

22. Song HK, Dougherty L. k-Space weighted image contrast (KWIC) for contrast manipulation in projection reconstruction MRI. *Magn. Reson. Med.* 2000;44:825–832.

23. Deoni SCL, Rutt BK, Peters TM. Rapid combined T1 and T2 mapping using gradient recalled acquisition in the steady state. *Magn. Reson. Med.* 2003;49:515–526.

24. Deoni SCL, Ward HA, Peters TM, Rutt BK. Rapid T2 estimation with phase-cycled variable nutation steady-state free precession. *Magn. Reson. Med.* 2004;52:435–439.

25. Deoni SCL. High-resolution T1 mapping of the brain at 3T with driven equilibrium single pulse observation of T1 with high-speed incorporation of RF field inhomogeneities (DESPOT1-HIFI). *J. Magn. Reson. Imaging* 2007;26:1106–1111.

26. Deoni SCL. Transverse relaxation time (T2) mapping in the brain with off-resonance correction using phase-cycled steady-state free precession imaging. *J. Magn. Reson. Imaging* 2009;30:411–417.

27. Crooijmans HJA, Scheffler K, Bieri O. Finite RF pulse correction on DESPOT2. *Magn. Reson. Med.* 2011;65:858–862.

28. Ma D, Gulani V, Seiberlich N, Liu K, Sunshine JL, Duerk JL, Griswold MA. Magnetic resonance fingerprinting. *Nature* 2013;495:187–92.

29. Jiang Y, Ma D, Seiberlich N, Gulani V, Griswold MA. MR fingerprinting using fast imaging with steady state precession (FISP) with spiral readout. *Magn. Reson. Med.* 2015;74:1621–1631.

30. Gao Y, Chen Y, Ma D, et al. Preclinical MR fingerprinting (MRF) at 7 T: Effective quantitative imaging for rodent disease models. *NMR Biomed.* 2015;28:384–394.

31. Davies M, Puy G, Vandergheynst P, Wiaux Y. A Compressed Sensing Framework for Magnetic Resonance Fingerprinting. *SIAM J. Imaging Sci.* 2014;7:27.

32. Ye H, Cauley SF, Gagoski B, Bilgic B, Ma D, Jiang Y, Du YP, Griswold MA, Wald LL, Setsompop K. Simultaneous multislice magnetic resonance fingerprinting (SMS-MRF) with direct-spiral slice-GRAPPA (ds-SG) reconstruction. *Magn. Reson. Med.* 2016.

33. Ye H, Ma D, Jiang Y, Cauley SF, Du Y, Wald LL, Griswold MA, Setsompop K. Accelerating magnetic resonance fingerprinting (MRF) using t-blipped simultaneous multislice (SMS) acquisition. *Magn. Reson. Med.* 2016;75:2078–2085.

34. Whittall KP, MacKay AL, Graeb DA, Nugent RA, Li DKB, Paty DW. In vivo measurement of T2 distributions and water contents in normal human brain. *Magn. Reson. Med.* 1997;37:34–43.

35. Wolff SD, Balaban RS. Magnetization transfer contrast (MTC) and tissue water proton relaxation in vivo. *Magn. Reson. Med.* 1989;10:135–44.

36. Bloch F. Nuclear Induction. *Phys. Rev.* 1946;70:460–474.

37. Bloembergen N, Purcell EM, Pound RV. Relaxation Effects in Nuclear Magnetic Resonance Absorption. *Phys. Rev.* 1948;73:679–712.

38. Levitt, Malcolm H. *Spin Dynamics: Basics of Nuclear Magnetic Resonance.* 2nd Ed. New York: John Wiley & Sons, Inc.; 2008.

39. Hopkins AL, Yeung HN, Bratton CB. Multiple field strength in vivo T1 and T2 for cerebrospinal fluid protons. *Magn. Reson. Med.* 1986;3:303–11.

40. Hahn EL. Spin Echoes. *Phys. Rev.* 1950;80:580–594.

41. Choyke PL, Dwyer AJ, Knopp MV. Functional tumor imaging with dynamic contrast-enhanced magnetic resonance imaging. *J. Magn. Reson. Imaging* 2003;17:509–520.

42. Ogawa S, Lee TM, Kay AR, Tank DW. Brain magnetic resonance imaging with contrast dependent on blood oxygenation. *Proc. Natl. Acad. Sci. USA.* 1990;87:9868–72.

43. Bernstein MA, King KF, Zhou XJ. *Handbook of MRI Pulse Sequences.* Burlington, MA: Elsevier Academic Press; 2004.

44. Pell GS, Briellmann RS, Waites AB, Abbott DF, Lewis DP, Jackson GD. Optimized clinical T2 relaxometry with a standard CPMG sequence. *J. Magn. Reson. Imaging* 2006;23:248–52.

45. Bottomley PA, Edelstein WA. *Method of eliminating effects of spurious free induction decay NMR signal caused by imperfect 180 degrees RF pulses.* US Patent 4,484,138. 1984.

46. Hennig J. Echoes—how to generate, recognize, use or avoid them in MR-imaging sequences. Part I: Fundamental and not so fundamental properties of spin echoes. *Concepts Magn. Reson.* 1991;3:125–143.

47. Majumdar S, Orphanoudakis SC, Gmitro A, O'Donnell M, Gore JC. Errors in the measurements of T2 using multiple-echo MRI techniques. I. Effects of radiofrequency pulse imperfections. *Magn. Reson. Med.* 1986;3:397–417.

48. Majumdar S, Orphanoudakis SC, Gmitro A, O'Donnell M, Gore JC. Errors in the measurements of T2 using multiple-echo MRI techniques. II. Effects of static field inhomogeneity. *Magn. Reson. Med.* 1986;3:562–74.

49. Crawley AP, Henkelman RM. Errors in T2 estimation using multislice multiple-echo imaging. *Magn. Reson. Med.* 1987;4:34–47.

50. Henkelman RM, Hardy PA, Bishop JE, Poon ECS, Plewes DB. Why fat is bright in rare and fast spin-echo imaging. *J. Magn. Reson. Imaging* 1992;2:533–540.

51. Ben-Eliezer N, Sodickson DK, Block KT. Rapid and accurate T2 mapping from multi-spin-echo data using Bloch-simulation-based reconstruction. *Magn. Reson. Med.* 2015;73:809–17.

52. Ben-Eliezer N, Sodickson DK, Shepherd T, Wiggins GC, Block KT. Accelerated and motion-robust in vivo T2 mapping from radially undersampled data using bloch-simulation-based iterative reconstruction. *Magn. Reson. Med.* 2016;75:1346–54.

53. Hennig J. Multiecho imaging sequences with low refocusing flip angles. *J. Magn. Reson.* 1988;78:397–407.

54. Lukzen NN, Petrova M V, Koptyug I V, Savelov AA, Sagdeev RZ. The generating functions formalism for the analysis of spin response to the periodic trains of RF pulses. Echo sequences with arbitrary refocusing angles and resonance offsets. *J. Magn. Reson.* 2009;196:164–9.

55. Sumpf TJ, Petrovic A, Uecker M, Knoll F, Frahm J. Fast T2 Mapping With Improved Accuracy Using Undersampled Spin-Echo MRI and Model-Based Reconstructions With a Generating Function. *IEEE Trans. Med. Imaging* 2014;33:2213–2222.

56. Lebel RM, Wilman AH. Transverse relaxometry with stimulated echo compensation. *Magn. Reson. Med.* 2010;64:1005–14.

57. Huang C, Bilgin A, Barr T, Altbach MI. T2 relaxometry with indirect echo compensation from highly undersampled data. *Magn. Reson. Med.* 2013;70:1026–1037.

58. McPhee KC, Wilman AH. Transverse relaxation and flip angle mapping: Evaluation of simultaneous and independent methods using multiple spin echoes. *Magn. Reson. Med.* 2016. In press.

59. Look DC, Locker DR. Time Saving in Measurement of NMR and EPR Relaxation Times. *Rev. Sci. Instrum.* 1970;41:250.

60. Constable RT, Gore JC. The loss of small objects in variable TE imaging: Implications for FSE, RARE, and EPI. *Magn. Reson. Med.* 1992;28:9–24.

61. Feinberg DA, Hale JD, Watts JC, Kaufman L, Mark A. Halving MR imaging time by conjugation: demonstration at 3.5 kG. *Radiology* 1986;161:527–531.

62. MacFall JR, Pelc NJ, Vavrek RM. Correction of spatially dependent phase shifts for partial Fourier imaging. *Magn. Reson. Imaging* 1988;6:143–155.

63. Noll DC, Nishimura DG, Macovski A. Homodyne Detection in Magnetic Resonance Imaging. *IEEE Trans. Med. Imaging* 1991;10:154–163.

64. Patel MR, Klufas RA, Alberico RA, Edelman RR. Half-fourier acquisition single-shot turbo spin-echo (HASTE) MR: Comparison with fast spin-echo MR in diseases of the brain. *Am. J. Neuroradiol.* 1997;18:1635–1640.

65. Feinberg DA, Setsompop K. Ultra-fast MRI of the human brain with simultaneous multi-slice imaging. *J. Magn. Reson.* 2013;229:90–100.

66. Tong CY, Prato FS. A novel fast T1-mapping method. *J. Magn. Reson. Imaging* 1994;4:701.

67. Tran-Gia J, Stäb D, Wech T, Hahn D, Köstler H. Model-based Acceleration of Parameter mapping (MAP) for saturation prepared radially acquired data. *Magn. Reson. Med.* 2013;70:1524–1534.

68. Tran-Gia J, Lohr D, Weng AM, Ritter CO, Stäb D, Bley TA, Köstler H. A model-based reconstruction technique for quantitative myocardial perfusion imaging. *Magn. Reson. Med.* 2015;76:880–887.

69. Tran-Gia J, Bisdas S, Köstler H, Klose U. A model-based reconstruction technique for fast dynamic T1 mapping. *Magn. Reson. Imaging* 2016;34:298–307.

70. Block KT, Uecker M, Frahm J. Model-based iterative reconstruction for radial fast spin-echo MRI. *IEEE Trans. Med. Imaging* 2009;28:1759–69.

71. Sumpf TJ, Uecker M, Boretius S, Frahm J. Model-based nonlinear inverse reconstruction for T2 mapping using highly undersampled spin-echo MRI. *J. Magn. Reson. Imaging* 2011;34:420–428.

72. Huang C, Graff CG, Clarkson EW, Bilgin A, Altbach MI. T2 mapping from highly undersampled data by reconstruction of principal component coefficient maps using compressed sensing. *Magn. Reson. Med.* 2012;67:1355–1366.

73. Doneva M, Börnert P, Eggers H, Stehning C, Sénégas J, Mertins A. Compressed sensing reconstruction for magnetic resonance parameter mapping. *Magn. Reson. Med.* 2010;64:1114–1120.

74. Velikina J V., Alexander AL, Samsonov A. Accelerating MR parameter mapping using sparsity-promoting regularization in parametric dimension. *Magn. Reson. Med.* 2013;70:1263–1273.

75. Peng X, Liu X, Zheng H, Liang D. Exploiting parameter sparsity in model-based reconstruction to accelerate proton density and T2 mapping. *Med. Eng. Phys.* 2014;36:1428–1435.

76. Zhao L, Feng X, Meyer CH. Direct and accelerated parameter mapping using the unscented Kalman filter. *Magn. Reson. Med.* 2016;75:1989–1999.

77. Busse RF, Hariharan H, Vu A, Brittain JH. Fast spin echo sequences with very long echo trains: design of variable refocusing flip angle schedules and generation of clinical T2 contrast. *Magn. Reson. Med.* 2006;55:1030–7.

78. Weigel M, Hennig J. Contrast behavior and relaxation effects of conventional and hyperecho-turbo spin echo sequences at 1.5 and 3 T. *Magn. Reson. Med.* 2006;55:826–835.

79. Lebel RM, Wilman AH. Intuitive design guidelines for fast spin echo imaging with variable flip angle echo trains. *Magn. Reson. Med.* 2007;57:972–5.

80. Uddin MN, Marc Lebel R, Wilman AH. Transverse relaxometry with reduced echo train lengths via stimulated echo compensation. *Magn. Reson. Med.* 2013;70:1340–1346.

81. Prasloski T, Mädler B, Xiang QS, MacKay A, Jones C. Applications of stimulated echo correction to multicomponent T2 analysis. *Magn. Reson. Med.* 2012;67:1803–1814.

82. Layton KJ, Morelande M, Wright D, Farrell PM, Moran B, Johnston LA. Modelling and estimation of multicomponent T2 distributions. *IEEE Trans. Med. Imaging* 2013;32:1423–1434.

83. Mulkern R V, Melki PS, Jakab P, Higuchi N, Jolesz F a. Phase-encode order and its effect on contrast and artifact in single-shot RARE sequences. *Med. Phys.* 1991;18:1032–1037.

84. Altbach MI, Outwater EK, Trouard TP, Krupinski EA, Theilmann RJ, Stopeck AT, Kono M, Gmitro AF. Radial fast spin-echo method for T2-weighted imaging and T2 mapping of the liver. *J. Magn. Reson. Imaging* 2002;16:179–189.

85. Hansen PC. Analysis of Discrete Ill-Posed Problems by Means of the L-Curve. *SIAM Rev.* 1992;34:561–580.

86. Gulliksson M, Wedin P-A. *Analyzing the nonlinear L-curve.* Department of Computer Science, Umea University, Sweden. 1998.

87. Mulkern R V., Wong STS, Winalski C, Jolesz FA. Contrast manipulation and artifact assessment of 2D and 3D RARE sequences. *Magn. Reson. Imaging* 1990;8:557–566.

88. Deoni SCL, Peters TM, Rutt BK. High-resolution T1 and T2 mapping of the brain in a clinically acceptable time with DESPOT1 and DESPOT2. *Magn. Reson. Med.* 2005;53:237–241.

89. Stanisz GJ, Kecojevic A, Bronskill MJ, Henkelman RM. Characterizing white matter with magnetization transfer and T2. *Magn. Reson. Med.* 1999;42:1128–1136.

90. Melki PS, Mulkern R V. Magnetization transfer effects in multislice RARE sequences. *Magn. Reson. Med.* 1992;24:189–195.

91. Constable RT, Anderson AW, Zhong J, Gore JC. Factors influencing contrast in fast spin-echo MR imaging. *Magn. Reson. Imaging* 1992;10:497–511.

92. Lankford CL, Dortch RD, Does MD. Fast T2 mapping with multiple echo, Caesar cipher acquisition and model-based reconstruction. *Magn. Reson. Med.* 2015;73:1065–74.

93. Gochberg DF, Gore JC. Quantitative imaging of magnetization transfer using an inversion recovery sequence. *Magn. Reson. Med.* 2003;49:501–505.

94. Does MD, Snyder RE. Multiecho Imaging with Suboptimal Spoiler Gradients. *J. Magn. Reson.* 1998;131:25–31.

95. Insko EK, Bolinger L. Mapping of the Radiofrequency Field. *J. Magn. Reson. Ser. A* 1993;103:82–85.

96. Stollberger R, Wach P. Imaging of the active B1 field in vivo. *Magn. Reson. Med.* 1996;35:246–251.

97. Cunningham CH, Pauly JM, Nayak KS. Saturated double-angle method for rapid B1+ mapping. *Magn. Reson. Med.* 2006;55:1326–1333.

98. Yarnykh VL. Actual flip-angle imaging in the pulsed steady state: A method for rapid three-dimensional mapping of the transmitted radiofrequency field. *Magn. Reson. Med.* 2007;57:192–200.

99. Sacolick LI, Wiesinger F, Hancu I, Vogel MW. B1 mapping by Bloch-Siegert shift. *Magn. Reson. Med.* 2010;63:1315–1322.

100. Kay S, Eldar YC. Rethinking biased estimation. *IEEE Signal Process. Mag.* 2008;25:133–136.

101. Park DJ, Bangerter NK, Javed A, Kaggie J, Khalighi MM, Morrell GR. A statistical analysis of the Bloch-Siegert B1 mapping technique. *Phys. Med. Biol.* 2013;58:5673–5691.

102. Morrell GR. A phase-sensitive method of flip angle mapping. *Magn. Reson. Med.* 2008;60:889–894.

103. Gracien RM, Reitz SC, Hof SM, Fleischer V, Zimmermann H, Droby A, Steinmetz H, Zipp F, Deichmann R, Klein JC. Assessment of cortical damage in early multiple sclerosis with quantitative T2 relaxometry. *NMR Biomed.* 2016;29:444–450.

104. Lankford CL, Does MD. On the inherent precision of mcDESPOT. *Magn. Reson. Med.* 2013;69:127–136.

105. Zhang F, editor. *The Schur Complement and Its Applications.* New York: Springer-Verlag; 2005.

APPENDIX 1

DERIVATION OF THE CRAMÉR-RAO LOWER BOUND

This section is adapted from the article "On the inherent precision of mcDESPOT" published in *Magnetic Resonance in Medicine* 69 (2013) by Christopher L. Lankford and Mark D. Does (104). It derives the free and constrained CRLB used in Chapters 2 and 4.

The so-called score vector, **v**, which is the relative rate of change of the signal likelihood function, *f*, with respect to model parameters, **z**, is

$$v_j \equiv \frac{1}{f\left(\mathbf{y},\mathbf{z}\right)}\frac{\partial f\left(\mathbf{y},\mathbf{z}\right)}{\partial z_j} = \frac{\partial}{\partial z_j}\log f\left(\mathbf{y},\mathbf{z}\right). \qquad [A1.1]$$

When *f* is multivariate Gaussian, **v** can be reduced to

$$v_j = \sum_{i=1}^{N}\frac{\left(y_i - g_i\left(\mathbf{z}\right)\right)}{\sigma_i^2}\frac{\partial g_i\left(\mathbf{z}\right)}{\partial z_j} \qquad [A1.2]$$

or, in matrix form as a column vector,

$$\mathbf{v} = \mathbf{J}^T\boldsymbol{\Sigma}^{-1}\mathbf{r} \qquad [A1.3]$$

where **J** is the Jacobian matrix as traditionally defined for the true signal **g**(**z**), **Σ** is the diagonal covariance matrix of the added noise, and **r** is a column vector of noise values. Note that since the expectation of additive noise is zero, the expectation of the score vector is a zero vector. The covariance matrix of the score vector **v**, also known as the Fisher information matrix, is then calculated as follows:

$$\begin{aligned}\mathrm{cov}\left(\mathbf{v}\right) &= \mathrm{E}\left[\mathbf{v}\mathbf{v}^T\right] - \mathrm{E}\left[\mathbf{v}\right]\mathrm{E}\left[\mathbf{v}^T\right] = \mathrm{E}\left[\mathbf{J}^T\boldsymbol{\Sigma}^{-1}\mathbf{r}\mathbf{r}^T\boldsymbol{\Sigma}^{-1}\mathbf{J}\right] - \mathbf{0}\\ &= \mathbf{J}^T\boldsymbol{\Sigma}^{-1}\mathrm{E}\left[\mathbf{r}\mathbf{r}^T\right]\boldsymbol{\Sigma}^{-1}\mathbf{J} = \mathbf{J}^T\boldsymbol{\Sigma}^{-1}\boldsymbol{\Sigma}\boldsymbol{\Sigma}^{-1}\mathbf{J}\\ &= \mathbf{J}^T\boldsymbol{\Sigma}^{-1}\mathbf{J}\end{aligned} \qquad [A1.4]$$

where the symbol $\mathrm{E}[\cdot]$ represents the expectation operation over the likelihood function *f* with respect to **y**. Furthermore, the covariance of **v** with the estimate vector $\hat{\mathbf{z}}$ can be calculated as:

$$\begin{aligned}\operatorname{cov}(\hat{\mathbf{z}},\mathbf{v}) &= \mathrm{E}\left[\hat{\mathbf{z}},\mathbf{v}^T\right] - \mathrm{E}[\hat{\mathbf{z}}]\mathrm{E}\left[\mathbf{v}^T\right] = \mathrm{E}\left[\hat{\mathbf{z}}\left(\frac{1}{f(\mathbf{y},\mathbf{z})}\frac{\partial}{\partial \mathbf{z}} f(\mathbf{y},\mathbf{z})\right)\right] \\ &= \int \hat{\mathbf{z}}\left(\frac{\partial}{\partial \mathbf{z}} f(\mathbf{y},\mathbf{z})\right)\mathrm{d}\mathbf{y} \quad . \end{aligned} \tag{A1.5}$$

Because the estimate $\hat{\mathbf{z}}$ is not directly dependent on underlying parameters **z**, the order of differentiation and integration can be reversed, leaving

$$\operatorname{cov}(\hat{\mathbf{z}},\mathbf{v}) = \frac{\partial}{\partial \mathbf{z}}\int \hat{\mathbf{z}}\, f(\mathbf{y},\mathbf{z})\ \mathrm{d}\mathbf{y} = \frac{\partial \mathrm{E}[\hat{\mathbf{z}}]}{\partial \mathbf{z}}. \tag{A1.6}$$

Substituting Equation A1.6 into the multivariate Cauchy-Schwarz inequality results in a formal statement of the Cramer-Rao bound:

$$\begin{aligned}\operatorname{cov}(\hat{\mathbf{z}}) &\geq \operatorname{cov}(\hat{\mathbf{z}},\mathbf{v})\operatorname{cov}(\mathbf{v})^{-1}\operatorname{cov}(\hat{\mathbf{z}},\mathbf{v})^T \\ &\geq \frac{\partial \mathrm{E}[\hat{\mathbf{z}}]}{\partial \mathbf{z}}\left[\mathbf{J}^T\boldsymbol{\Sigma}^{-1}\mathbf{J}\right]^{-1}\frac{\partial \mathrm{E}[\hat{\mathbf{z}}]^T}{\partial \mathbf{z}} \ . \end{aligned} \tag{A1.7}$$

Note that Equation A1.7 states that the distribution of an estimate is inversely proportional to the model's squared sensitivity to the estimated parameter, which is a generalization of the well-known propagation of error theorem to a possibly biased set of estimates given multiple random points of data. In a further, potentially more significant parallel to the propagation of error theorem, the uncertainty in parameter estimates defined by the CRLB scales inversely with SNR.

Due to the fact that the FIM is purely a function of the true signal and noise variance, information content is unaffected by the choice of estimator. Thus, information is conserved even when the contrast of the estimate is enhanced; the multiplication by $\partial \mathrm{E}[\hat{\mathbf{z}}]/\partial \mathbf{z}$ causes biased estimates which enjoy greater contrast than their unbiased counterparts to receive a proportional penalty to random deviation. Only by constraining covarying parameters to *a priori* values and

eliminating their respective elements from the FIM before inverting—or by decreasing the problem dimensionality in any similar manner—can estimate precision truly be improved. Stated mathematically, the conditional covariance matrix of the parameters in $\hat{\mathbf{z}}_{\text{free}} \subset \hat{\mathbf{z}}$ (those which remain unconstrained) is the Schur complement of the covariance matrix block pertaining to the constrained parameters (105):

$$\operatorname{cov}\left(\hat{\mathbf{z}}_{\text{free}}\right) \geq \frac{\partial \mathrm{E}[\hat{\mathbf{z}}_{\text{free}}]}{\partial \mathbf{z}_{\text{free}}} \left[\Sigma_{\text{free}} - \Sigma_{\text{f,c}} \left(\Sigma_{\text{cons}}{}^{-1} \right) \Sigma_{\text{c,f}} \right] \frac{\partial \mathrm{E}[\hat{\mathbf{z}}_{\text{free}}]^{T}}{\partial \mathbf{z}_{\text{free}}} \qquad \text{[A1.8]}$$

where

$$\operatorname{cov}\left(\hat{\mathbf{z}}\right) \geq \left[\mathbf{J}^{T} \Sigma^{-1} \mathbf{J} \right]^{-1} = \begin{bmatrix} \Sigma_{\text{cons}} & \Sigma_{\text{c,f}} \\ \Sigma_{\text{f,c}} & \Sigma_{\text{free}} \end{bmatrix} \qquad \text{[A1.9]}$$

and $\hat{\mathbf{z}} = \begin{bmatrix} \hat{\mathbf{z}}_{\text{cons}} & \hat{\mathbf{z}}_{\text{free}} \end{bmatrix}^{T}$**,** implying that uncertainty in free parameter estimates is reduced according to the parameter's squared covariance with other parameters ($\Sigma_{\text{f,c}}$).

APPENDIX 2

DERIVATION OF EQUATION 4.2

The mean squared error of $\hat{T}_2$ when using the constraint $\theta = \hat{\theta}$ is well approximated by Equation [4.2]. The derivation of this formula is presented below. By definition, the mean-squared error for an estimate of T_2 that uses an independently-estimated refocusing pulse flip angle, $\hat{\theta}$ is

$$\varepsilon^2_{\hat{T}_2} = E\left[\left(\hat{T}_2\left(\mathbf{s},\hat{\theta}\right) - T_2\right)^2\right], \qquad \text{[A2.1]}$$

where E is the expectation operator and the other elements are defined in Section 4.2. Assuming **s** and $\hat{\theta}$ are independent random variables, the expectation operation can be separated into two stages,

$$\varepsilon^2_{\hat{T}_2} = E_{\hat{\theta}}\left[E_{\mathbf{s}}\left[\left(\hat{T}_2\left(\mathbf{s},\hat{\theta}\right) - T_2\right)^2\right]\right], \qquad \text{[A2.2]}$$

where the expectation symbol's subscript defines the random variables over which integration is implied. It is conventional to separate mean-squared error into two parts: the contribution caused by an estimate's variance and that caused by its bias. In order to achieve this, the term $\bar{T}_2\left(\hat{\theta}\right)$ is introduced as

$$\bar{T}_2\left(\hat{\theta}\right) \triangleq E_{\mathbf{s}}\left[\hat{T}_2\left(\mathbf{s},\hat{\theta}\right)\right]. \qquad \text{[A2.3]}$$

In other words, $\bar{T}_2\left(\hat{\theta}\right)$ is the average estimate of T_2 for a given constraint, $\theta = \hat{\theta}$, and is not a function of noise in the multiple spin echo signals, **s**. Adding and subtracting this term within Eq. [A2.2] provides

$$\begin{aligned}\varepsilon_{\hat{T}_2}^2 &= E_{\hat{\theta}}\left[E_{\mathbf{s}}\left[\left(\hat{T}_2\left(\mathbf{s},\hat{\theta}\right)-\bar{T}_2\left(\hat{\theta}\right)+\bar{T}_2\left(\hat{\theta}\right)-T_2\right)^2\right]\right] \\ &= E_{\hat{\theta}}\left[E_{\mathbf{S}}\left[\left(\hat{T}_2\left(\mathbf{s},\hat{\theta}\right)-\bar{T}_2\left(\hat{\theta}\right)\right)^2\right]\right] \\ &\quad + 2E_{\hat{\theta}}\left[\left(E_{\mathbf{S}}\left[\hat{T}_2\left(\mathbf{s},\hat{\theta}\right)\right]-\bar{T}_2\left(\hat{\theta}\right)\right)\left(\bar{T}_2\left(\hat{\theta}\right)-T_2\right)\right] \quad + \quad E_{\hat{\theta}}\left[\left(\bar{T}_2\left(\hat{\theta}\right)-T_2\right)^2\right]. \end{aligned} \qquad \text{[A2.4]}$$

The cross-term in Eq. [A2.4] vanishes due to the definition in Eq. [A2.3], resulting in

$$\varepsilon_{\hat{T}_2}^2 = E_{\hat{\theta}}\left[E_{\mathbf{S}}\left[\left(\hat{T}_2\left(\mathbf{s},\hat{\theta}\right)-\bar{T}_2\left(\hat{\theta}\right)\right)^2\right]\right] \quad + \quad E_{\hat{\theta}}\left[\left(\bar{T}_2\left(\hat{\theta}\right)-T_2\right)^2\right]. \qquad \text{[A2.5]}$$

The first term inside the expectation over $\hat{\theta}$ is the variance in $\hat{T}_2$ caused by noise in **s** for a given value of $\hat{\theta}$. In most practical cases, this term has only a weak dependence on $\hat{\theta}$, and so it can be approximated by the CRLB independently of $\hat{\theta}$ as

$$E_{\hat{\theta}}\left[E_{\mathbf{S}}\left[\left(\hat{T}_2\left(\mathbf{s},\hat{\theta}\right)-\bar{T}_2\left(\hat{\theta}\right)\right)^2\right]\right] \approx \sigma_{\mathbf{s}}{}^2\left(\mathbf{J}_{M_0,T_2}^T\mathbf{J}_{M_0,T_2}\right)_{T_2,T_2}^{-1} \qquad \text{[A2.6]}$$

For brevity, it is defined here as $\sigma_{\hat{T}_2,\mathbf{S}}^2$. Thus, equation [A2.5] reduces to the approximation

$$\varepsilon_{\hat{T}_2}^2 \approx \sigma_{\hat{T}_2,\mathbf{S}}^2 \quad + \quad E_{\hat{\theta}}\left[\left(\bar{T}_2\left(\hat{\theta}\right)-T_2\right)^2\right]. \qquad \text{[A2.7]}$$

From here, the same procedure used for expanding Eq. [A2.1] can be applied to the second term of Eq. [A2.7]. To do so, we define two new average parameter terms,

$$\bar{\theta} \triangleq E_{\hat{\theta}}\left[\hat{\theta}\right] \qquad \text{[A2.8]}$$

and then

$$\bar{T}_2\left(\bar{\theta}\right) \triangleq E_{\mathbf{S}}\left[\hat{T}_2\left(\mathbf{s},E_{\hat{\theta}}\left[\hat{\theta}\right]\right)\right] = E_{\mathbf{S}}\left[\hat{T}_2\left(\mathbf{s},\bar{\theta}\right)\right]. \qquad \text{[A2.9]}$$

Then, adding and subtracting $\bar{T}_2\left(\bar{\theta}\right)$ inside the squared term in Eq [A2.7] results in

$$\begin{aligned}\varepsilon^2_{\hat{T}_2} &\approx \sigma^2_{T_2,\mathbf{s}} + E_{\hat{\theta}}\left[\left(\bar{T}_2\left(\hat{\theta}\right)-\bar{T}_2\left(\bar{\theta}\right)+\bar{T}_2\left(\bar{\theta}\right)-T_2\right)^2\right] \\ &\approx \sigma^2_{T_2,\mathbf{s}} + E_{\hat{\theta}}\left[\left(\bar{T}_2\left(\hat{\theta}\right)-\bar{T}_2\left(\bar{\theta}\right)\right)^2\right] \\ &\quad + \ 2\left(E_{\hat{\theta}}\left[\bar{T}_2\left(\hat{\theta}\right)\right]-\bar{T}_2\left(\bar{\theta}\right)\right)\left(\bar{T}_2\left(\bar{\theta}\right)-T_2\right) \ + \ \left(\bar{T}_2\left(\bar{\theta}\right)-T_2\right)^2 \end{aligned} \qquad \text{[A2.10]}$$

Here (unlike in Eq. [A2.4]) the cross-term is not zero in general; however, for practical values of $\bar{\theta}-\theta$ and $SNR_{\mathbf{S}}$, it is much smaller than either the variance term $\sigma^2_{\hat{T}_2,\mathbf{S}}$ or the squared T_2 bias, $\left(\bar{T}_2\left(\bar{\theta}\right)-T_2\right)^2$, and can be neglected. The first term is, by definition, the variance of a function of a single random variable and can be approximated using linear propagation of error as,

$$E_{\hat{\theta}}\left[\left(\bar{T}_2\left(\hat{\theta}\right)-\bar{T}_2\left(\bar{\theta}\right)\right)^2\right] \approx \sigma^2_{\hat{\theta}}\left[\frac{\partial \bar{T}_2\left(\hat{\theta}\right)}{\partial \hat{\theta}}\right]^2. \qquad \text{[A2.11]}$$

This term represents the propagation of noise in the measurement of $\hat{\theta}$ to the estimate $\hat{T}_2$. The third term is the squared-bias of the average T_2 estimate (as defined by Eq [A2.9]), and results from bias in the measurement of θ. Thus, in summary, the mean squared error in $\hat{T}_2$ when using an independent measure of refocusing pulse flip angle, $\hat{\theta}$, is approximated as the sum of three terms,

$$\varepsilon^2_{\hat{T}_2} \approx \sigma_{\mathbf{S}}{}^2\left(\mathbf{J}^T_{M_0,T_2}\mathbf{J}_{M_0,T_2}\right)^{-1}_{T_2,T_2} + \sigma^2_{\hat{\theta}}\left(\frac{\partial \bar{T}_2}{\partial \hat{\theta}}\right)^2 + \left(\bar{T}_2\left(\bar{\theta}\right)-T_2\right)^2, \qquad \text{[A2.12]}$$

including (first term) the propagation of noise from the spin echo images, (second term) the propagation of noise from the flip angle measurement, and (third term) the squared bias in $\hat{T}_2$ resulting from the bias in $\hat{\theta}$.

APPENDIX 3

ME-CAMBREC RECONSTRUCTION MATLAB SCRIPT

The following script requires the function pmri_poly_sensitivity by Fa-Hsuan Lin (Martinos Center for Biomedical Imaging, Massachusetts General Hospital, 2004), written August 24th, 2004.

```
function [M0_output,T2_output,B1_output]=...
    mecambrec_recon_multislice_ver093(data,noise,info,varargin)
% ME-CAMBREC image reconstruction function v. 0.93
% Author: Chris Lankford
% Date: Sep 29, 2016
%
% [M0,T2,B1]=mecambrec_recon(data,noise,info,flipangle,lambda);
%
% Outputs:
% M0, a complex matrix of excited magnetization values (pe x ro x nslice)
% T2, a real matrix of fitted T2 values in seconds (pe x ro x nslice)
% B1, a real matrix of fitted refocusing pulse flip angles in degrees
% (pe x ro x nslice)
%
% Inputs:
% data, an array of data generated by feeding the first output of the
%       GPI function 'ReadPhilips' into GPI function 'SaveMAT'.
% noise, an array of noise samples generated by feeding the second output
%       of the GPI function 'ReadPhilips' into GPI function 'SaveMAT'.
% info, a struct of accompanying information generated by the MATLAB
%       function 'loadSIN'.
% flipangle, the nominal flip angle
% lambda, the reconstruction regularization weighting parameter

%Ensure data is as expected
if length(size(data))>5
    error('Unexpected data format: data should have only 5 dimensions.');
end

%Extract array size information
num_coils=size(data,1);
num_pseudoimg=size(data,2);
num_slices=size(data,3);
pe_size=size(data,4);
ro_size=size(data,5)/2;
```

```
%TEMPORARY-FEB 2016; hopefully will be replaced with more black-box logic
designated_flip_angle=varargin{1};
lambda=varargin{2};
lambda=lambda*num_coils*num_pseudoimg*rms(data(:)).^2;

%Extract important parameters as variables, and clear the memory of the big
%inputs (noise covariance and info struct)
ETL=info.tse_factor.vals;
ESP=info.tse_echo_spacing.vals*1e-3;
clear info
noise_covar=cov(noise.');
clear noise

%generate list of effective echo times for each pseudoimage
%this logic is hardcoded into the CAMBREC patch
efftes=zeros(num_pseudoimg,1);
efftes(1)=1;
efftes(2)=2;
for ii=3:num_pseudoimg
    efftes(ii)=3+(ii-3)*floor((ETL-2)/(num_pseudoimg-2));
end

%generate the base acquisition map that will be rotated modulo echo train
%length after the first pseudoimage is acquired
%this logic is hardcoded into the CAMBREC patch
base_acqecho=zeros(pe_size,1);
for ii=1:(pe_size/ETL/2)
    base_acqecho(((pe_size/2 + 1):(pe_size/ETL/2):end) + ii-1)=1:ETL;
    base_acqecho(((pe_size/2):(-pe_size/ETL/2):1) + 1-ii)=1:ETL;
end
base_acqecho=squeeze(base_acqecho);

%rotate modulo echo train length
for ii=1:num_pseudoimg
    acqecho(:,ii)=mod(base_acqecho + (efftes(ii)-1),ETL);
end
acqecho(acqecho==0)=ETL;

%generate accompanying pelist
pelist=repmat(squeeze((-pe_size/2):(pe_size/2 - 1)) , [1 num_pseudoimg]);

%Next few sections are data reconfiguration...

%transform data into hybrid space (IFFT_ro)
data=ifftshift(ifft(fftshift(data,5),[],5),5);

%account for dc offset correction by multiplying all data by either -1 or
%1, alternating between phase encode lines (this is the same as performing
%an extra/one-less FFTSHIFT in the phase encode direction)
data=data.*permute(repmat([-1 1],[ro_size*2,pe_size/2,num_coils, ...
    num_pseudoimg,num_slices]),[3 4 5 2 1]);

%remove oversampling in readout direction
data=data(:,:,:,:,round(1/2*ro_size + 1):round(3/2*ro_size));
```

```
%create coil index vector, pevector, acqechovector
coilnum=zeros(num_coils*numel(pelist),1);
for coil=1:num_coils
    coilnum((coil-1)*numel(pelist) + (1:numel(pelist)))=coil;
end
pevector=repmat(pelist(:),[num_coils,1]);
acqechovector=repmat(acqecho(:),[num_coils,1]);

%ready output arrays
M0_output=zeros(pe_size,ro_size,num_slices);
T2_output=zeros(pe_size,ro_size,num_slices);
B1_output=zeros(pe_size,ro_size,num_slices);


%%%%%%%% Loop across slices
for slice_counter=1:num_slices

    %Shouldn't have any problems, but just in case...
    clear coilsens_mask
    clear coilsens_nomask
    clear coilsens

    %%%%%%%%%%%%%%%%%%%%%%%%%%%%%%%%%%%%%%%%%%%%%%%%%%%%%%%%%%%%%%%%%%%%%%%%%%%
    %Next few sections are estimation of coil sensitivity maps...

    %create reference image for each coil from first-pseudoimage data
    refimgs=squeeze(...
        ifftshift(ifft(fftshift(data(:,1,slice_counter,:,:),4),[],4),4));
    if num_coils==1
        refimgs=permute(refimgs,[3 1 2]);
    end
    refreconimg=squeeze(sqrt(sum(abs(refimgs).^2./ ...
        repmat(diag(noise_covar),[1,pe_size,ro_size]),1)));

    %create masks from data
    fitting_mask=refreconimg > 0.1*max(refreconimg(:));

    %create sensitivity maps
    if num_coils==1
        coilsens(1,1:size(refreconimg,1),1:size(refreconimg,2))=1;
    else
        for coil=1:num_coils
            [coilsens_mask(:,:,coil),coilsens_nomask(:,:,coil)]=...
                pmri_poly_sensitivity( squeeze(refimgs(coil,:,:)), 3,...
                'mask', fitting_mask);
            coilsens(coil,:,:)=permute(coilsens_nomask(:,:,coil)/...
                max(max(abs(fitting_mask.*coilsens_nomask(:,:,coil)))),...
                [3 1 2]);
        end
    end
    mask3d=permute(repmat(fitting_mask,[1 1 num_coils]),[3 1 2]);
    coilsens(~mask3d)=1;

    coilsens=coilsens*exp(-1i*pi/4);%This is for scaling the penalty
```

```
    %%%%%%%%%%%%%%%%%%%%%%%%%%%%%%%%%%%%%%%%%%%%%%%%%%%%%%%%%%%%%%%%%%%%%%%

    %Finally, call the ME-CAMBREC recon code line-by-line
    M0=zeros(ro_size,pe_size);
    R2=zeros(ro_size,pe_size);
    B1=zeros(ro_size,pe_size);
    for imgcol=1:ro_size
        signalvector=permute(squeeze(data(:,:,slice_counter,:,imgcol)),...
            [3 2 1]);
        %data now is {pe, pseudoimg, coil} to match vectors above
        signalvector=signalvector(:);

        if max(fitting_mask(:,imgcol))>0
            [M0(imgcol,:),R2(imgcol,:),B1(imgcol,:)]=...
                mecambrec_parallel_subfunc(double(signalvector),pevector,...
                acqechovector,coilnum,...
                double(squeeze(coilsens(:,:,imgcol).')),...
                double(diag(noise_covar)),fitting_mask(:,imgcol).',...
                double(ESP),double(designated_flip_angle),...
                double(lambda));
        end
        if mod(imgcol,5)==0
            num_fitted_cols=nnz(max(fitting_mask(:,:),[],1)>0);
            num_fitted_cols_to_here=nnz(max(fitting_mask(...
                :,1:imgcol),[],1)>0);
            fprintf('Slice %d, %2.1f%% complete...\n',...
                slice_counter,100*num_fitted_cols_to_here/num_fitted_cols);
            if mod(imgcol,10)==0
                figure(1);imagesc(abs(1./R2'));axis image off;
                caxis([0 .2]);
                drawnow;
            end
        end
    end

    %tweak data for presentability and store in output variables
    R2=R2';
    M0=M0.';
    B1=B1';
    T2=1./R2;
    T2(isnan(T2))=0;
    T2(T2==inf)=0;
    badmask=T2<(ESP*1.5);
    M0_output(:,:,slice_counter)=M0.*~badmask;
    T2_output(:,:,slice_counter)=T2.*~badmask;
    B1_output(:,:,slice_counter)=B1.*~badmask;
    save('MECAMBREC_inprogress.mat','M0_output','T2_output','B1_output');
    fprintf('Slice %d complete...\n',slice_counter);
end
```

```
function [M0,R2,B1]=mecambrec_parallel_subfunc(k_signal,pelist,acqecho,...
    coilnum,coilsen,coilnoise,mask,ESP,desig_flip,varargin)

if nargin>9
    lambda=varargin{1};
else
    lambda=0;
end

acqecho=int16(acqecho);
pelist=int16(pelist);
coilnum=int16(coilnum);

if size(coilnoise,1)==size(coilnoise,2)
    %Noise covariance matrix rather than noise variance vector
    psiinv=inv(coilnoise);
    weights=diag(psiinv);
    weights=weights(coilnum);
    weights=repmat(weights(:),2,1);
elseif size(coilnoise,1)==1 || size(coilnoise,2)==1
    psiinv=1./coilnoise;
    psiinv=psiinv(:);
    weights=psiinv(coilnum);
    weights=repmat(weights(:),2,1);
    psiinv=diag(psiinv);
else
    error('Coil noise covariance must be a square matrix or a vector');
end

numpts=length(mask);
coilnum=coilnum-(min(coilnum)-1);

%Create a best-guess for T2 from kpe=0 data and the receive coil with
%maximum signal
[~,maxind]=sort(abs(k_signal).*logical(0==mod(pelist,numpts)));
maxind=maxind(end);
coil_used_for_est=coilnum(maxind);

guess_decay=abs(k_signal(logical(0==mod(pelist,numpts)) & ...
    logical(coilnum==coil_used_for_est)));
guess_echoes=double(acqecho(logical(0==mod(pelist,numpts)) & ...
    logical(coilnum==coil_used_for_est)));
even_t=ESP*guess_echoes(logical(mod(guess_echoes,2)==0));
odd_t=ESP*guess_echoes(logical(mod(guess_echoes,2)==1));
even_decay=guess_decay(logical(mod(guess_echoes,2)==0));
odd_decay=guess_decay(logical(mod(guess_echoes,2)==1));
guess_X=[ones([length(even_t) 1]), zeros([length(even_t) 1]), -even_t(:)];
guess_X=[guess_X;[zeros([length(odd_t) 1]),...
    ones([length(odd_t) 1]), -odd_t(:)]];
guess_Y=log([even_decay(:);odd_decay(:)]);
guess_b=(guess_X'*guess_X)\guess_X'*guess_Y;
T2_guess=1/guess_b(3);
```

```
% create a k-space vector using a roughly inside-out path
for ncoil=int16(1:max(coilnum(:)))
    k0_coil=zeros([numpts 1]);
    last_echo=int16(1);
    for pe=int16(0:max(pelist))
        viable_points=(mod(pe,numpts)==mod(pelist,numpts)) &...
            (acqecho>=last_echo) & (coilnum==ncoil);
        [sorted_viable_acqecho,indices1]=...
            sort(double(acqecho).*viable_points);
        sorted_signal=k_signal(indices1);
        myindex=find(sorted_viable_acqecho,1);
        last_echo=sorted_viable_acqecho(myindex);
        k0_coil(pe+1)=sorted_signal(myindex);
    end
    last_echo=int16(1);
    for pe=int16(-1:-1:min(pelist))
        viable_points=(mod(pe,numpts)==mod(pelist,numpts)) &...
            (acqecho>=last_echo) & (coilnum==ncoil);
        [sorted_viable_acqecho,indices1]=...
            sort(double(acqecho).*viable_points);
        sorted_signal=k_signal(indices1);
        myindex=find(sorted_viable_acqecho,1);
        last_echo=sorted_viable_acqecho(myindex);
        k0_coil(mod(pe,numpts)+1)=sorted_signal(myindex);
    end

    img_coil(:,ncoil)=ifftshift(ifft(k0_coil));
end

img0=diag(conj(coilsen)*psiinv*img_coil.')./...
    diag(conj(coilsen)*psiinv*coilsen.');

%Roughly account for first-echo decay, for sake of scaling
scalefactor=1/getsignal(1,1,T2_guess,desig_flip,0,ESP,1);
init_M0=scalefactor*img0;

initmask=mask;

init_M0_i=imag(init_M0(initmask));
init_M0_r=real(init_M0(initmask));
init_R1=ones(size(init_M0_r));
init_R2=1/T2_guess*ones(size(init_M0_r));
init_B1=desig_flip*ones(size(init_M0_r));
indices=find(initmask);

M0_r=zeros(numpts,1);
R2=zeros(numpts,1);
B1=zeros(numpts,1);
M0_i=zeros(numpts,1);

options=optimset('Jacobian','on','TolFun',1e-16,'TolX',1e-20,'MaxIter',...
    25,'MaxFunEvals',100,'Display','off');

signal_r=real(k_signal);
signal_i=imag(k_signal);
```

```
if ~isempty(indices)
    initguess=[init_M0_r(:); init_M0_i(:); init_R2(:); init_B1(:)];
    lb=[-inf*ones(size(init_M0_r)), -inf*ones(size(init_M0_i)),...
        .25*ones(size(init_R2)), 10*ones(size(init_B1))];
    ub=[inf*ones(size(init_M0_r)), inf*ones(size(init_M0_i)),...
        1/ESP*ones(size(init_R2)), 179.98*ones(size(init_B1))];
    %179.8 is the limit to ensure forward differences are still < 180
    %degrees, for stability.

    %Here's where the work gets done
    recon_fit=lsqnonlin(@model_recon_cost_function_lsq,initguess,lb,ub,...
        options,pelist,acqecho,coilnum,coilsen,ESP,signal_r,signal_i,...
        init_R1,indices,numpts,weights,lambda,init_M0);
    B1(indices)  =recon_fit((3*length(indices)+1):(4*length(indices)));
    M0_r(indices)=recon_fit((0*length(indices)+1):(1*length(indices)));
    M0_i(indices)=recon_fit((1*length(indices)+1):(2*length(indices)));
    R2(indices)  =recon_fit((2*length(indices)+1):(3*length(indices)));
end
M0=M0_r(:)+1i*M0_i(:);

function [return_cost, varargout]=model_recon_cost_function_lsq(...
    params,pelist,acq_echo,coilnum,coilsens,esp,signal_r,signal_i,...
    R1_guess,indices,total_points,weights,lambda,fourier_M0)
sqrtweights=sqrt(weights);
numpts=length(params)/4;
M0_r=params((0*numpts+1):(1*numpts));
M0_i=params((1*numpts+1):(2*numpts));
R2  =params((2*numpts+1):(3*numpts));
B1  =params((3*numpts+1):(4*numpts));
R1=R1_guess;

if nargout>1
    jac=zeros([2*length(signal_r)+2*(total_points-1),length(params)]);
    if nargout>2
        hessiant=zeros(length(params));
        hessiany=zeros(length(params));
    end
end

M0=M0_r(:)+1i*M0_i(:);
true_M0=zeros([total_points 1]);true_M0(indices)=M0;
norm_decay_curves=zeros(max(acq_echo),numpts);
decay_curves=zeros(max(acq_echo),numpts,max(coilnum));
total_space=zeros(max(acq_echo),total_points,max(coilnum));

%penalty calculations
fourier_diff_r=real(diff(fourier_M0))./real(fourier_M0(2:end) +...
    fourier_M0(1:(end-1)));
fourier_diff_i=imag(diff(fourier_M0))./imag(fourier_M0(2:end) +...
    fourier_M0(1:(end-1)));
real_diff=real(diff(true_M0))./real(true_M0(2:end) + true_M0(1:(end-1)));
imag_diff=imag(diff(true_M0))./imag(true_M0(2:end) + true_M0(1:(end-1)));
penalty=[(real_diff(:)-fourier_diff_r(:));...
    (imag_diff(:)-fourier_diff_i(:))];
penalty_zero_mask=isnan(penalty); %takes care of difference between zeros.
```

```
penalty(penalty_zero_mask)=0;

if nargout>1 %Calculation of penalty gradients/hessian
    for ii=1:numpts
        if (indices(ii)<total_points)&&(~penalty_zero_mask(indices(ii)))
            jac(2*length(signal_r)+indices(ii),0*numpts+ii)=...
                sqrt(lambda)*(-2)*real(true_M0(indices(ii)+1))/...
                (M0_r(ii)+real(true_M0(indices(ii)+1)))^2;
                %real, ii to the next
            jac(2*length(signal_r)+(total_points-1)+indices(ii),...
                1*numpts+ii)=...
                sqrt(lambda)*(-2)*imag(true_M0(indices(ii)+1))/...
                (M0_i(ii)+imag(true_M0(indices(ii)+1)))^2;
                %imag, ii to the next
            if nargout>2
                hessiany(0*numpts+ii,0*numpts+ii)=...
                    2*4*real(true_M0(indices(ii)+1))/...
                    (M0_r(ii)+real(true_M0(indices(ii)+1)))^3*...
                    penalty(indices(ii));
                hessiany(1*numpts+ii,1*numpts+ii)=...
                    2*4*imag(true_M0(indices(ii)+1))/...
                    (M0_i(ii)+imag(true_M0(indices(ii)+1)))^3*...
                    penalty(total_points-1+indices(ii));
                if (ii+1<=length(indices))&&((indices(ii)+1)==...
                        indices(ii+1))
                    %cross term of 2nd derivative term
                    hessiany(0*numpts+ii,0*numpts+ii+1)=...
                        2*2*(M0_r(ii+1)-M0_r(ii))/...
                        (M0_r(ii+1)+M0_r(ii))^3*...
                        penalty(indices(ii));
                    hessiany(0*numpts+ii+1,0*numpts+ii)=...
                        2*2*(M0_r(ii+1)-M0_r(ii))/...
                        (M0_r(ii+1)+M0_r(ii))^3*...
                        penalty(indices(ii));
                    hessiany(1*numpts+ii,1*numpts+ii+1)=...
                        2*2*(M0_i(ii+1)-M0_i(ii))/...
                        (M0_i(ii+1)+M0_i(ii))^3*...
                        penalty(total_points-1+indices(ii));
                    hessiany(1*numpts+ii+1,1*numpts+ii)=...
                        2*2*(M0_i(ii+1)-M0_i(ii))/...
                        (M0_i(ii+1)+M0_i(ii))^3*...
                        penalty(total_points-1+indices(ii));
                end
            end
        end
        if (indices(ii)>1)&&(~penalty_zero_mask(indices(ii)-1))
            jac(2*length(signal_r)+indices(ii)-1,0*numpts+ii)=...
                sqrt(lambda)*(2)*real(true_M0(indices(ii)-1))/...
                (M0_r(ii)+real(true_M0(indices(ii)-1)))^2;
                %real, previous to ii
            jac(2*length(signal_r)+(total_points-1)+indices(ii)-1,...
                1*numpts+ii)=...
                sqrt(lambda)*(2)*imag(true_M0(indices(ii)-1))/...
                (M0_i(ii)+imag(true_M0(indices(ii)-1)))^2;
                %imag, previous to ii
            if nargout>2
                hessiany(0*numpts+ii,0*numpts+ii)=...
```

```
                    hessiany(0*numpts+ii,0*numpts+ii) + ...
                    2*-4*real(true_M0(indices(ii)-1))/...
                    (M0_r(ii)+real(true_M0(indices(ii)-1)))^3*...
                    penalty(indices(ii)-1);
                hessiany(1*numpts+ii,1*numpts+ii)=...
                    hessiany(1*numpts+ii,1*numpts+ii) + ...
                    2*-4*imag(true_M0(indices(ii)-1))/...
                    (M0_i(ii)+imag(true_M0(indices(ii)-1)))^3*...
                    penalty(total_points-1+indices(ii)-1);
            end
        end
    end
end

%Forward model
for ii=1:numpts
    norm_decay_curves(:,ii)=getsignal(1,1/R1(ii),1/R2(ii),B1(ii),...
        0,esp,max(acq_echo));
    for ncoil=1:max(coilnum)
        decay_curves(:,ii,ncoil)=coilsens(indices(ii),ncoil)*...
            M0(ii)*norm_decay_curves(:,ii);
        total_space(:,indices(ii),ncoil)=decay_curves(:,ii,ncoil);
    end
end

k_decay=fft(fftshift(total_space,2),[],2);
%uncentered theoretical k-space data

%Calculate cost
theo_signal=zeros(size(pelist));
for ii=1:length(pelist)
    theo_signal(ii)=k_decay(acq_echo(ii),1+mod(pelist(ii),total_points),...
        coilnum(ii));
end
cost=(theo_signal(:)-(signal_r(:)+1i*signal_i(:)));
return_cost=[([real(cost);imag(cost)].*sqrtweights);sqrt(lambda)*penalty];

if nargout>1 %Calculate jacobian
    step=1e-5;
    for ii=1:numpts
        decay_inc_R2=M0(ii)*getsignal(...
            1,1/R1(ii),1/(R2(ii)*(1+step)),B1(ii),0,esp,max(acq_echo));
        decay_inc_B1=M0(ii)*getsignal(...
            1,1/R1(ii),1/R2(ii),B1(ii)*(1+step),0,esp,max(acq_echo));
        delM_delM0r=1*norm_decay_curves(:,ii);
        delM_delM0i=1i*norm_decay_curves(:,ii);
        delM_delR2=(decay_inc_R2.'-M0(ii)*...
            norm_decay_curves(:,ii))/(R2(ii)*step);
        delM_delB1=(decay_inc_B1.'-M0(ii)*...
            norm_decay_curves(:,ii))/(B1(ii)*step);
        if B1(ii)==180
            delM_delB1=zeros(size(delM_delB1));
        end
```

```
sensitivities_for_this_point=coilsens(indices(ii),coilnum).';
%get ready for fft-ish operation, so fftshift the current point
phaseconst=...
    -1i*2*pi/double(total_points)*...
    (mod(double(indices(ii))-ceil(double(total_points)/2),...
    double(total_points))-1);
delS_delM0r=...
    sensitivities_for_this_point.*delM_delM0r(acq_echo).*...
    exp(phaseconst*mod(double(pelist),total_points));
delS_delM0i=...
    sensitivities_for_this_point.*delM_delM0i(acq_echo).*...
    exp(phaseconst*mod(double(pelist),total_points));
delS_delR2=...
    sensitivities_for_this_point.*delM_delR2(acq_echo).*...
    exp(phaseconst*mod(double(pelist),total_points));
delS_delB1=...
    sensitivities_for_this_point.*delM_delB1(acq_echo).*...
    exp(phaseconst*mod(double(pelist),total_points));

jac(1:(2*length(signal_r)),0*numpts+ii)=...
    [real(delS_delM0r);imag(delS_delM0r)].*sqrtweights;
jac(1:(2*length(signal_r)),1*numpts+ii)=...
    [real(delS_delM0i);imag(delS_delM0i)].*sqrtweights;
jac(1:(2*length(signal_r)),2*numpts+ii)=...
    [real(delS_delR2);imag(delS_delR2)].*sqrtweights;
jac(1:(2*length(signal_r)),3*numpts+ii)=...
    [real(delS_delB1);imag(delS_delB1)].*sqrtweights;


if nargout>2
    decay_dec_R2=M0(ii)*getsignal(...
        1,1/R1(ii),1/(R2(ii)*(1-step)),B1(ii),0,esp,max(acq_echo));
    decay_dec_B1=M0(ii)*getsignal(...
        1,1/R1(ii),1/R2(ii),B1(ii)*(1-step),0,esp,max(acq_echo));
    decay_inc_R2B1=M0(ii)*getsignal(...
        1,1/R1(ii),1/(R2(ii)*(1+step)),B1(ii)*(1+step),0,...
        esp,max(acq_echo));
    decay_dec_R2B1=M0(ii)*getsignal(...
        1,1/R1(ii),1/(R2(ii)*(1-step)),B1(ii)*(1-step),0,...
        esp,max(acq_echo));

    del2M_delR22=(decay_inc_R2.'+decay_dec_R2.'...
        -2*M0(ii)*norm_decay_curves(:,ii))/(R2(ii)*step)^2;
    del2M_delB12=(decay_inc_B1.'+decay_dec_B1.'...
        -2*M0(ii)*norm_decay_curves(:,ii))/(B1(ii)*step)^2;
    del2M_delR2delB1=(decay_inc_R2B1.'-decay_inc_R2.'-...
        decay_inc_B1.'...
        +2*M0(ii)*norm_decay_curves(:,ii)-decay_dec_R2.'...
        -decay_dec_B1.'+decay_dec_R2B1.')/2/(B1(ii)*step)/...
        (R2(ii)*step);
    if B1(ii)==180
        del2M_delB12=zeros(size(del2M_delB12));
        del2M_delR2delB1=del2M_delB12;
    end
```

```
del2M_delM0rdelR2=real(delM_delR2)/M0_r(ii);
del2M_delM0idelR2=1i*imag(delM_delR2)/M0_i(ii);
del2M_delM0rdelB1=real(delM_delB1)/M0_r(ii);
del2M_delM0idelB1=1i*imag(delM_delB1)/M0_i(ii);

del2S_delM0rdelR2=sensitivities_for_this_point.*...
    del2M_delM0rdelR2(acq_echo).*...
    exp(phaseconst*mod(double(pelist),total_points));
del2S_delM0idelR2=sensitivities_for_this_point.*...
    del2M_delM0idelR2(acq_echo).*...
    exp(phaseconst*mod(double(pelist),total_points));
del2S_delM0rdelB1=sensitivities_for_this_point.*...
    del2M_delM0rdelB1(acq_echo).*...
    exp(phaseconst*mod(double(pelist),total_points));
del2S_delM0idelB1=sensitivities_for_this_point.*...
    del2M_delM0idelB1(acq_echo).*...
    exp(phaseconst*mod(double(pelist),total_points));
del2S_delR22     =sensitivities_for_this_point.*...
    del2M_delR22(acq_echo).*...
    exp(phaseconst*mod(double(pelist),total_points));
del2S_delB12     =sensitivities_for_this_point.*...
    del2M_delB12(acq_echo).*...
    exp(phaseconst*mod(double(pelist),total_points));
del2S_delR2delB1 =sensitivities_for_this_point.*...
    del2M_delR2delB1(acq_echo).*...
    exp(phaseconst*mod(double(pelist),total_points));

%Hessian calculation
hessiant(0*numpts+ii,2*numpts+ii)=...
    2*sqrtweights'.*[real(del2S_delM0rdelR2);...
    imag(del2S_delM0rdelR2)]'*...
    return_cost(1:(2*length(signal_r)));
hessiant(2*numpts+ii,0*numpts+ii)=...
    hessiant(0*numpts+ii,2*numpts+ii);
hessiant(0*numpts+ii,3*numpts+ii)=...
    2*sqrtweights'.*[real(del2S_delM0rdelB1);...
    imag(del2S_delM0rdelB1)]'*...
    return_cost(1:(2*length(signal_r)));
hessiant(3*numpts+ii,0*numpts+ii)=...
    hessiant(0*numpts+ii,3*numpts+ii);
hessiant(1*numpts+ii,2*numpts+ii)=...
    2*sqrtweights'.*[real(del2S_delM0idelR2);...
    imag(del2S_delM0idelR2)]'*...
    return_cost(1:(2*length(signal_r)));
hessiant(2*numpts+ii,1*numpts+ii)=...
    hessiant(1*numpts+ii,2*numpts+ii);
hessiant(1*numpts+ii,3*numpts+ii)=...
    2*sqrtweights'.*[real(del2S_delM0idelB1);...
    imag(del2S_delM0idelB1)]'*...
    return_cost(1:(2*length(signal_r)));
hessiant(3*numpts+ii,1*numpts+ii)=...
    hessiant(1*numpts+ii,3*numpts+ii);
hessiant(2*numpts+ii,2*numpts+ii)=...
    2*sqrtweights'.*[real(del2S_delR22);...
    imag(del2S_delR22)]'*...
    return_cost(1:(2*length(signal_r)));
```

```
            hessiant(3*numpts+ii,3*numpts+ii)=...
                2*sqrtweights'.*[real(del2S_delB12);...
                imag(del2S_delB12)]'*...
                return_cost(1:(2*length(signal_r)));
            hessiant(2*numpts+ii,3*numpts+ii)=...
                2*sqrtweights'.*[real(del2S_delR2delB1);...
                imag(del2S_delR2delB1)]'*...
                return_cost(1:(2*length(signal_r)));
            hessiant(3*numpts+ii,2*numpts+ii)=...
                hessiant(2*numpts+ii,3*numpts+ii);
        end

    end %Looping over fitted image points
    varargout{1}=jac;
    if nargout>2
        hessiany=hessiany+2/lambda*...
            jac((2*length(signal_r)+1):end,:)'*...
            jac((2*length(signal_r)+1):end,:);
        hessiant=hessiant+...
            2*jac(1:(2*length(signal_r)),:)'*jac(1:(2*length(signal_r)),:);
        beta=4/lambda^2*(jac((2*length(signal_r)+1):end,:)'*...
            return_cost((2*length(signal_r)+1):end))'/...
            (hessiant+lambda*hessiany)*...
            (jac((2*length(signal_r)+1):end,:)'*...
            return_cost((2*length(signal_r)+1):end));
        t=sum(return_cost(1:(2*length(signal_r))).^2);
        y=1/lambda*sum(return_cost((2*length(signal_r)+1):end).^2);
        q=t/lambda/y;
        kappa=q/(1+q^2)^(3/2)*(q*(lambda*beta)^-1*y - (q+1));
        varargout{2}=kappa;
%         save analytic_jac
    end
end %calculating jacobian, and return from here

function echo_amp = getsignal(M0,T1,T2,flip_angle,prepTEs,TE,ETL)
    % Computes the normalized echo decay curve for a MR spin echo
    % sequence with the given parameters.
    %
    % ETL: Echo train length (number of echos)
    % flip_angle: Angle of refocusing pulses (degrees)
    % TE: Interecho time (seconds)
    % T2: Transverse relaxation time (seconds)
    % T1: Longitudinal relaxation time (seconds)
    % M0: Signal density (a.u.)
    % prepTEs: T2-prep duration, must be an odd integer
    ETL=double(ETL);

    flip_angle=flip_angle*pi/180;

    % Initialize magnetization phase state vector (MPSV)
    flip_angle_exc=90*pi/180;
    M=zeros(3*(ETL+prepTEs),1);
    M(1)=exp(-(TE/2)/T2)*sin(flip_angle_exc); %excited F1
    M(3)=(1-(1-cos(flip_angle_exc))*exp(-(TE/2)/T1)); %excited Z
```

```
    % Compute relaxation matrix
    T_r=relaxmat(ETL+prepTEs,TE,T2,T1);
    % Initialize vector to track echo amplitude
    echo_amp=zeros(1,ETL);
    % Compute flip matrix
    [~,T_p]=flipmat(flip_angle,ETL+prepTEs);

    % Perform flip-relax sequence ETL-1 times
    for x=1:(ETL+prepTEs)
        % Perform the flip
        % Record the magnitude of the population
        % of F1* as the echo amplitude
        % and allow for relaxation
        if x>prepTEs
            M=T_p*M;
            echo_amp(1,x-prepTEs)=abs(M(2,1))*exp(-(TE/2)/T2);
        elseif x==ceil(prepTEs/2)
            M=T_p*M;
        end
        % Allow time evolution of magnetization between pulses
        M=T_r*M;
    end
    echo_amp=echo_amp*M0;
    return

function [T_1,T_p] = flipmat(alpha,num_pulses)
    % Computes the transition matrix that describes the effect of the
    % refocusing pulse on the magnetization phase state vector.

    % Compute the flip matrix as given by Hennig (1988), but corrected by
    % Jones (1997)
    T_1=[cos(alpha/2)^2,sin(alpha/2)^2,-1i*sin(alpha);...
        sin(alpha/2)^2,cos(alpha/2)^2,1i*sin(alpha);...
        -0.5i*sin(alpha),0.5i*sin(alpha),cos(alpha)];
    % Create a block matrix with T_1 on the diagonal and zeros elsewhere
    T_p=spalloc(3*num_pulses,3*num_pulses,9*num_pulses);
    for x=1:num_pulses
        T_p(3*x-2:3*x,3*x-2:3*x)=T_1;
    end
    return



function T_r = relaxmat(num_states,te,t2,t1)
    % Computes the relaxation matrix that describes the time evolution of
    % the magnetization phase state vector after each refocusing pulse.

    % Create a matrix description of the time evolution as described by
    % Hennig (1988)
    T_r=zeros(3*num_states,3*num_states);
    % F1* --> F1
    T_r(1,2)=exp(-te/t2);
    % F(n)* --> F(n-1)*
    for x=1:num_states-1
        T_r(3*x-1,3*x+2)=exp(-te/t2);
    end
```

```
% F(n) --> F(n+1)
for x=1:num_states-1
    T_r(3*x+1,3*x-2)=exp(-te/t2);
end
% Z(n) --> Z(n)
for x=1:num_states
    T_r(3*x,3*x)=exp(-te/t1);
end
T_r=sparse(T_r);
return
```